박 사 학 위 논 문
Ph.D. Dissertation

확장된 Saint-Venant 비틀림 이론 및 이를 이용한 비틀림을 받는 빔의 위상 최적화

Extended Saint-Venant torsion theory and its application to topology optimization of beams under torsion

2022

이 동 화 (李 東 和 Lee, Dong-Hwa)

한 국 과 학 기 술 원

Korea Advanced Institute of Science and Technology

박 사 학 위 논 문

확장된 Saint-Venant 비틀림 이론 및 이를 이용한 비틀림을 받는 빔의 위상 최적화

2022

이 동 화

한 국 과 학 기 술 원

기계항공공학부

확장된 Saint-Venant 비틀림 이론 및 이를 이용한 비틀림을 받는 빔의 위상 최적화

이 동 화

위 논문은 한국과학기술원 박사학위논문으로
학위논문 심사위원회의 심사를 통과하였음

2021년 12월 6일

심사위원장 이 필 승 (인)

심 사 위 원 윤 정 환 (인)

심 사 위 원 오 일 권 (인)

심 사 위 원 이 익 진 (인)

심 사 위 원 전 형 민 (인)

Extended Saint-Venant torsion theory and its application to topology optimization of beams under torsion

Dong-Hwa Lee

Advisor: Phill-Seung Lee

A dissertation/thesis submitted to the faculty of
Korea Advanced Institute of Science and Technology in
partial fulfillment of the requirements for the degree of
Doctor of Philosophy in Mechanical Engineering

Daejeon, Korea
December 6, 2021

Approved by

Phill-Seung Lee
Professor of Mechanical Engineering

The study was conducted in accordance with Code of Research Ethics[1).]

1) Declaration of Ethical Conduct in Research: I, as a graduate student of Korea Advanced Institute of Science and Technology, hereby declare that I have not committed any act that may damage the credibility of my research. This includes, but is not limited to, falsification, thesis written by someone else, distortion of research findings, and plagiarism. I confirm that my dissertation contains honest conclusions based on my own careful research under the guidance of my advisor.

DME 이동화. 확장된 Saint-Venant 비틀림 이론 및 이를 이용한 비틀림을 받는 빔의 위상 최적화. 기계공학과. 2022년. 69+viii 쪽. 지도교수: 이필승. (영문 논문)
Dong-Hwa Lee. Extended Saint-Venant torsion theory and its application to topology optimization of beams under torsion. Department of Mechanical Engineering. 2022. 69+viii pages. Advisor: Phill-Seung Lee. (Text in English)

초 록

본 논문에서는 종방향 불연속성을 갖는 빔의 와핑 함수(warping function)를 계산하는 새롭고 효율적인 방법을 제안한다. 제안된 계면 와핑 함수(interface warping function)는 기존 Saint-Venant 비틀림 이론을 3차원 영역으로 확장하여 계산된다. 계산된 계면 와핑 함수를 연속체 역학 기반 빔 요소에 적용하여 길이 방향 불연속성이 있는 임의 단면 모양 빔을 분석해 보았다. 그 결과, 기하 및 재료 불연속면을 가진 빔 유한 요소 해석에서 이전 연구 방법보다 더 적은 자유도를 사용해 더 높은 정확도의 해를 얻을 수 있었다. 본 기법을 활용하여 주어진 힘 조건에 대한 최적의 빔 단면을 찾는 위상최적화 기법 또한 제시되었다. 잘 알려진 SIMP 방법이 구현되었고, 민감도(sensitivity)는 추가 가정 없이 연속체역학 빔에서 직접 유도되었다. 수치 예제들을 통해 제안된 방법이 낮은 계산비용과 좋은 수렴성능을 보여준다는 것을 확인했다.

핵 심 낱 말 유한요소법, 빔 요소, 와핑 함수, 불연속단면, 합성보, 비선형해석, 위상최적설계

Abstract

In this dissertation, the new efficient method of calculating the warping function of a beam with a longitudinal discontinuity is proposed. The proposed interface warping function is obtained by extending the classical Saint-Venant torsion theory to a three-dimensional domain. The calculated interface warping functions are employed in the continuum-mechanics based beam formulation to analyze arbitrary shape cross-section beams with longitudinal discontinuities. Compared to the previous work, higher accuracy with fewer degrees of freedom is obtained for beams with geometric and material discontinuities. Using this method, topology optimization of finding the optimal beam cross-section for a given force condition can be formulated. A well-known SIMP method is implemented and the sensitivity is directly derived from the continuum mechanics based beam without further assumption. Through numerical examples, it was confirmed that the proposed method has good convergence behavior with a low computational cost.

Keywords Finite element method, Beam element, Warping function, Discontinuous cross-section, Composite beam, Nonlinear analysis

Contents

List of Tables

List of Figures

Chapter 1. Introduction

1.1 Development of Beam Models

Beam structures not only exist in nature, but have been widely used in many fields of engineering such as mechanical, marine, civil, and aerospace engineering. The development of beam models to interpret pillars and girders has been a long topic. Numerous beam models have been developed to predict when beams break and interpret the buckling of beams.

Historic records say, Galileo was the first to test the load limit of a beam, which sparked research on the beam. In 1691, Bernoulli suggested the problem of "How does a thin rod bend?", and Euler presented its solution using the calculus of variation. The model we call now an Euler-Bernoulli beam model was the first beam model which includes elastic.

It was the French engineers and mathematicians from 'Ecole Polytechnique', who made most of the important contribution to the theory of elasticity. Cauchy, Lame, Poisson, Saint-Venant, Duleau, and Navier are the mathematicians who contributed to elasticity theory, including the development of the beam model. Saint-Venant analyzed a cylindrical rod under uniform torsion using the ‘semi-inverse’ method, which was an extension of Poisson’s work.

With the development of elasticity theory, the beam model can be extended to curved three-dimensional space with various load conditions. Kirchhoff, a former student of Gauss, developed the new beam model by assuming that the beam is composed of prism segments with different loads. Love eliminated the idea of segments and generalized the Euler-Bernoulli beam model into three-dimensional space. However, it maintained Euler’s assumption of beam: cross-sections remain plane, undistorted, and normal to the rod axis.

It was the Cosserat brothers, who introduced the director vectors to solve the twisted curved beams, like spring. By introducing a material coordinate system, deformation including bending, twisting, shearing, and stretching can be specified.

Ehrenfest (1916) and Timoshenko (1921) published a beam model which includes shear deformation in the Euler-Bernoulli beam model, and it is now called the Timoshenko-Ehrenfest beam model. Later on, Reissner extended the model into three-dimensional space using curvature [1].

1.2 Finite Element Method and Degenerated Element

The finite element method (FEM) is widely used to solve physical behaviors of mechanics in various areas, such as solid mechanics, fluid mechanics, thermodynamics, and their coupled problems. In continuum mechanics problems, displacement based elements are widely used to solve static, dynamic, and their coupling problems. The geometry and its displacement are interpolated from the discretized nodal values, using interpolation functions. Isoparametic elements, which use the same interpolation function for both geometry and displacement fields, are the most widely used elements.

When modeling some particular shapes, sometimes it is useful to use specified elements, such as plate, shell, truss, and beam. These elements have lower degrees of freedom by ignoring some relatively small local behaviors. **Fig. 1-1** shows the original physical model and its discretized models using solid, shell, and beam elements. With a proper choice of elements, the global behavior of the original physical model can be calculated with fewer computational costs. And the development of finite elements to express local behaviors with low computational cost has been a long topic.

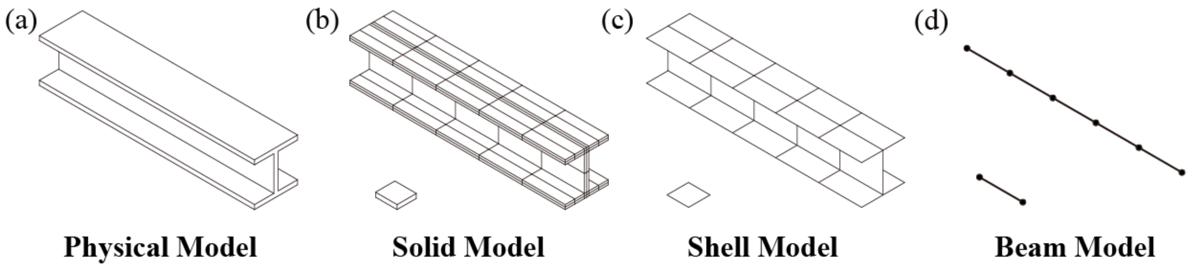

Figure 1-1. (a) The original physical model and its discretization using (b) solid, (c) shell, and (d) beam.

The degeneration process is one of the well-known concepts of deriving the elements. **Fig. 1-2** shows the concept of degenerated elements, which are the direct degeneration from the original solid elements. **Fig. 1-2(a)** shows the degeneration process from solid to plate or shell element. The overall geometry is presented by nodes in their mid-surface, and its thickness is represented by director vectors. **Fig. 1-2(b)** shows the degenerated beam element, where the nodes and director vectors represent the geometry and cross-sections.

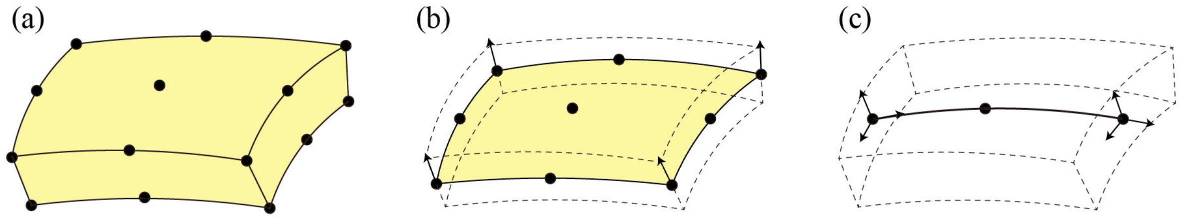

Figure 1-2. The concept of a degenerated element. (a) The solid element, (b) shell element, and (c) beam element.

Numerous researches show that the degenerated elements successfully express the global behavior of the original elements, without further development of elemental theories. Kinematics are straightforward and easy to implement. Most of the coupling effects between their deformation modes are automatically calculated.

Although the degenerated elements have strong computational efficiency, sometimes it gives bad performance when the ignored local behavior plays an important role in global behavior. The twisting behavior on degenerated beam elements is one of the well-known problems. When the cross-sections of the beam are assumed to be undeformed, torsional behavior undergoes 'locking' because it does not represent the local deformation 'warping'.

1.3 Warping on Beams and Its Theories

When the cross-section of the beam is not circular, it does not remain 'planar' when the beam is under twisting behavior, as shown in **Fig. 1-3**. This 'warping' phenomenon is caused by shear stress in the cross-section when twist moment is applied. It is an essential problem in engineering since the shafts are used to transmit the torque.

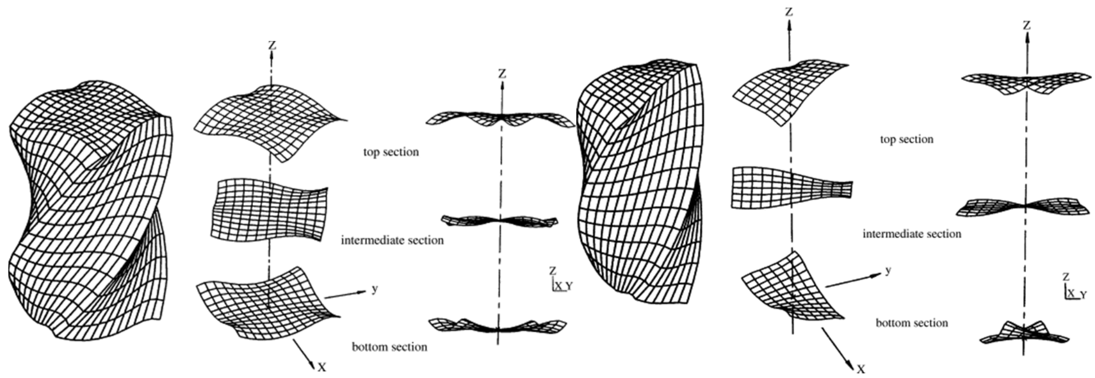

Figure 1-3. The waring of beam when twisting [2].

It has been well known that warping must be considered in order to accurately predict three-dimensional (3D) bending, stretching, and twisting behaviors and their couplings in beams. The development of 3D beam finite elements considering warping has long been an important research topic.

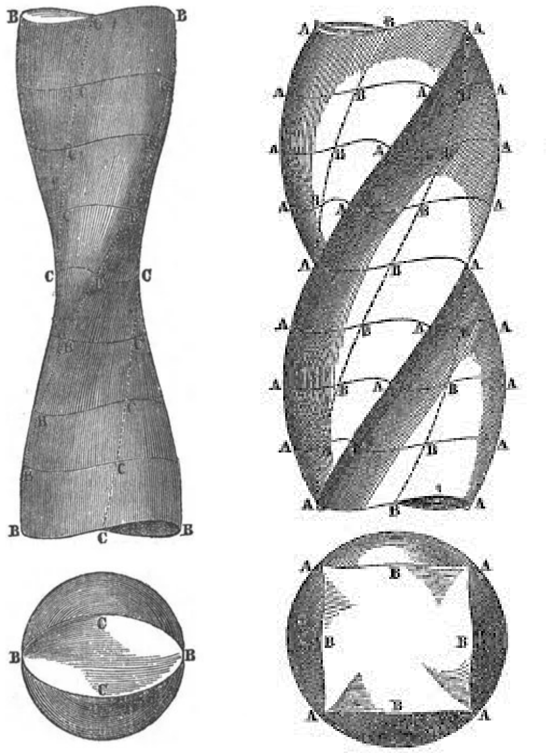

Figure 1-4. Classical Saint-Venant torsion theory and its solution [3].

In order to develop a beam element with the warping effect, an exact warping kinematic must be obtained for a given condition. The most celebrated solution to this phenomenon is the semi-inverse method proposed by Barre de Saint-Venant (1855). **Fig. 1-4** shows the torsion of shafts and their deformation with an elliptic and square cross-section, drawn by Saint-Venant [3]. However, its solution can be only used to analyze a beam with a constant cross-section without any constraints, since it assumes a constant twist rate along the longitudinal direction.

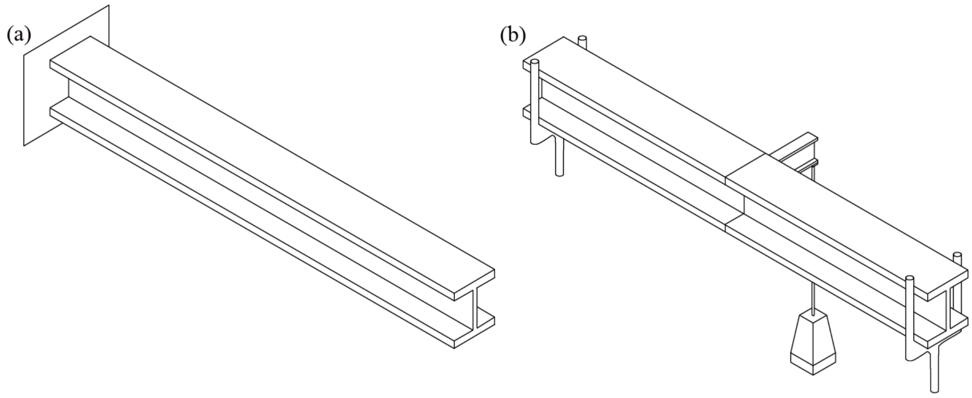

Figure 1-5. Beam with different boundary and force conditions.

Fig. 1-5 shows two beams with different boundary and force conditions. The warping of the beam can be restrained on its boundary support, which is common in engineering practice, as illustrated in **Fig. 1-5(a)**. However, warping can also be restrained due to its loading condition. **Fig. 1-5(b)** shows the constrained warping condition by its load condition, not the boundary condition.

To solve the constrained warping problem, Vlasov [4] proposed the governing equation for the general thin-walled beams to obtain twist rates, using an assumption that shear stress vanishes along the centerline of the thin-walled section. His analytic model was widely adopted however, the model was limited to thin-walled beams and still assumed the cross-section to remain in a plane.

After the advent of the Finite Element Method (FEM), beam theories were implemented into beam elements. For thin-walled beam elements, Vlasov's beam theory and its extensions can be used to analyze the constrained warping problems [5]. In the case of thick beams, studies were proposed under the assumption that the twist rate follows a polynomial function [6-7], an exponential function [8], or a trigonometric function [9].

Another way to consider the warping effect with varying twist rates is enriching the warping displacements and determining its size using additional degrees of freedom. It has advantages in preserving the basic displacement field and presenting non-uniform warping with various boundary conditions. However, the construction of additional warping modes plays an important role.

Benscoter showed that enriching the free warping mode (obtained from Saint-Venant torsion theory) with an additional degree of freedom can not only present the uniform warping but also warping problems with varying twist rates successfully [10]. Batoz proved that the Benscoter type warping enrichment model can also be used to calculate thin-walled beams and showed better results compared to the Vlasov type warping model in closed section beam problems [11]. Further studies to obtain free warping modes on composite beams [12-17], non-isotropic materials [18-20] were suggested. Yoon showed that Benscoter type warping enrichment could be extended to geometric and material nonlinear analysis [21-25] with displacement based degenerated beam.

1.4 Research Motivation

However, most of these works focused on continuously varying cross-sections, such as tapered beams, and only few tried to solve discontinuous cross-section beams [25-27]. Beams with discontinuous cross-sections are easily found in reinforced composite beams. Yoon [25] used additional warping modes, obtained using the Lagrange multiplier method, with an additional degree-of-freedom to solve beams with discontinuous cross-section. As a result, a total of 1~3 warping modes were implemented depending on boundary conditions.

Fig. 1-6 shows an example of a beam with cross-sectional discontinuity and its warping functions. The beam has three different cross-sections: ①, ②, and an interface cross-section between them. The classical Saint-Venant torsion theory provides free warping functions for continuous cross-sections, as shown in **Fig. 1-6(b)**. However, it is difficult to calculate the warping functions at an interface cross-section where discontinuity occurs. The main reason is that the cross-sections adjacent to the interface can have different geometric and material properties, but the classical Saint-Venant theory can only handle continuous cross-sections.

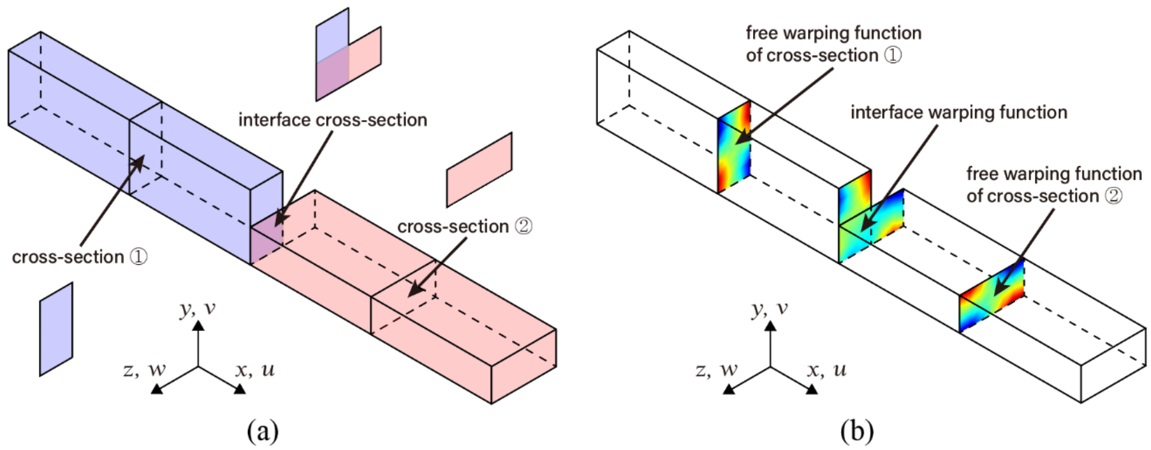

Figure 1-6. Beam with a discontinuously varying cross-section. (a) Cross-sections ① and ②, and the interface cross-section between them. (b) Free warping functions of cross-sections ① and ②, and the interface warping function at the interface cross-section.

Without exact warping function on discontinuous cross-section, one can only build stiffness matrices of beam element using their own cross-sections, as illustrated in **Fig. 1-7(a)**. This violates kinematic compatibility, occurring gap and overlap between elements at discontinuous cross-section, and gives bad results. To avoid boundary discrepancy, as shown in **Fig. 1-7(b)**, exact warping functions at each cross-section should be implemented to build stiffness matrices of each beam element.

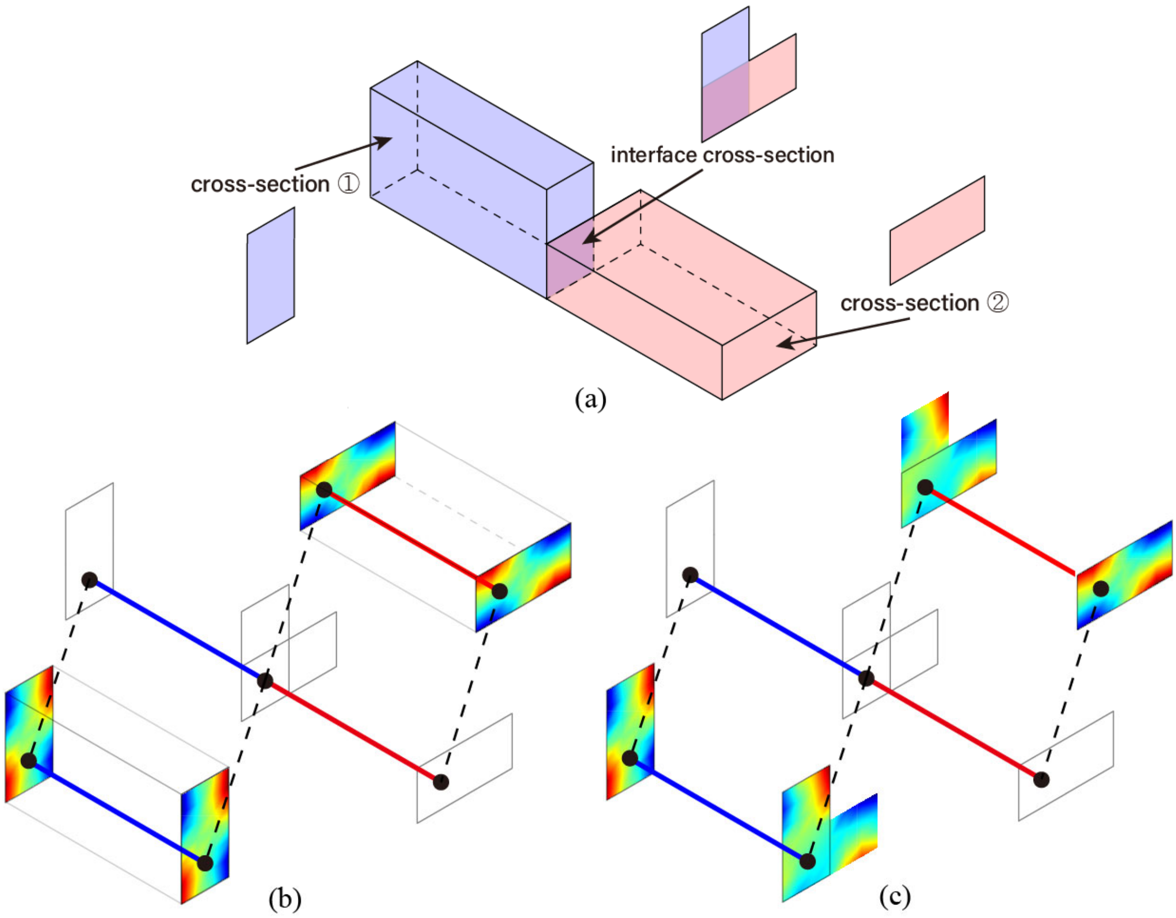

Figure 1-7. Description of implementing warping functions to each beam element. (a) Cross-sections ① and ②, and the interface cross-section between them. (b) Implementing free warping functions of cross-section ① and ② in each element. (c) Implementing free warping functions and the interface warping function, corresponding to their cross-sections.

Chapter 2. Calculation of Interface Warping Function

This chapter describes the classical Saint-Venant torsion theory and introduces displacement-based degenerate beams, the so-called continuum mechanics-based beams. Then, large displacement kinematics for geometric nonlinear analysis and the method of enriching warping mode are introduced.

2.1 Calculation of Free Warping Mode

The Saint-Venant's torsion theory assumes the long straight beam is subjected to a torsional moment at the end, which is free-warping condition. In this section, we assume a long straight beam subjected to a torsional moment at the end, as illustrated in **Fig. 2-1**.

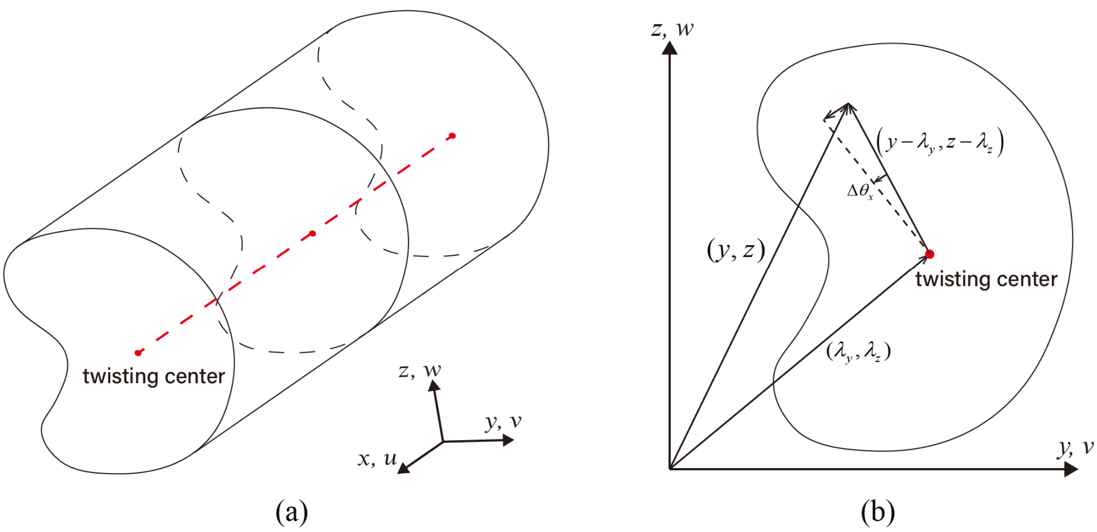

Figure 2-1. (a) Description of arbitrary shaped, prismatic straight beam along *z*-direction. (b) Cross-section with the twisting center.

The cross-section of the beam is assumed to have rigid body rotation from twisting center (λ_y, λ_z), where the cross-sectional in-plane distortion is neglected but free to warp for cross-sectional out-of-plane direction *x*. Assuming small rotation, the displacement field can be decomposed into the cross-sectional part and longitudinal part,

$$u = f(y,z)\frac{d\theta_x}{dx}, \tag{2-1a}$$

$$v = -(z-\lambda_z)\Delta\theta_x, \tag{2-1b}$$

$$w = (y-\lambda_y)\Delta\theta_x, \tag{2-1c}$$

where u, v, and w are displacement for Cartesian coordinate x-, y-, and z-directions, respectively, and $\Delta\theta_x$ is the rotation angle along x-direction. Magnitude of warping displacement is proportional to rate of twist, $d\theta_x / dx$, and its shape is the warping function, $f(y,z)$, which depends on cross-sectional geometry and material distribution.

Small strain-displacement relation proves that the displacement field shows no cross-sectional in-plane strain,

$$\varepsilon_{yy} \equiv \frac{\partial v}{\partial y} = 0, \tag{2-2a}$$

$$\varepsilon_{zz} \equiv \frac{\partial w}{\partial z} = 0, \tag{2-2b}$$

$$\gamma_{yz} \equiv \frac{\partial v}{\partial z} + \frac{\partial w}{\partial y} = -\theta_x + \theta_x = 0, \tag{2-2c}$$

which coincides with conventional beam kinematics.

The local equilibrium equation in static condition with no body force is,

$$\left(\frac{\partial \sigma_{xx}}{\partial x} + \frac{\partial \sigma_{yx}}{\partial y} + \frac{\partial \sigma_{zx}}{\partial z} \right) = 0. \tag{2-3}$$

With stress-strain relation of isotropic beam,

$$\sigma_{xx} \equiv E\varepsilon_{xx} = E\frac{\partial u}{\partial x}, \tag{2-4a}$$

$$\sigma_{yx} \equiv G\gamma_{yx} = G\left(\frac{\partial u}{\partial y} + \frac{\partial v}{\partial x} \right), \tag{2-4b}$$

$$\sigma_{zx} \equiv G\gamma_{zx} = G\left(\frac{\partial u}{\partial z} + \frac{\partial w}{\partial x} \right), \tag{2-4c}$$

Eq. (2-3) become,

$$\left(E\frac{\partial^2 u}{\partial x^2} + G\frac{\partial^2 u}{\partial y^2} + G\frac{\partial^2 u}{\partial z^2} \right) = 0 \quad \text{in} \quad \Omega. \tag{2-5}$$

In order to get boundary condition, no traction condition on surface along x-direction with the displacement field is applied,

$$T_x \equiv \sigma_{xx} n_x + \sigma_{yx} n_y + \sigma_{zx} n_z = E\frac{\partial u}{\partial x} n_x + G\left(\frac{\partial u}{\partial y} + \frac{\partial v}{\partial x} \right) n_y + G\left(\frac{\partial u}{\partial z} + \frac{\partial w}{\partial x} \right) n_z = 0 \quad \text{on} \quad \partial\Omega, \tag{2-6}$$

where n_x, n_y, and n_z are components of surface normal vector along x-, y-, and z-directions respectively.

In the classical Saint-Venant torsion theory, long straight beam with constant cross-section is assumed to have torsion at the end, see **Fig. 2-1(a)**. It results constant rate of twist and twist center along the longitudinal direction since the end-effect due to boundary condition vanishes. As a result, constant rate of twist condition and zero traction condition on surface are presented as

$$\frac{\partial^2 \theta_x}{\partial x^2} = 0 \quad \text{in} \quad \Omega, \tag{2-7a}$$

and

$$T_x = 0 \quad \text{on} \quad \partial\Omega, \tag{2-7b}$$

respectively.

Substituting Eq. (2-7a)-(2-7b) to Eq. (2-5) and Eq. (2-6), we obtain

$$\left[G\frac{\partial^2 u}{\partial y^2} + G\frac{\partial^2 u}{\partial z^2} \right] = 0 \quad \text{in} \quad \Omega, \tag{2-8a}$$

$$G\left(\frac{\partial u}{\partial y} + \frac{\partial v}{\partial x} \right) n_y + G\left(\frac{\partial u}{\partial z} + \frac{\partial w}{\partial x} \right) n_z = 0 \quad \text{on} \quad \partial\Omega. \tag{2-8b}$$

Apply kinematics from Eq. (2-1), we get

$$\left[G\frac{\partial^2 f}{\partial y^2} + G\frac{\partial^2 f}{\partial z^2} \right] \frac{d\theta_x}{dx} = 0 \quad \text{in} \quad \Omega, \tag{2-9a}$$

$$\left[G\left(\frac{\partial f}{\partial y} - \left(z - \lambda_z \right) \right) n_y + G\left(\frac{\partial f}{\partial z} + \left(y - \lambda_y \right) \right) n_z \right] \frac{d\theta_x}{dx} = 0 \quad \text{on} \quad \partial\Omega. \tag{2-9b}$$

Assuming $d\theta_x / dx$ is not zero, and material property is constant inside domain Ω, Eq. (2-9) can be rearranged as,

$$\frac{\partial^2 (Gf)}{\partial y^2} + \frac{\partial^2 (Gf)}{\partial z^2} = 0 \quad \text{in} \quad \Omega, \tag{2-10a}$$

$$\frac{\partial (Gf)}{\partial y} n_y + \frac{\partial (Gf)}{\partial z} n_z = G\left(z - \lambda_z \right) n_y - G\left(y - \lambda_y \right) n_z \quad \text{on} \quad \partial\Omega, \tag{2-10b}$$

or more simply,

$$\nabla^2 (Gf) = 0 \quad \text{in} \quad \Omega, \quad \nabla(Gf)\mathbf{n} = G\left(z - \lambda_z \right) n_y - G\left(y - \lambda_y \right) n_z \quad \text{on} \quad \partial\Omega, \tag{2-11}$$

where $\nabla = \frac{\partial}{\partial y}\mathbf{e}_y + \frac{\partial}{\partial z}\mathbf{e}_z$, and $\mathbf{n} = n_y \mathbf{e}_y + n_z \mathbf{e}_z$.

The variational formulation is introduced to get linearized function of warping function f and twisting center (λ_y, λ_z) [21]. For arbitrary virtual warping function δf, governing equation from Eq. (2-11) provides,

$$0 = \int \nabla^2 (Gf) \delta f \, d\Omega = \int \nabla\left(\nabla(Gf) \right) \delta f \, d\Omega \tag{2-12a}$$

$$= \int \nabla\left(\nabla(Gf) \delta f \right) d\Omega - \int \nabla(Gf) \nabla(\delta f) \, d\Omega \quad \text{(Integration by parts)} \tag{2-12b}$$

$$= \int \nabla(Gf)\delta f\,\mathbf{n}\,d\partial\Omega - \int \nabla(Gf)\nabla(\delta f)\,d\Omega \quad \text{(Divergence theorem)}, \tag{2-12c}$$

whereas, boundary condition from Eq. (2-11) provides,

$$\nabla(Gf)\delta f\,\mathbf{n} = \left[G\left(z-\lambda_z\right)n_y - G\left(y-\lambda_y\right)n_z\right]\delta f\ . \tag{2-13}$$

Combining Eq. (2-12c) and Eq. (2-13), final form of variational formulation is obtained,

$$\int \nabla(\delta f)\nabla(Gf)\,d\Omega = \int\left[G\left(z-\lambda_z\right)n_y - G\left(y-\lambda_y\right)n_z\right]\delta f\,d\partial\Omega \quad \text{in} \quad \Omega\ . \tag{2-14}$$

Even though, the formulations above are assumed to have constant material inside the domain Ω, it can be easily extended to composite material beam with combining cluster of multi-material sub-beams, as shown in **Fig. 2-2**. For simplicity of discretization, in this chapter we assume the beam consist of multiple sub-element with single material properties each.

Let us consider a discretized cross-sectional domain $\Omega = \bigcup_{d=1}^{q}\Omega^{(d)}$ with q number of sub-beam elements, as shown in **Fig. 2-2**, denoted using index *d*. Warping function $f = h_i(y,z)f_i$, and virtual warping function $\delta f = h_i(y,z)\delta f_i$, are interpolated from discretized nodal values f_i and δf_j, using same interpolation function $h_i(y,z)$.

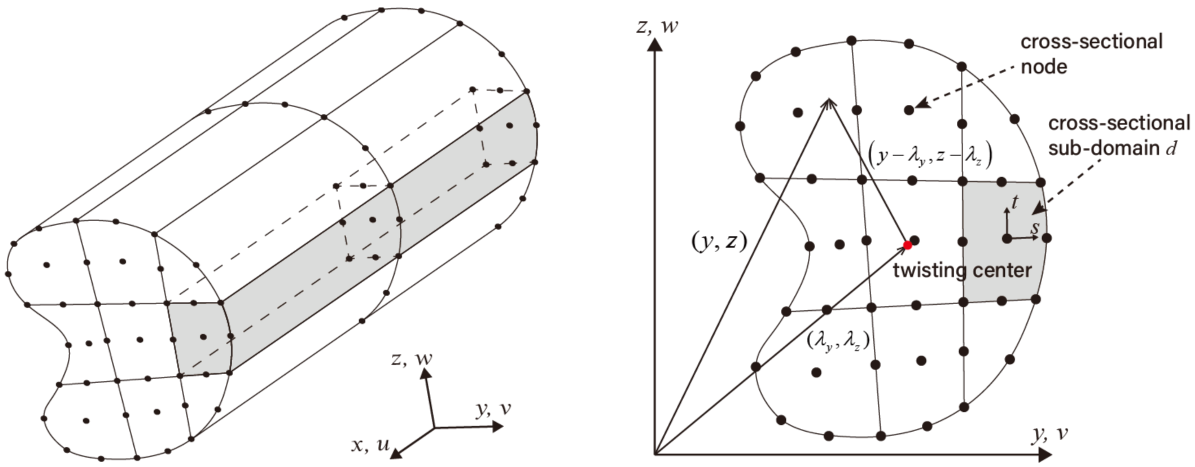

(a) (b)

Figure 2-2. (a) Description of arbitrary shaped, prismatic straight beam with sub-beam elements. (b) Cross-section with sub-beam element mesh.

For a sub-element *d*, Eq. (2-14) would be discretized as,

$$\sum_{d=1}^{q}\left[\int_{\Omega^{(d)}} \nabla(h_i\delta f_i)\nabla(G^{(d)}h_j f_j)\,d\Omega^{(d)}\right]$$

$$=\sum_{d=1}^{q}\left[\int_{\partial\Omega^{(d)}}\left(G^{(d)}\left(z-\lambda_z\right)n_y-G^{(d)}\left(y-\lambda_y\right)n_z\right)h_i\delta f_i\,d\partial\Omega^{(d)}\right]\ \text{ in }\ \Omega^{(d)}. \tag{2-15}$$

Eq. (2-15) holds for arbitrary warping function δf_i, therefore,

$$\sum_{d=1}^{q}\left[\int_{\Omega^{(d)}}\nabla(h_i)\nabla(G^{(d)}h_jf_j)\,d\Omega^{(d)}\right]$$

$$=\sum_{d=1}^{q}\left[\int_{\partial\Omega^{(d)}}\left(G^{(d)}\left(z-\lambda_z\right)n_y-G^{(d)}\left(y-\lambda_y\right)n_z\right)h_i\,d\partial\Omega^{(d)}\right]. \tag{2-16}$$

Yoon [21] proposed this formulation which can find both warping function and twisting center for composite beam model at the same time. It can be expressed in matrix form of,

$$\mathbf{K}_w\mathbf{F}-\mathbf{N}_z\lambda_y+\mathbf{N}_y\lambda_z=\mathbf{B}, \tag{2-17}$$

where,

$$\left[\mathbf{K}_w\right]_{ij}=\sum_{d=1}^{n}\left[\int_{\Omega^{(d)}}G^{(d)}(\nabla h_i)(\nabla h_j)\,d\Omega^{(d)}\right], \tag{2-18a}$$

$$\left[\mathbf{N}_z\right]_i=\sum_{d=1}^{n}\left[\int_{\partial\Omega^{(d)}}G^{(d)}n_z\,h_i\,d\partial\Omega^{(d)}\right], \tag{2-18b}$$

$$\left[\mathbf{N}_y\right]_i=\sum_{d=1}^{n}\left[\int_{\partial\Omega^{(d)}}G^{(d)}n_y\,h_i\,d\partial\Omega^{(d)}\right], \tag{2-18c}$$

$$\left[\mathbf{B}\right]_i=\sum_{d=1}^{n}\left[\int_{\partial\Omega^{(d)}}G^{(d)}(zn_y-yn_z)\,h_i\,d\partial\Omega^{(d)}\right]. \tag{2-18d}$$

are the components of matrices and vector $\mathbf{K}_w$, $\mathbf{N}_z$, $\mathbf{N}_y$, and $\mathbf{B}$, respectively, and λ_x, λ_y, $\left[\mathbf{F}\right]_j=f_j$ are the variables to solve.

Orthogonality condition of warping mode needs to be applied, in order to avoid singular problem in Eq. (2-16). 2-bending mode and 1-axial mode should be orthogonal to warping function.

$$\sum_{d=1}^{q}\left[\int_{\Omega^{(d)}}(f_i\,\mathbf{e}_x)\bullet(\vec{\mathbf{1}}\,\mathbf{e}_x)\,d\Omega^{(d)}\right]=0, \tag{2-19a}$$

$$\sum_{d=1}^{q}\left[\int_{\Omega^{(d)}}(f_i\,\mathbf{e}_x)\bullet(y\vec{\mathbf{1}}\,\mathbf{e}_x)\,d\Omega^{(d)}\right]=0, \tag{2-19b}$$

$$\sum_{d=1}^{q}\left[\int_{\Omega^{(d)}}(f_i\,\mathbf{e}_x)\bullet(z\vec{\mathbf{1}}\,\mathbf{e}_x)\,d\Omega^{(d)}\right]=0, \tag{2-19c}$$

where $\vec{\mathbf{1}}$ stands for vector with all 1 inside.

Orthogonality condition of warping functions are,

$$\mathbf{H}_x=0, \tag{2-20a}$$

$$\mathbf{H}_y=0, \tag{2-20b}$$

$$\mathbf{H}_z = 0 \,, \tag{2-20c}$$

where,

$$\left[\mathbf{H}_x\right]_i = \sum_{d=1}^{q}\left[\int_{\Omega^{(d)}} f_i \, d\Omega^{(d)}\right], \tag{2-21a}$$

$$\left[\mathbf{H}_y\right]_i = \sum_{d=1}^{q}\left[\int_{\Omega^{(d)}} y \, f_i \, d\Omega^{(d)}\right], \tag{2-21b}$$

$$\left[\mathbf{H}_z\right]_i = \sum_{d=1}^{q}\left[\int_{\Omega^{(d)}} z \, f_i \, d\Omega^{(d)}\right], \tag{2-21c}$$

are the components of matrices $\mathbf{H}_x$, $\mathbf{H}_y$, and $\mathbf{H}_z$, respectively.

Combining all these equations, for solving warping function and twisting center for arbitrary composite beam,

$$\begin{bmatrix} \mathbf{K}_w & -\mathbf{N}_z & \mathbf{N}_y \\ \mathbf{H}_x & \mathbf{0} & \mathbf{0} \\ \mathbf{H}_y & \mathbf{0} & \mathbf{0} \\ \mathbf{H}_z & \mathbf{0} & \mathbf{0} \end{bmatrix} \begin{bmatrix} \mathbf{F} \\ \lambda_y \\ \lambda_z \end{bmatrix} = \begin{bmatrix} \mathbf{B} \\ \mathbf{0} \\ \mathbf{0} \\ \mathbf{0} \end{bmatrix}. \tag{2-22}$$

Formulation above provides linear equation to solve warping function $\mathbf{F}$ and twisting center (λ_y, λ_z) at the same time.

2.2 Continuum Mechanics Based Beam Element

In this section, we present the implementation of warping function in finite element beam. Well known continuum mechanics based beam element, which is directly degenerated from solid element, has been used []. As shown in **Fig. 2-3(a)**, the beam can be discretized with partitioned sub-beams, which enables beam to model arbitrary complicated shape or multi-material composite beam. This degenerated beam element is graphically presented in **Fig. 2-3(b)**.

Several coordinate systems are introduced to present beam element. The spatial coordinate (*x,y,z*) is the fixed global 3-D Cartesian coordinate from the origin, whereas material coordinate (*r,s,t*) is the local 3-D curvilinear coordinate spanned inside the beam element, see **Fig. 2-3(b)**. The director vectors, $\mathbf{V}_{\bar{x}}$, $\mathbf{V}_{\bar{y}}$, and $\mathbf{V}_{\bar{z}}$ are orthonormal vectors, defining cross-sections. In material coordinate, the direction *r* is defined as the tangential direction of beam, and direction of *s* and *t* are defined as tangential to director vectors $\mathbf{V}_{\bar{x}}$ and $\mathbf{V}_{\bar{y}}$, respectively. Remark that the direction of *r* does not necessarily be orthogonal to *s*-*t* plane, which allows shear strain. Local 2-D Cartesian coordinate (*s*,*t*) on each cross-section *k* is defined at the beam node *k* with director vectors $\mathbf{V}_{\bar{x}}^k$ and $\mathbf{V}_{\bar{y}}^k$ as a basis, see **Fig. 2-3(d)**.

As shown in **Fig. 2-3(b)**, the global position vector of a given material point (*r,s,t*) of sub-beam element *d*,

$\mathbf{x}^{(d)}(r,s,t)$, is given as,

$$\mathbf{x}^{(d)}(r,s,t)=\sum_{k}H_k(r)\,\mathbf{x}_k^{(d)}(s,t)\,, \tag{2-23}$$

where $H_k(r)$ is the 1-D interpolation function along r, and $\mathbf{x}_k^{(d)}(s,t)$ is the global position vector of a given material point (s,t) of sub-beam element d, at node k.

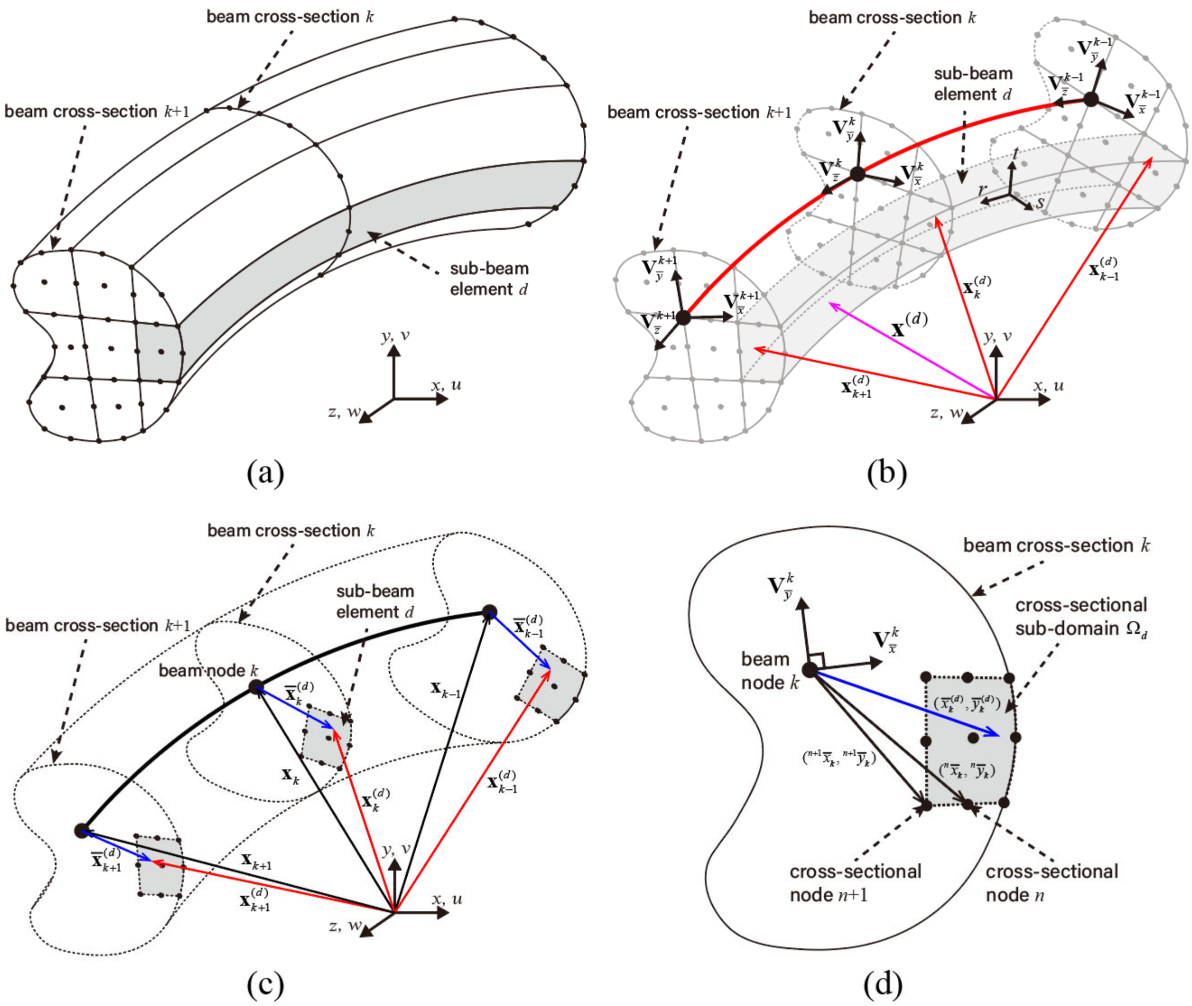

Figure 2-3. Description of arbitrary curved beam with sub-elements. (a) Description with sub-beams, (b) description with nodes and director vectors, (c) cross-sectional position vectors from origin, (d) cross-sectional position vector from beam node k.

As shown in **Fig. 2-3(c)**, $\mathbf{x}_k^{(d)}(s,t)$ is the summation of two position vectors,

$$\mathbf{x}_k^{(d)}(s,t)=\mathbf{x}_k+\bar{\mathbf{x}}_k^{(d)}(s,t)\,, \tag{2-24}$$

where $\mathbf{x}_k$ is the global position vector of node k, and $\bar{\mathbf{x}}_k^{(d)}(s,t)$ is the position vector of a given point (s,t) of sub-beam element d origin from node k. $\overline{\mathbf{x}}_k^{(d)}(s,t)$ is interpolated from 2-D interpolation function ${}^n h_k(s,t)$ with cross-sectional nodal position ${}^n\overline{\mathbf{x}}_k^{(d)}$ origin from node k, see **Fig. 2-3(d)**.

$$\overline{\mathbf{x}}_k^{(d)}(s,t) = \sum_{n\in\Omega_d} {}^n h_k(s,t)\, {}^n\overline{\mathbf{x}}_k \,, \tag{2-25}$$

As shown in **Fig. 2-3(d)**, $({}^n\overline{x}_k, {}^n\overline{y}_k)$ is the local coordinate of cross-sectional node n, defined by local 2-D Cartesian coordinate with basis vectors $\mathbf{V}_{\overline{x}}^k$ and $\mathbf{V}_{\overline{y}}^k$ on cross-section k, therefore, ${}^n\overline{\mathbf{x}}_k = {}^n\overline{x}_k \mathbf{V}_{\overline{x}}^k + {}^n\overline{y}_k \mathbf{V}_{\overline{y}}^k$.(2-26)

Combining Eqs. (2-24), (2-25), (2-26), and (2-27), the final form of position vector of continuum mechanics based beam is,

$$\mathbf{x}^{(d)}(r,s,t) = \sum_k H_k(r)\left(\mathbf{x}_k + \sum_{n\in\Omega_d} {}^n h_k(s,t)\left({}^n\overline{x}_k \mathbf{V}_{\overline{x}}^k + {}^n\overline{y}_k \mathbf{V}_{\overline{y}}^k \right) \right). \tag{2-27}$$

2.3 Enrichment of Warping Displacement Field

For sub-beam element d, the new enriched beam position field ${}^e\mathbf{x}^{(d)}(r,s,t)$ is obtained by combining warping position field ${}^w\mathbf{x}^{(d)}(r,s,t)$ to conventional beam position field $\mathbf{x}^{(d)}(r,s,t)$. The enrichment warping field ${}^w\mathbf{x}^{(d)}(r,s,t)$ is interpolated from cross-sectional nodal warping values, ${}^n\tilde{f}_k$, with $\mathbf{V}_{\overline{z}}^k$ direction. To maintain kinematic compatibility, we use same interpolation function, therefore,

$${}^w\mathbf{x}^{(d)}(r,s,t) = \sum_k H_k(r)\left(\sum_{n\in\Omega_d} {}^n h_k(s,t)\, {}^n\tilde{f}_k\, \mathbf{V}_{\overline{z}}^k \right). \tag{2-28}$$

As we discussed from previous section, shape of warping function is pre-calculated free warping function ${}^n f_k$ from St. Venant equation, and its magnitude is proportional to additional independent degree-of-freedom, α_k. The enrichment warping field with one degree-of-freedom per cross-section k become,

$${}^w\mathbf{x}^{(d)}(r,s,t) = \sum_k H_k(r)\left(\sum_{n\in\Omega_d} {}^n h_k(s,t)\, {}^n f_k\, \mathbf{V}_{\overline{z}}^k\, \alpha_k \right). \tag{2-29}$$

The final form of new enriched position field with warping for sub-beam element d is,

$$\begin{aligned}
{}^e\mathbf{x}^{(d)}(r,s,t) &= \mathbf{x}^{(d)}(r,s,t) + {}^w\mathbf{x}^{(d)}(r,s,t) \\
&= \sum_k H_k(r)\left(\mathbf{x}_k + \sum_{n\in\Omega_d} {}^n h_k(s,t)\left({}^n\overline{x}_k \mathbf{V}_{\overline{x}}^k + {}^n\overline{y}_k \mathbf{V}_{\overline{y}}^k \right) \right) + \sum_k H_k(r)\left(\sum_{n\in\Omega_d} {}^n h_k(s,t)\, {}^n f_k\, \mathbf{V}_{\overline{z}}^k \right)\alpha_k \\
&= \sum_k H_k(r)\left(\mathbf{x}_k + \sum_{n\in\Omega_d} {}^n h_k(s,t)\left({}^n\overline{x}_k \mathbf{V}_{\overline{x}}^k + {}^n\overline{y}_k \mathbf{V}_{\overline{y}}^k + {}^n f_k\, \mathbf{V}_{\overline{z}}^k\, \alpha_k \right) \right).
\end{aligned} \tag{2-30}$$

The displacement field would be the difference between position field at time t and at time 0,

$$
{}^{e}\mathbf{u}^{(d)}(r,s,t) = {}^{e}_{t}\mathbf{x}^{(d)}(r,s,t) - {}^{e}_{0}\mathbf{x}^{(d)}(r,s,t)
$$

$$
= \sum_{k} H_k(r)\left(\left({}_{t}\mathbf{x}_k - {}_{0}\mathbf{x}_k\right) + \sum_{n\in\Omega_d} {}^{n}h_k(s,t)\left({}^{n}\overline{x}_k \left({}_{t}\mathbf{V}_{\overline{x}}^{k} - {}_{0}\mathbf{V}_{\overline{x}}^{k}\right) + {}^{n}\overline{y}_k \left({}_{t}\mathbf{V}_{\overline{y}}^{k} - {}_{0}\mathbf{V}_{\overline{y}}^{k}\right) + {}^{n}f_k\, \mathbf{V}_{\overline{z}}^{k}\left({}_{t}\alpha_k - {}_{0}\alpha_k\right)\right)\right)
$$

$$
= \sum_{k} H_k(r)\left(\mathbf{u}_k + \sum_{n\in\Omega_d} {}^{n}h_k(s,t)\left({}^{n}\overline{x}_k \left({}^{t}_{0}\mathbf{R}^{k} - \mathbf{I}\right)\mathbf{V}_{\overline{x}}^{k} + {}^{n}\overline{y}_k \left({}^{t}_{0}\mathbf{R}^{k} - \mathbf{I}\right)\mathbf{V}_{\overline{y}}^{k} + {}^{n}f_k\, \mathbf{V}_{\overline{z}}^{k}\, {}^{t}_{0}\alpha_k\right)\right), \tag{2-31}
$$

where ${}^{t}_{0}\mathbf{R}^{k}$ is rotation matrix of cross-section plane k from time 0 to t, satisfying relation ${}_{t}\mathbf{V}^{k} = {}^{t}_{0}\mathbf{R}^{k}\,{}_{0}\mathbf{V}^{k}$ between same vectors in different time.

For rotation matrix $\mathbf{R}(\boldsymbol{\theta})$ and rotation angle vector $\boldsymbol{\theta}$, exponential map for SO(3) is,

$$
\mathbf{R}(\boldsymbol{\theta}) = \exp(\hat{\boldsymbol{\theta}}) = \mathbf{I} + \hat{\boldsymbol{\theta}} + \frac{1}{2!}\hat{\boldsymbol{\theta}}^2 + \cdots + \frac{1}{n!}\hat{\boldsymbol{\theta}}^n + \cdots, \tag{2-32}
$$

where $\hat{\mathbf{v}}$ is the skew-symmetric matrix of vector $\mathbf{v}$,

$$
\hat{\mathbf{v}} = \begin{bmatrix} 0 & -v_z & v_y \\ v_z & 0 & -v_x \\ -v_y & v_x & 0 \end{bmatrix} \quad \text{for} \quad \mathbf{v} = [v_x, v_y, v_z]^T. \tag{2-33}
$$

If rotation is small, rotation matrix can be approximated as,

$$
\mathbf{R}(\boldsymbol{\theta}) \approx \mathbf{I} + \hat{\boldsymbol{\theta}}. \tag{2-34}
$$

Apply Eq. (2-34) to Eq. (2-31), the displacement field become linearized as follow,

$$
{}^{e}\mathbf{u}^{(d)}(r,s,t) = \sum_{k} H_k(r)\left(\mathbf{u}_k + \sum_{n\in\Omega_d} {}^{n}h_k(s,t)\left({}^{n}\overline{x}_k\, {}^{t}_{0}\hat{\boldsymbol{\theta}}\,\mathbf{V}_{\overline{x}}^{k} + {}^{n}\overline{y}_k\, {}^{t}_{0}\hat{\boldsymbol{\theta}}\,\mathbf{V}_{\overline{y}}^{k} + {}^{n}f_k\, \mathbf{V}_{\overline{z}}^{k}\, {}^{t}_{0}\alpha_k\right)\right)
$$

$$
= \sum_{k} H_k(r)\left(\mathbf{u}_k + \sum_{n\in\Omega_d} {}^{n}h_k(s,t)\left(-{}^{n}\overline{x}_k\, \hat{\mathbf{V}}_{\overline{x}}^{k}\, {}^{t}_{0}\boldsymbol{\theta} - {}^{n}\overline{y}_k\, \hat{\mathbf{V}}_{\overline{y}}^{k}\, {}^{t}_{0}\boldsymbol{\theta} + {}^{n}f_k\, \mathbf{V}_{\overline{z}}^{k}\, {}^{t}_{0}\alpha_k\right)\right)
$$

$$
= \mathbf{L}^{(d)}(r,s,t)\,\mathbf{U}, \tag{2-35}
$$

where $\mathbf{u}_k$, ${}^{t}_{0}\boldsymbol{\theta}$, and ${}^{t}_{0}\alpha_k$ are the degree-of-freedom concerning with translation, rotation and warping, respectively. $\mathbf{L}^{(d)}(r,s,t)$ is the displacement interpolation matrix, and $\mathbf{U}$ is the beam element's displacement variable vector, $\mathbf{U} = [\cdots\ u_k\ v_k\ w_k\ \theta_x^k\ \theta_y^k\ \theta_z^k\ \cdots]^T$.

The Green-Lagrange strain in curvilinear material coordinate with respect to time 0 to t is,

$$
{}^{t}_{0}\varepsilon_{ij}^{(d)} = \frac{1}{2}\left({}^{t}\mathbf{g}_i^{(d)} \cdot {}^{t}\mathbf{g}_j^{(d)} - {}^{0}\mathbf{g}_i^{(d)} \cdot {}^{0}\mathbf{g}_j^{(d)} \right) \quad \text{with} \quad \mathbf{g}_i^{(d)} = \frac{d\mathbf{x}^{(d)}}{dr_i}, \tag{2-36}
$$

where $r_1 = r$, $r_2 = s$, $r_3 = t$ are the curvilinear coordinate defined above. For simplicity of Gaussian quadrature, which will be shown later, coordinate transformation from curvilinear material coordinate to local

Cartesian coordinate is applied.

The basis vector notation of Green-Lagrange strain with respect to covariant basis $\mathbf{g}_i$ from material coordinate, and orthonormal basis $\mathbf{t}_i$ from local Cartesian coordinate is,

$${}_0^t\bar{\varepsilon}_{ij}\left({}^0\mathbf{t}_i \otimes {}^0\mathbf{t}_j\right) = {}_0^t\varepsilon_{nm}\left({}^0\mathbf{g}^n \otimes {}^0\mathbf{g}^m\right), \tag{2-37}$$

where ${}_0^t\varepsilon_{nm}$ is the covariant component with respect to contravariant basis $\mathbf{g}^n$, which satisfy relation between covariant basis,

$${}^0\mathbf{g}^i \cdot {}^0\mathbf{g}_j = \delta_j^i \text{ with Kronecker delta } \delta_j^i \text{ (1 if } i = j\text{, and 0 others).} \tag{2-38}$$

${}_0^t\bar{\varepsilon}_{ij}$ is the strain component with orthonormal basis, ${}^0\mathbf{t}_i$, interpolated from director vectors,

$${}^0\mathbf{t}_1 = H_k(r)\mathbf{V}_{\bar{x}}^k / \left\| H_k(r)\mathbf{V}_{\bar{x}}^k \right\|, \tag{2-39a}$$

$${}^0\mathbf{t}_2 = H_k(r)\mathbf{V}_{\bar{y}}^k / \left\| H_k(r)\mathbf{V}_{\bar{y}}^k \right\|, \tag{2-39b}$$

$${}^0\mathbf{t}_3 = H_k(r)\mathbf{V}_{\bar{z}}^k / \left\| H_k(r)\mathbf{V}_{\bar{z}}^k \right\|. \tag{2-39c}$$

Result of coordinate transformation would be,

$${}_0^t\bar{\varepsilon}_{ij} = {}_0^t\varepsilon_{nm}\left({}^0\mathbf{t}_i \cdot {}^0\mathbf{g}^n\right)\left({}^0\mathbf{t}_j \cdot {}^0\mathbf{g}^m\right). \tag{2-40}$$

Linear term of Green-Lagrange strain with respect to displacement is,

$${}_0^t e_{ij} = \frac{1}{2}\left({}^t\mathbf{g}_i \cdot {}^t\mathbf{u}_{,j} - {}^0\mathbf{g}_i \cdot {}^0\mathbf{u}_{,j}\right) \text{ with } \mathbf{u}_{,i} = \frac{d\mathbf{u}}{dr_i}. \tag{2-41}$$

When enriched displacement field from Eq. (2-35) is applied,

$${}_0^t e_{ij} = \frac{1}{2}\left({}^t\mathbf{g}_i \cdot {}^t\mathbf{L}_{,j}\mathbf{U} - {}^0\mathbf{g}_i \cdot {}^0\mathbf{L}_{,j}\mathbf{U}\right) = {}_0^t\mathbf{B}_{ij}\mathbf{U} \text{ with } \mathbf{L}_{,i} = \frac{d\mathbf{L}}{dr_i}, \tag{2-42}$$

linear term of Green-Lagrange strain is linearized with the strain-displacement matrix, ${}_0^t\mathbf{B}$.

When coordinate transformation from covariant basis $\mathbf{g}_i$ to orthonormal basis $\mathbf{t}_i$ is applied, the strain-displacement matrix with respect to orthogonal basis is,

$${}_0^t\bar{e}_{ij} = {}_0^t\mathbf{B}_{nm}\left({}^0\mathbf{t}_i \cdot {}^0\mathbf{g}^n\right)\left({}^0\mathbf{t}_j \cdot {}^0\mathbf{g}^m\right)\mathbf{U} = {}_0^t\bar{\mathbf{B}}_{ij}\mathbf{U}. \tag{2-43}$$

The stiffness matrix is obtained by principle of virtual work [28, 29], which is,

$$\mathbf{K}^{(d)} = \int_{(d)} {}_0^t\mathbf{B}^{(d)^T}\, \mathbf{C}^{(d)}\, {}_0^t\mathbf{B}^{(d)}\, dV^{(d)} = \int_{(d)} {}_0^t\bar{\mathbf{B}}^{(d)^T}\, \bar{\mathbf{C}}^{(d)}\, {}_0^t\bar{\mathbf{B}}^{(d)}\, dV^{(d)}$$

$$= \int_{(d)} {}_0^t\bar{\mathbf{B}}_{ij}^{(d)^T}\, \bar{\mathbf{C}}_{ijnm}^{(d)}\, {}_0^t\bar{\mathbf{B}}_{nm}^{(d)}\, dV^{(d)}, \tag{2-44}$$

where $\bar{\mathbf{C}}_{ijnm}^{(d)}$ is the material law in orthonormal basis.

It is notable that displacement field of Eq. (2-35) is interpolated by same unknown variable vector $\mathbf{U}$, regardless of sub-element d,

$$ {}^{e}\mathbf{u}(r,s,t) = \sum_{d=1}^{q} {}^{e}\mathbf{u}^{(d)}(r,s,t) \,. \tag{2-45} $$

It proves that stiffness matrix of a sub-beam element is independent to other the sub-beam elements. Therefore, we can build total stiffness matrix of all sub-beam elements, by simply adding all stiffness matrix from each node, which is,

$$ \mathbf{K} = \sum_{d=1}^{q} \mathbf{K}^{(d)} = \sum_{d=1}^{q} \int_{(d)} {}_{0}^{t}\overline{\mathbf{B}}_{ij}^{(d)^{T}} \, \overline{\mathbf{C}}_{ijnm}^{(d)} \, {}_{0}^{t}\overline{\mathbf{B}}_{nm}^{(d)} \, dV^{(d)} \,. \tag{2-46} $$

Note that, the locations of the twisting centers do not necessarily need to be added inside the formulation. It is due to the fact that the continuum mechanics based beam element automatically satisfies the compatibility condition of the displacement field by interpolating nodal information into elemental space. If the displacement basis functions of the beam element can depict the solution space close enough, we will be able to get approximated displacement field close enough. In this case, the choice of warping function is the choice of displacement basis function, and the magnitude of each basis function is independent to each other due to independent DOFs. However, for beams with discontinuity, choice of warping function between adjacent beam elements can occur gap and overlap and cannot be overcome with independent DOFs. Details will be discussed in next chapter.

Chapter 3. Direct Calculation of Interface Warping Mode

3.1 Interface Warping Function

Fig. 3-1 shows an example of a beam with cross-sectional discontinuity and its warping functions. The beam has three different cross-sections: ①, ②, and an interface cross-section between them. The classical Saint-Venant torsion theory provides free warping functions for continuous cross-sections, as shown in **Fig. 3-1(b)**. However, it is difficult to calculate the warping functions at an interface cross-section where discontinuity occurs. The main reason is that the cross-sections adjacent to the interface can have different geometric and material properties, but the classical Saint-Venant theory can only handle continuous cross-sections.

Here, we present a new method to calculate the interface warping functions. Considering the longitudinal direction, the classical Saint-Venant torsion theory given in the 2D domain is extended to a 3D domain. The governing equations in strong and weak forms are derived and finite element discretization is obtained to numerically calculate the interface warping functions.

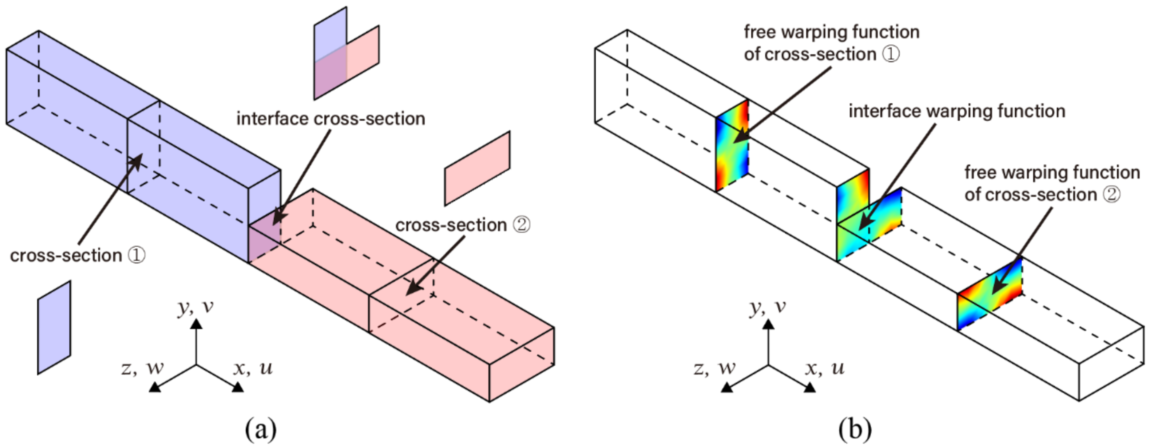

Figure 3-1. Beam with a discontinuously varying cross-section. (a) Cross-sections ① and ②, and the interface cross-section between them. (b) Free warping functions of cross-sections ① and ②, and the interface warping function at the interface cross-section.

3.2 Governing Equation and Its Boundary Condition

Let us consider a straight infinite beam subjected to torsion. The beam can have both material and geometric discontinuities in the middle; thus, its twisting center can vary. **Fig. 3-2(a)** shows the beam domain Ω near the discontinuity, and the global Cartesian coordinate system is defined where the x-direction and the yz-plane are normal and parallel to the cross-sections, respectively. Assume that cross-sectional warping is allowed, but cross-sectional in-plane distortion is neglected.

3.2.1 Kinematics

Let us consider a cross-section rigidly rotating around its twisting center (λ_y, λ_z), as shown in **Fig. 3-2(b)**. The corresponding displacements *u*, *v*, and *w* are defined with the following relations

$$u = f\alpha\ ,\ \ \frac{\partial v}{\partial x} = -\bar{z}\alpha\ ,\ \ \frac{\partial w}{\partial x} = \bar{y}\alpha\ , \tag{3-1}$$

where $\bar{y} = y - \lambda_y(x)$, $\bar{z} = z - \lambda_z(x)$, and $f(x, y, z)$ is the warping function, and $\alpha(x) = \partial\theta_x / \partial x$ is the twist rate which is the angle of twist per unit length along the *x*-direction [3,18].

Without body force, the equilibrium equation of beam domain Ω is written as

$$\frac{\partial \sigma_{xx}}{\partial x} + \frac{\partial \sigma_{yx}}{\partial y} + \frac{\partial \sigma_{zx}}{\partial z} = 0 \ \text{ in } \ \Omega\ , \tag{3-2}$$

where σ_{xx}, σ_{yx}, and σ_{zx} are non-zero stress components.

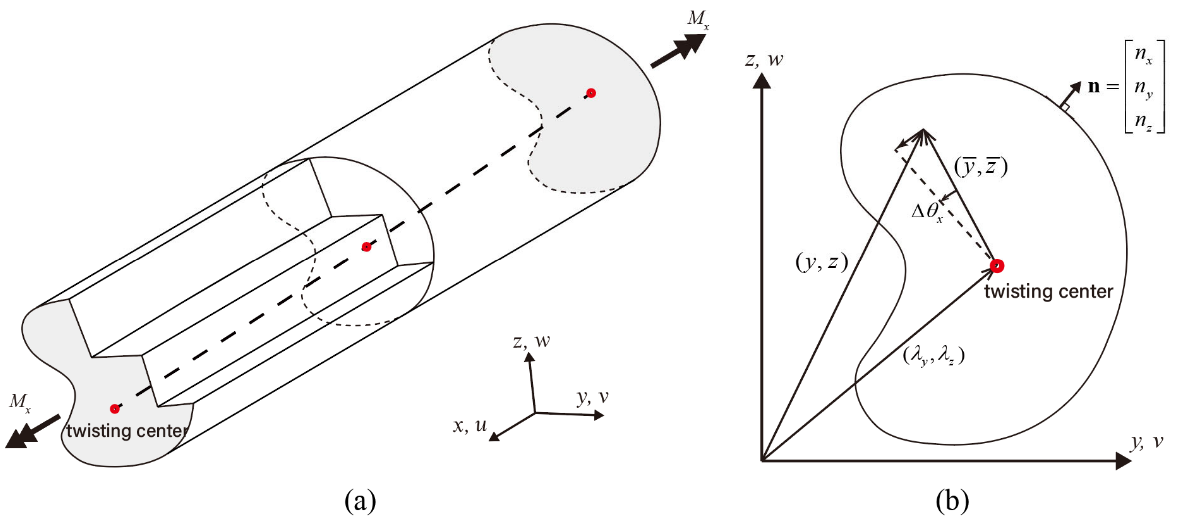

Figure 3-2. Illustration of a straight beam with discontinuity. (a) Global coordinate system and varying twisting center. (b) Cross-section with twisting center.

Fig. 3-2(a) also illustrates two different boundaries. The cross-sectional boundaries, positioned at both ends of the domain (gray colored), are normal to the *x*-axis and exposed to a torsional moment M_x. Although discontinuity exists in the middle, for a 'sufficiently (or infinitely)' long domain Ω, Saint Venant's principle guarantees that the *x*-directional component of traction (T_x) becomes zero on the cross-sectional boundaries.

The rest of the boundaries are where no external force and traction vector exist: the x-directional component of traction (T_x) becomes zero on all boundaries

$$T_x = \sigma_{xx} n_x + \sigma_{yx} n_y + \sigma_{zx} n_z = 0 \quad \text{on} \quad \Gamma, \tag{3-3}$$

in which n_x, n_y, and n_z are components of the unit vector ($\mathbf{n} = n_x \mathbf{e}_x + n_y \mathbf{e}_y + n_z \mathbf{e}_z$) normal to the boundary Γ.

Considering the linear elastic isotropic material law and the strain-displacement relation, the following equations are obtained

$$\sigma_{xx} = E\varepsilon_{xx} = E\frac{\partial u}{\partial x}, \tag{3-4a}$$

$$\sigma_{yx} = G\gamma_{yx} = G\left(\frac{\partial u}{\partial y} + \frac{\partial v}{\partial x}\right), \tag{3-4b}$$

$$\sigma_{zx} = G\gamma_{zx} = G\left(\frac{\partial u}{\partial z} + \frac{\partial w}{\partial x}\right), \tag{3-4c}$$

where G is the shear modulus, E is Young's modulus, and ε_{xx}, γ_{yx}, and γ_{zx} are strain components.

By incorporating Eq. (3-1) and Eqs. (3-4a)-(3-4c) into Eq. (3-2) and Eq. (3-3), we obtain

$$E\frac{\partial^2 u}{\partial x^2} + G\frac{\partial^2 u}{\partial y^2} + G\frac{\partial^2 u}{\partial z^2} = 0 \quad \text{in} \quad \Omega, \tag{3-5a}$$

$$G\left(\frac{E}{G}\frac{\partial u}{\partial x}n_x + \frac{\partial u}{\partial y}n_y + \frac{\partial u}{\partial z}n_z\right) = -G\left(\frac{\partial v}{\partial x}n_y + \frac{\partial w}{\partial x}n_z\right) \quad \text{on} \quad \Gamma. \tag{3-5b}$$

Note that the twisting center (λ_y, λ_z) can vary along the x-direction inside the domain Ω, as shown in **Fig. 3-2(a)**.

Unlike the classical Saint-Venant torsion theory, the longitudinal displacement u becomes a function of x, and $\partial u / \partial x$ is no longer zero near the discontinuity. However, for a 'sufficiently (or infinitely)' long domain Ω, Eq. (3-3) and Eq. (3-4a) show $\partial u / \partial x = 0$ on the cross-sectional boundaries where n_x is not zero. Therefore, using a coordinate transformation, Eqs. (3-5a)-(3-5b) can be rearranged into Laplace's equation with the Neumann boundary condition as follows

$$G\left(\frac{\partial^2 u}{\partial \hat{x}^2} + \frac{\partial^2 u}{\partial \hat{y}^2} + \frac{\partial^2 u}{\partial \hat{z}^2}\right) = 0 \quad \text{in} \quad \hat{\Omega}, \tag{3-6a}$$

$$G\left(\frac{\partial u}{\partial \hat{x}}\hat{n}_x + \frac{\partial u}{\partial \hat{y}}\hat{n}_y + \frac{\partial u}{\partial \hat{z}}\hat{n}_z\right) = -G\sqrt{\frac{G}{E}}\left(\frac{\partial v}{\partial \hat{x}}\hat{n}_y + \frac{\partial w}{\partial \hat{x}}\hat{n}_z\right) \quad \text{on} \quad \hat{\Gamma}, \tag{3-6b}$$

in which $\hat{x} = \sqrt{\frac{G}{E}}x$, $\hat{y} = y$, and $\hat{z} = z$ are new coordinates, and $\hat{\Omega}$ and $\hat{\Gamma}$ denote the corresponding transformed domain and its boundary, respectively.

3.2.2 Weak Form

The weak form of Eqs. (3-6a)-(3-6b) is derived with the virtual warping displacement field δu,

$$\int_{\hat{\Omega}} G\hat{\nabla}u\cdot\hat{\nabla}\delta u\, d\hat{\Omega} = -\int_{\hat{\Gamma}} G\sqrt{\frac{G}{E}}\left(\frac{\partial v}{\partial \hat{x}}\hat{n}_y + \frac{\partial w}{\partial \hat{x}}\hat{n}_z\right)\delta u\, d\hat{\Gamma}\,, \tag{3-7}$$

where $\hat{\nabla} = \frac{\partial}{\partial \hat{x}}\mathbf{e}_x + \frac{\partial}{\partial \hat{y}}\mathbf{e}_y + \frac{\partial}{\partial \hat{z}}\mathbf{e}_z$ is the del operator of the transformed coordinate.

Substituting Eq. (3-1) into Eq. (3-7), the variational form of the 3D Saint-Venant equation is obtained in the original coordinate system

$$\int_{\Omega} G\left(\frac{E}{G}\frac{\partial(f\alpha)}{\partial x}\frac{\partial \delta u}{\partial x} + \frac{\partial(f\alpha)}{\partial y}\frac{\partial \delta u}{\partial y} + \frac{\partial(f\alpha)}{\partial z}\frac{\partial \delta u}{\partial z}\right)d\Omega$$

$$= \int_{\Gamma} G\left(\alpha\lambda_y n_z - \alpha\lambda_z n_y\right)\delta u\, d\Gamma + \int_{\Gamma} G\alpha\left(zn_y - yn_z\right)\delta u\, d\Gamma\,. \tag{3-8}$$

The warping function f of Eq. (3-8) also contains stretching and bending modes. To extract only the warping mode, the following orthogonality conditions are applied,

$$\int_A E(1\mathbf{e}_x)\cdot(f\mathbf{e}_x)dA = 0\,, \tag{3-9a}$$

$$\int_A E(y\mathbf{e}_x)\cdot(f\mathbf{e}_x)dA = 0\,, \tag{3-9b}$$

$$\int_A E(z\mathbf{e}_x)\cdot(f\mathbf{e}_x)dA = 0\,, \tag{3-9c}$$

in which A is the area of the cross-section, perpendicular to the beam.

Resultant forces can be calculated on the cross-section

$$F_y = \int_A \sigma_{yx} dA = 0\,, \tag{3-10a}$$

$$F_z = \int_A \sigma_{zx} dA = 0\,, \tag{3-10b}$$

$$M_x = \int_A \left(\bar{y}\sigma_{zx} - \bar{z}\sigma_{yx}\right)dA = \int_A \left(y\sigma_{zx} - z\sigma_{yx}\right)dA - \lambda_y\int_A \sigma_{zx}dA + \lambda_z\int_A \sigma_{yx}dA\,, \tag{3-10c}$$

in which F_y and F_z are shear forces in the y- and z-directions, and M_x is the torsional moment about twisting center acting on cross-sectional area A.

Substituting Eqs. (3-10a) and (3-10b) into Eq. (3-10c), the following equation is obtained

$$M_x = \int_A \left(y\sigma_{zx} - z\sigma_{yx}\right)dA\,, \tag{3-11}$$

and using Eq. (3-1) and Eqs. (3-4b)-(3-4c) in Eq. (3-11) gives

$$M_x = \int_A G\left(y\frac{\partial(f\alpha)}{\partial z} - z\frac{\partial(f\alpha)}{\partial y} \right) dA - \alpha\lambda_y \int_A GydA - \alpha\lambda_z \int_A GzdA + \alpha\int_A G\left(y^2+z^2\right)dA \,. \tag{3-12}$$

3.3 Finite Element Discretization

To numerically calculate the interface warping function, here we present the finite element discretization of Eq. (3-8), Eqs. (3-9a)-(3-9c), and Eq. (3-12).

Let us introduce three unknown variables: $\tilde{\lambda}_y = \alpha\lambda_y$, $\tilde{\lambda}_z = \alpha\lambda_z$, and the warping displacement field $u = f\alpha$. Then, Eq. (3-8), Eqs. (3-9a)-(3-9c), and Eq. (3-12) become

$$\int_\Omega G\left(\frac{E}{G}\frac{\partial u}{\partial x}\frac{\partial \delta u}{\partial x} + \frac{\partial u}{\partial y}\frac{\partial \delta u}{\partial y} + \frac{\partial u}{\partial z}\frac{\partial \delta u}{\partial z} \right) d\Omega$$

$$= \int_\Gamma G\left(\tilde{\lambda}_y n_z - \tilde{\lambda}_z n_y\right)\delta u \, d\Gamma + \int_\Gamma G\alpha\left(zn_y - yn_z\right)\delta u \, d\Gamma \,, \tag{3-13a}$$

$$\int_A E(1\mathbf{e}_x)\cdot(u\mathbf{e}_x)dA = 0 \,, \tag{3-13b}$$

$$\int_A E(y\,\mathbf{e}_x)\cdot(u\mathbf{e}_x)dA = 0 \,, \tag{3-13c}$$

$$\int_A E(z\mathbf{e}_x)\cdot(u\mathbf{e}_x)dA = 0 \,, \tag{3-13d}$$

$$M_x = \int_A G\left(y\frac{\partial u}{\partial z} - z\frac{\partial u}{\partial y} \right) dA - \tilde{\lambda}_y \int_A GydA - \tilde{\lambda}_z \int_A GzdA + \alpha\int_A G\left(y^2+z^2\right)dA \,. \tag{3-13e}$$

The 3D beam domain Ω in **Fig. 3-2(a)** is discretized using a 3D finite element model, as shown in **Fig. 3-3(a)**

$$\Omega = \bigcup_{e=1}^{d} \Omega^{(e)} \,, \tag{3-14}$$

in which $\Omega^{(e)}$ denotes the 3D finite element domains and d is the number of finite elements used. Different material properties can be assigned in each finite element domain to model composite beams.

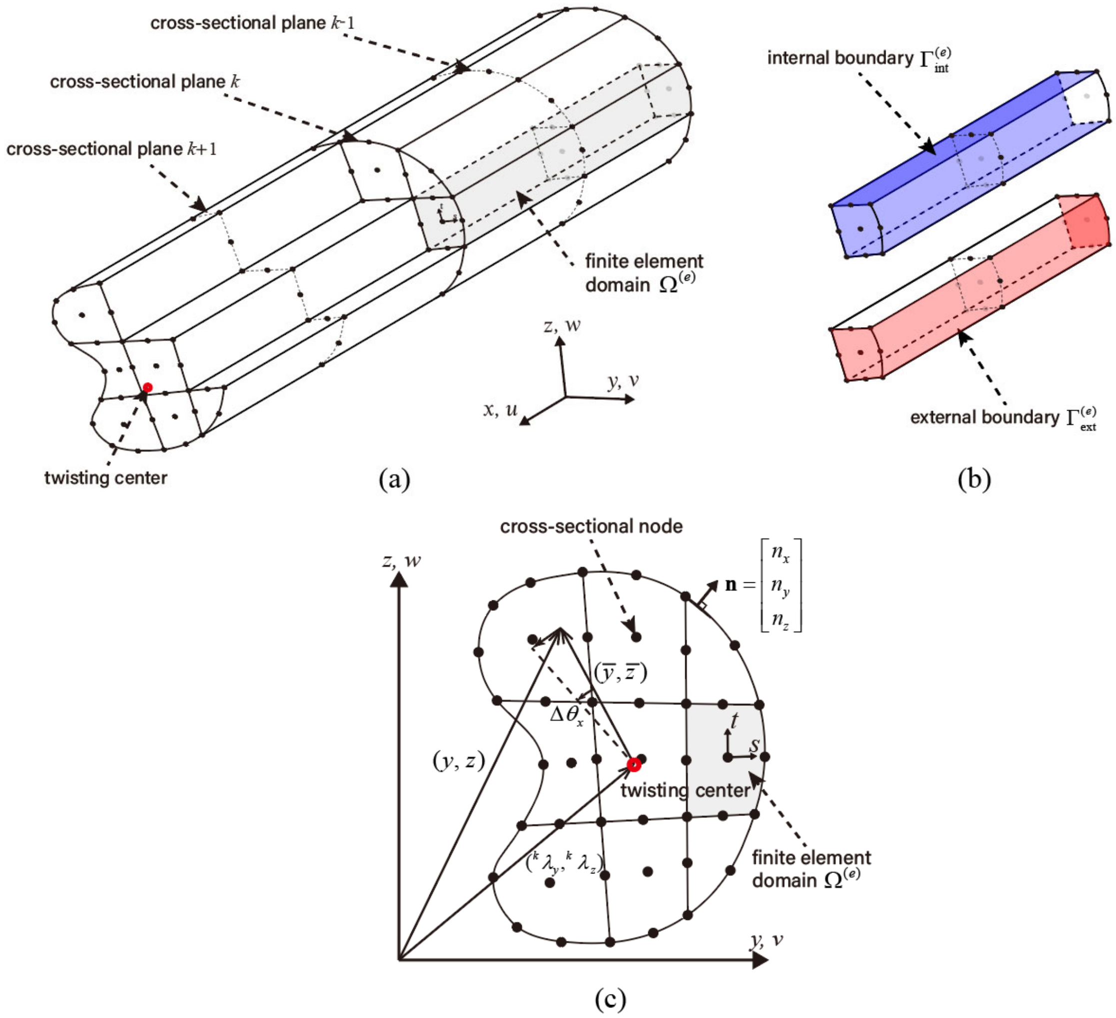

Figure 3-3. Discretization of the beam domain Ω for interface warping calculation. (a) Discretization of interface cross-section and its adjacent cross-sections. (b) Internal and external boundary of the finite element domain $\Omega^{(e)}$. (c) Discretized cross-section at beam node *k*.

Each domain $\Omega^{(e)}$ consists of a *p*-node solid element. The displacement function $u^{(e)}$ in the finite element domain $\Omega^{(e)}$ is interpolated as

$$u^{(e)}(x, y, z) = \mathbf{H}^{(e)}\mathbf{U}^{(e)} \tag{3-15}$$

with

$$\mathbf{U}^{(e)} = \left[u_1^{(e)}, \cdots, u_i^{(e)}, \cdots, u_p^{(e)}\right]^T, \tag{3-16a}$$

$$\mathbf{H}^{(e)} = \left[H_1(x, y, z), \cdots, H_i(x, y, z), \cdots, H_p(x, y, z)\right], \tag{3-16b}$$

where $u_i^{(e)}$ is the nodal warping displacement value at node *i*, $\mathbf{U}^{(e)}$ is the vector containing the nodal warping displacement values, $H_i(x, y, z)$ is the 3D shape functions corresponding to node *i*, and $\mathbf{H}^{(e)}$ is the matrix containing the shape functions.

Similarly, the virtual warping displacement field $\delta u^{(e)}$ is interpolated as

$$\delta u^{(e)}(x,y,z) = \mathbf{H}^{(e)}\delta\mathbf{U}^{(e)} \tag{3-17}$$

with

$$\delta\mathbf{U}^{(e)} = \left[\delta u_1^{(e)},\ \cdots,\ \delta u_i^{(e)},\ \cdots,\ \delta u_p^{(e)}\right]^T, \tag{3-18}$$

where $\delta\mathbf{U}^{(e)}$ is the vector containing the virtual nodal warping displacement values, $\delta u_i^{(e)}$.

Fig. 3(b) illustrates the internal and external boundaries of the finite element domain $\Omega^{(e)}$: $\Gamma^{(e)} = \Gamma_{\text{int}}^{(e)} \cup \Gamma_{\text{ext}}^{(e)}$ with internal boundary $\Gamma_{\text{int}}^{(e)}$ (colored in blue) and external boundary $\Gamma_{\text{ext}}^{(e)}$ (colored in red). The boundary of the entire domain Ω is denoted by

$$\Gamma = \bigcup_{e=1}^{d} \Gamma_{\text{ext}}^{(e)}. \tag{3-19}$$

Each cross-sectional plane of sub-beam *e* rotates around its twisting center, as shown in **Fig. 3-3(c)**. The variables $(\tilde{\lambda}_y, \tilde{\lambda}_z)$ are interpolated as

$$\tilde{\lambda}_y(x) = \mathbf{h}^{(e)}\tilde{\boldsymbol{\Lambda}}_y^{(e)},\quad \tilde{\lambda}_z(x) = \mathbf{h}^{(e)}\tilde{\boldsymbol{\Lambda}}_z^{(e)} \tag{3-20}$$

with

$$\tilde{\boldsymbol{\Lambda}}_y^{(e)} = \left[{}^1\tilde{\lambda}_y^{(e)},\ \cdots,\ {}^l\tilde{\lambda}_y^{(e)},\ \cdots,\ {}^q\tilde{\lambda}_y^{(e)}\right]^T, \tag{3-21a}$$

$$\tilde{\boldsymbol{\Lambda}}_z^{(e)} = \left[{}^1\tilde{\lambda}_z^{(e)},\ \cdots,\ {}^l\tilde{\lambda}_z^{(e)},\ \cdots,\ {}^q\tilde{\lambda}_z^{(e)}\right]^T, \tag{3-21b}$$

$$\mathbf{h}^{(e)} = \left[h_1(x),\ \cdots,\ h_l(x),\ \cdots,\ h_q(x)\right], \tag{3-21c}$$

where q is the number of the cross-sectional planes of sub-beam *e*, $({}^l\tilde{\lambda}_y^{(e)}, {}^l\tilde{\lambda}_z^{(e)})$ denotes the variables $(\tilde{\lambda}_y, \tilde{\lambda}_z)$ of the *l*th cross-sectional plane of sub-beam *e*, $\tilde{\boldsymbol{\Lambda}}_y^{(e)}$ and $\tilde{\boldsymbol{\Lambda}}_z^{(e)}$ are the vectors containing ${}^l\tilde{\lambda}_y^{(e)}$ and ${}^l\tilde{\lambda}_z^{(e)}$, respectively, and $\mathbf{h}^{(e)}$ is the matrix containing 1D shape functions, $h_l(x)$, corresponding to cross-sectional plane *l*.

Similarly, the twist rate α is interpolated using the same 1D shape function

$$\alpha(x) = \mathbf{h}^{(e)}\mathbf{A}^{(e)} \tag{3-22}$$

with

$$\mathbf{A}^{(e)} = \left[{}^1\alpha^{(e)},\ \cdots,\ {}^l\alpha^{(e)},\ \cdots,\ {}^q\alpha^{(e)}\right]^T, \tag{3-23}$$

where ${}^l\alpha^{(e)}$ denotes the twist rate of the *l*th cross-sectional plane of sub-beam *e*.

Using Eqs. (3-14)-(3-23) in Eq. (3-13a), the following finite element discretization is obtained

$$\delta\mathbf{U}^T \mathop{\mathsf{A}}_{e=1}^{d}\left[\int_{\Omega^{(e)}} G^{(e)}\left(\frac{E^{(e)}}{G^{(e)}}\frac{\partial\mathbf{H}^{(e)T}}{\partial x}\frac{\partial\mathbf{H}^{(e)}}{\partial x}+\frac{\partial\mathbf{H}^{(e)T}}{\partial y}\frac{\partial\mathbf{H}^{(e)}}{\partial y}+\frac{\partial\mathbf{H}^{(e)T}}{\partial z}\frac{\partial\mathbf{H}^{(e)}}{\partial z}\right)d\Omega\right]\mathbf{U}$$

$$-\delta\mathbf{U}^T \mathop{\mathsf{A}}_{e=1}^{d}\left[\int_{\Gamma_{\text{ext}}^{(e)}} G^{(e)}\mathbf{H}^{(e)T}\mathbf{h}^{(e)}\, n_z\, d\Gamma\right]\tilde{\boldsymbol{\Lambda}}_y$$

$$+\delta\mathbf{U}^T \mathop{\mathsf{A}}_{e=1}^{d}\left[\int_{\Gamma_{\text{ext}}^{(e)}} G^{(e)}\mathbf{H}^{(e)T}\mathbf{h}^{(e)}\, n_y\, d\Gamma\right]\tilde{\boldsymbol{\Lambda}}_z$$

$$+\delta\mathbf{U}^T \mathop{\mathsf{A}}_{e=1}^{d}\left[\int_{\Gamma_{\text{ext}}^{(e)}} G^{(e)}\left(-zn_y+yn_z\right)\mathbf{H}^{(e)T}\mathbf{h}^{(e)}\, d\Gamma\right]\mathbf{A}=\mathbf{0}\,, \tag{3-24}$$

where $\mathbf{U}$, $\delta\mathbf{U}$, $\tilde{\boldsymbol{\Lambda}}_y$, $\tilde{\boldsymbol{\Lambda}}_z$, and $\mathbf{A}$ are the vectors containing $\mathbf{U}^{(e)}$, $\delta\mathbf{U}^{(e)}$, $\tilde{\boldsymbol{\Lambda}}_y^{(e)}$, $\tilde{\boldsymbol{\Lambda}}_z^{(e)}$, and $\mathbf{A}^{(e)}$ of all finite element domains, respectively, and A is the assembly operator [29].

For an infinitely long domain, the change of warping displacements along the x-direction is negligible compared to the change along the y- and z-directions: $\frac{\partial\mathbf{H}}{\partial x}\ll\frac{\partial\mathbf{H}}{\partial y}$ and $\frac{\partial\mathbf{H}}{\partial x}\ll\frac{\partial\mathbf{H}}{\partial z}$,

$$\delta\mathbf{U}^T \mathop{\mathsf{A}}_{e=1}^{d}\left[\int_{\Omega^{(e)}} G^{(e)}\left(\frac{\partial\mathbf{H}^{(e)T}}{\partial y}\frac{\partial\mathbf{H}^{(e)}}{\partial y}+\frac{\partial\mathbf{H}^{(e)T}}{\partial z}\frac{\partial\mathbf{H}^{(e)}}{\partial z}\right)d\Omega\right]\mathbf{U}$$

$$-\delta\mathbf{U}^T \mathop{\mathsf{A}}_{e=1}^{d}\left[\int_{\Gamma_{\text{ext}}^{(e)}} G^{(e)}\mathbf{H}^{(e)T}\mathbf{h}^{(e)}\, n_z\, d\Gamma\right]\tilde{\boldsymbol{\Lambda}}_y$$

$$+\delta\mathbf{U}^T \mathop{\mathsf{A}}_{e=1}^{d}\left[\int_{\Gamma_{\text{ext}}^{(e)}} G^{(e)}\mathbf{H}^{(e)T}\mathbf{h}^{(e)}\, n_y\, d\Gamma\right]\tilde{\boldsymbol{\Lambda}}_z$$

$$+\delta\mathbf{U}^T \mathop{\mathsf{A}}_{e=1}^{d}\left[\int_{\Gamma_{\text{ext}}^{(e)}} G^{(e)}\left(-zn_y+yn_z\right)\mathbf{H}^{(e)T}\mathbf{h}^{(e)}\, d\Gamma\right]\mathbf{A}=\mathbf{0}\,. \tag{3-25}$$

Note that the length of the domain Ω no longer affects the solution of Eq. (3-25), because all the integrals in the equation are linearly proportional to the length of the domain. Therefore, the domain length can be arbitrarily chosen when calculating the interface warping functions.

By eliminating $\delta\mathbf{U}$ in Eq. (3-25), the following equation in matrix form is obtained

$$\mathbf{K}_w\mathbf{U}-\mathbf{N}_z\tilde{\boldsymbol{\Lambda}}_y+\mathbf{N}_y\tilde{\boldsymbol{\Lambda}}_z+\mathbf{B}_c\mathbf{A}=\mathbf{0} \tag{3-26}$$

with

$$\mathbf{K}_w=\mathop{\mathsf{A}}_{e=1}^{d}\left[\int_{\Omega^{(e)}} G^{(e)}\left(\frac{\partial\mathbf{H}^{(e)T}}{\partial y}\frac{\partial\mathbf{H}^{(e)}}{\partial y}+\frac{\partial\mathbf{H}^{(e)T}}{\partial z}\frac{\partial\mathbf{H}^{(e)}}{\partial z}\right)d\Omega\right], \tag{3-27a}$$

$$\mathbf{N}_z=\mathop{\mathsf{A}}_{e=1}^{d}\left[\int_{\Gamma_{\text{ext}}^{(e)}} G^{(e)}n_z\mathbf{H}^{(e)T}\,\mathbf{h}^{(e)}\, d\Gamma\right], \tag{3-27b}$$

$$\mathbf{N}_y=\mathop{\mathsf{A}}_{e=1}^{d}\left[\int_{\Gamma_{\text{ext}}^{(e)}} G^{(e)}n_y\mathbf{H}^{(e)T}\,\mathbf{h}^{(e)}\, d\Gamma\right], \tag{3-27c}$$

$$\mathbf{B}_c = \mathop{\mathrm{A}}\limits_{e=1}^{d}\left[\int_{\Gamma_{\text{ext}}^{(e)}} G^{(e)}\left(-zn_y + yn_z\right)\mathbf{H}^{(e)T}\mathbf{h}^{(e)}\, d\Gamma\right]. \tag{3-27d}$$

The orthogonality conditions of Eqs. (3-13b)-(3-13d) are also discretized and expressed in the matrix and vector forms

$$\mathbf{Q}_x\mathbf{U} = \mathbf{0}, \quad \mathbf{Q}_y\mathbf{U} = \mathbf{0}, \quad \mathbf{Q}_z\mathbf{U} = \mathbf{0} \tag{3-28}$$

with

$$\mathbf{Q}_x = \mathop{\mathrm{A}}\limits_{e=1}^{d}\left[\int_{\Omega^{(e)}} E^{(e)}\mathbf{H}_1^{(e)T}\, d\Omega, \cdots, \int_{\Omega^{(e)}} E^{(e)}\mathbf{H}_k^{(e)T}\, d\Omega, \cdots, \int_{\Omega^{(e)}} E^{(e)}\mathbf{H}_n^{(e)T}\, d\Omega\right]^T, \tag{3-29a}$$

$$\mathbf{Q}_y = \mathop{\mathrm{A}}\limits_{e=1}^{d}\left[\int_{\Omega^{(e)}} yE^{(e)}\mathbf{H}_1^{(e)T}\, d\Omega, \cdots, \int_{\Omega^{(e)}} yE^{(e)}\mathbf{H}_k^{(e)T}\, d\Omega, \cdots, \int_{\Omega^{(e)}} yE^{(e)}\mathbf{H}_n^{(e)T}\, d\Omega\right]^T, \tag{3-29b}$$

$$\mathbf{Q}_z = \mathop{\mathrm{A}}\limits_{e=1}^{d}\left[\int_{\Omega^{(e)}} zE^{(e)}\mathbf{H}_1^{(e)T}\, d\Omega, \cdots, \int_{\Omega^{(e)}} zE^{(e)}\mathbf{H}_k^{(e)T}\, d\Omega, \cdots, \int_{\Omega^{(e)}} zE^{(e)}\mathbf{H}_n^{(e)T}\, d\Omega\right]^T, \tag{3-29c}$$

where $\mathbf{H}_k^{(e)}$ is the 3D interpolation matrix $\mathbf{H}^{(e)}$ at cross-sectional plane *k*.

Eq. (3-13e) is discretized and expressed in matrix form as follow

$$\mathbf{R}_w\mathbf{U} - \mathbf{S}_y\tilde{\mathbf{\Lambda}}_y - \mathbf{S}_z\tilde{\mathbf{\Lambda}}_z + \mathbf{J}_x\mathbf{A} = M_x\mathbf{1} \tag{3-30}$$

with

$$\mathbf{R}_w = \mathop{\mathrm{A}}\limits_{e=1}^{d}\left[\mathbf{C}_1^{(e)},\ \mathbf{C}_2^{(e)},\ \cdots,\ \mathbf{C}_k^{(e)},\ \cdots, \mathbf{C}_n^{(e)}\right]^T, \tag{3-31a}$$

$$\mathbf{S}_y = \mathop{\mathrm{A}}\limits_{e=1}^{d}\left[\int_{\Omega^{(e)}} G^{(e)} y\, \mathbf{h}_k^{(e)T}\mathbf{h}_k^{(e)} d\Omega\right], \tag{3-31b}$$

$$\mathbf{S}_z = \mathop{\mathrm{A}}\limits_{e=1}^{d}\left[\int_{\Omega^{(e)}} G^{(e)} z\, \mathbf{h}_k^{(e)T}\mathbf{h}_k^{(e)} d\Omega\right], \tag{3-31c}$$

$$\mathbf{J}_x = \mathop{\mathrm{A}}\limits_{e=1}^{d}\left[\int_{\Omega^{(e)}} G^{(e)}(y^2 + z^2)\, \mathbf{h}_k^{(e)T}\mathbf{h}_k^{(e)} d\Omega\right], \tag{3-31d}$$

$$\mathbf{1} = \left[1,\ 1,\ \cdots,\ 1\right]^T, \tag{3-31e}$$

where $\mathbf{h}_k^{(e)}$ is the 1D interpolation matrix $\mathbf{h}^{(e)}$ at cross-sectional plane k, M_x is an torsional moment acting on the beam, and $\mathbf{C}_k^{(e)}$ is defined as

$$\mathbf{C}_k^{(e)} = \left[\int_{\Omega^{(e)}} G^{(e)}\left(y\frac{\partial \mathbf{H}_k^{(e)T}}{\partial z} - z\frac{\partial \mathbf{H}_k^{(e)T}}{\partial y}\right) d\Omega\right]. \tag{3-31f}$$

Eqs. (3-26)-(3-31) can be merged into the following matrix equation

$$
\begin{bmatrix} \mathbf{K}_w & -\mathbf{N}_z & \mathbf{N}_y & \mathbf{B}_c \\ \mathbf{Q}_x & \mathbf{0} & \mathbf{0} & \mathbf{0} \\ \mathbf{Q}_y & \mathbf{0} & \mathbf{0} & \mathbf{0} \\ \mathbf{Q}_z & \mathbf{0} & \mathbf{0} & \mathbf{0} \\ \mathbf{R}_w & -\mathbf{S}_y & -\mathbf{S}_z & \mathbf{J}_x \end{bmatrix} \begin{bmatrix} \mathbf{U} \\ \tilde{\Lambda}_y \\ \tilde{\Lambda}_z \\ \mathbf{A} \end{bmatrix} = M_x \begin{bmatrix} \mathbf{0} \\ \mathbf{0} \\ \mathbf{0} \\ \mathbf{0} \\ \mathbf{1} \end{bmatrix}. \tag{3-32}
$$

Solving Eq. (3-32), the interface warping function, the corresponding twisting center, and the twist rate can be simultaneously calculated along with the fully coupled effects of adjacent elements. Since the magnitude of M_x is proportional to the twist rate and does not affect the warping function and twisting center, an arbitrary number can be applied to M_x. Note that, when Eq. (3-32) is applied to continuous cross-section beams with uniform material, the free warping function with constant twist rate and twisting center is obtained.

We tested the proposed finite element discretization to calculate the interface warping function considering beams with geometric and material discontinuities. Almost the same interface warping functions were calculated irrespective of beam length and number of elements used along the longitudinal direction. Therefore, the use of only two elements along the longitudinal direction is recommended. For example, considering the beam in **Fig. 3-1**, one element is used for cross-section ① and another element is used for cross-section ②.

3.4 Convergence Test

In this section, we perform a convergence test for the proposed interface warping calculation. The interface warping function and its twisting center will be observed based on the number of elements used along the longitudinal direction.

To assess the beam with geometric and material discontinuity, a step-varying thick beam with geometric discontinuity [25] and a partially reinforced thin beam with material discontinuity will be observed. Both beams are subjected to a torsional moment, and the calculated interface warping functions are normalized for comparison.

Fig. 3-4(a) illustrates a step varying rectangular cross-section problem with two beam parts. Cross-sections of each beam part, ① and ②, have heights of $0.5\,\mathrm{m}$ and $1\,\mathrm{m}$, respectively, and identical width of $0.5\,\mathrm{m}$. The beam is composed of a material with Young's modulus $E = 2\times10^{11}\,\mathrm{Pa}$ and Poisson's ratio $\nu = 0$. Two and one 16-node cubic cross-sectional elements are used to discretize ① and ②, respectively.

Fig. 3-4(b) shows a partially reinforced wide flange beam with material discontinuity. Half of the beam has a reinforced upper flange Ω_r (shaded in gray) with Young's modulus $E_r = 6\times10^{11}$ Pa and Poisson's ratio $\nu = 0$. The remaining part of the beam is made of a material with Young's modulus $E_0 = 2\times10^{11}$ Pa and Poisson's ratio $\nu = 0$. The cross-sections are discretized with 7 16-node cubic cross-sectional elements.

The beam domain Ω will be split into N parts along the longitudinal direction with $N = 2$, 4, 8, and 16. **Fig. 3-4(c)** demonstrates the mesh with $N = 4$ and $N = 8$ for comparison. The longitudinal length of the beam domain Ω is assumed to be infinite, and a linear shape function is used to interpolate along the longitudinal direction.

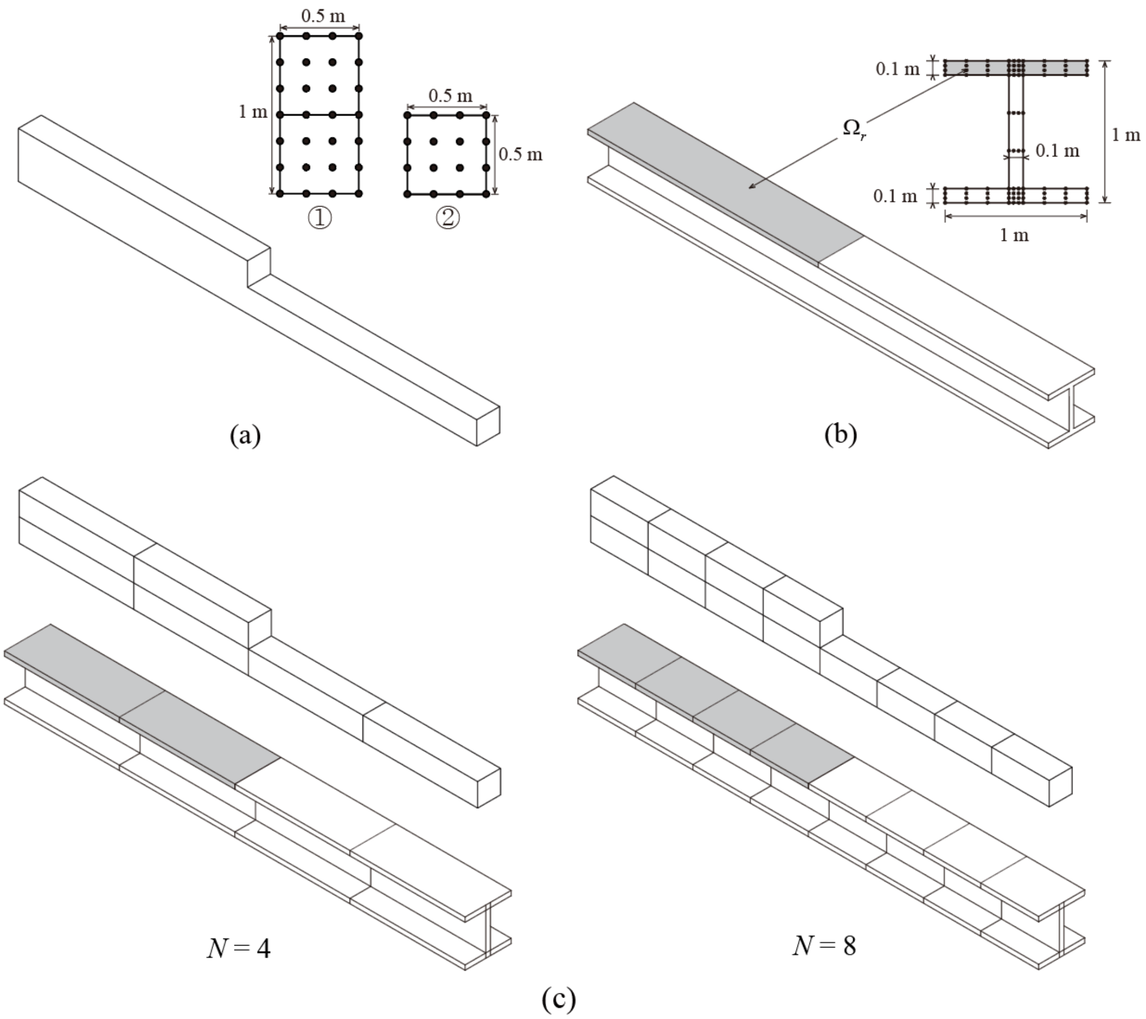

Figure 3-4. Description of convergence test. (a) Step varying rectangular cross-section beam problem and its cross-sectional discretization. (b) Partially reinforced wide flange beam problem and its cross-sectional discretization. (c) Mesh with $N = 4$ and $N = 8$.

The calculated nodal interface warping functions and twist centers are compared with the result obtained using a mesh of $N = 64$. The calculated nodal interface warping functions are normalized and then compared using the relative error norm,

$$E = \frac{\left\| \mathbf{F}_{ref} - \mathbf{F}_h \right\|_2}{\left\| \mathbf{F}_{ref} \right\|_2}, \tag{3-33}$$

where $\mathbf{F}$ is the vector containing the nodal interface warping function values f_i, and "ref" and "h" denote the reference and the finite element solutions, respectively. The relative error of the position of the twist center is measured in the same way.

Table 3-1 gives the relative error of the nodal interface warping function and the position of the twist center. It can be seen that the calculated values from the mesh of $N = 2$ give the same solution compare to that from the mesh of $N = 64$.

Table 3-1. Relative error of the nodal interface warping function and the position of twist center.

N	Step-varying rectangular cross-section beam		Partially reinforced wide flange beam	
	Nodal interface warping function	Position of twist center	Nodal interface warping function	Position of twist center
2	6.11715×10^{-9}	3.81028×10^{-9}	4.16073×10^{-14}	7.11663×10^{-14}
4	4.09772×10^{-10}	2.55237×10^{-10}	2.34144×10^{-14}	2.01117×10^{-14}
8	2.10534×10^{-12}	1.30599×10^{-12}	2.41485×10^{-14}	5.84202×10^{-14}
16	1.50455×10^{-14}	2.23571×10^{-15}	2.74817×10^{-14}	1.26663×10^{-14}

3.5 Numerical Examples

In this section, we present four numerical examples to verify the usefulness of the proposed interface warping function: a partially reinforced wide flange beam, a partially constrained warping problem, a step varying rectangular cross-section beam, and a circular beam with a step varying rectangular cross-section.

In the following examples, the beams are modeled using 2-node continuum-mechanics based beam elements, and their cross-sections are discretized using 4-node or 16-node quadrilateral cross-sectional elements. The well-known reduced integration scheme is applied along the longitudinal direction of the beam element to avoid shear locking [28,29], and 2×2 or 4×4 Gauss integration points are used on 4-node or 16-node cross-sectional elements, respectively. The interface warping functions are calculated using Eq. (3-32) in the straight beam domain Ω in **Fig. 3-3(a)**, where its cross-sectional mesh used is the same as that of continuum-mechanics based beam elements.

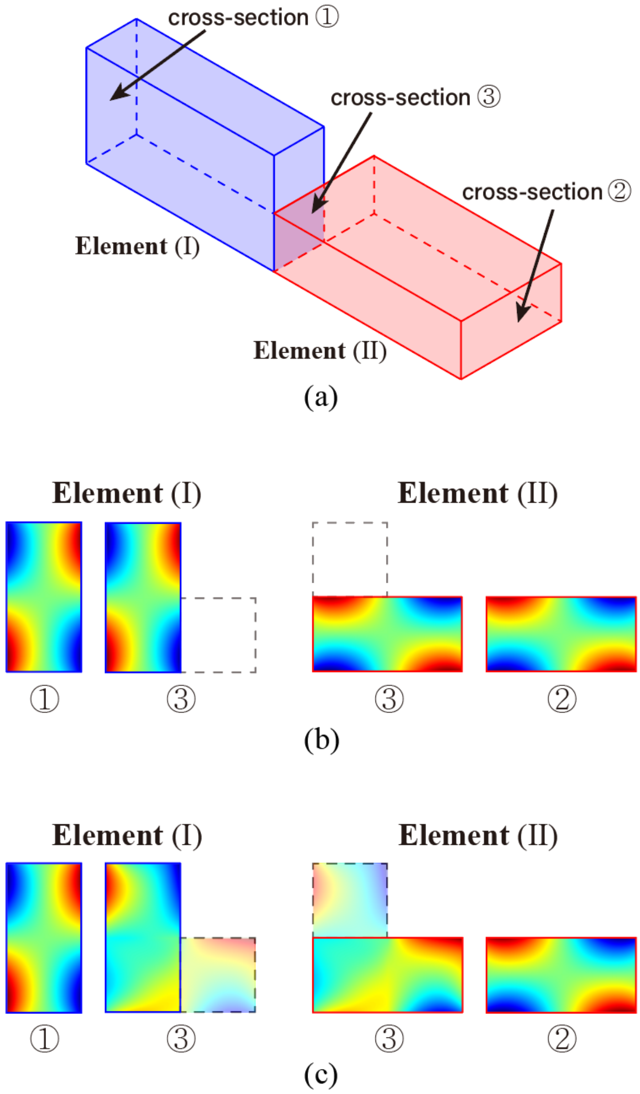

Figure 3-5. Comparison of the free warping beam model and the proposed warping beam model: (a) Beam with longitudinal discontinuity and its cross-sections. (b) Free warping beam model constructed using free warping functions. (c) Proposed warping beam model constructed using the interface warping function.

Fig. 3-5 compares two different methods of modeling beams with longitudinal discontinuity. **Fig. 3-5(a)** illustrates two beam elements, (I) and (II), with three different cross-sections: ①, ②, and ③. **Fig. 3-5(b)** shows the free warping beam model, in which free warping functions of each cross-section are applied to each node. In this model, the compatibility of warping displacements is not satisfied at the interface cross-section ③. This incompatibility can be resolved with the proposed warping beam model by applying the interface warping function to cross-section ③, as shown in **Fig. 3-5(c)**. As a result, the adjacent elements of the interface cross-section share the same warping shape and magnitude; therefore, the displacement compatibility is always satisfied.

The numerical results are compared with the reference solutions obtained using 20-node hexahedral solid elements in ANSYS [30]. To assess the performance of the proposed warping beam model, the calculated values using the free warping beam model, BEAM188 in ANSYS, and results from Ref. [25] are compared. While BEAM188, the free warping beam model, and the proposed warping beam model employ 7 DOFs per node, 7 to 9 DOFs per node are used in the beam model by Yoon and Lee [25].

3.5.1 Partially reinforced wide flange beam

Here, we consider a partially reinforced wide flange beam of length $10\,\mathrm{m}$ with material discontinuity. As shown in **Fig. 3-6(a)**, the height and width of the cross-section are 1m, and the thickness is 0.1m. Half of the beam has a reinforced upper flange Ω_r (colored in gray) with Young's modulus $E_r = 6\times10^{11}\,\mathrm{Pa}$ and Poisson's ratio $\nu = 0$, as illustrated in **Fig. 3-6(a)**. In the remaining part, Young's modulus is $E_0 = 2\times10^{11}\,\mathrm{Pa}$ and Poisson's ratio is $\nu = 0$. The beam is fully clamped at $x = 0\,\mathrm{m}$ and the torsional moment M_x is applied at $x = 10\,\mathrm{m}$.

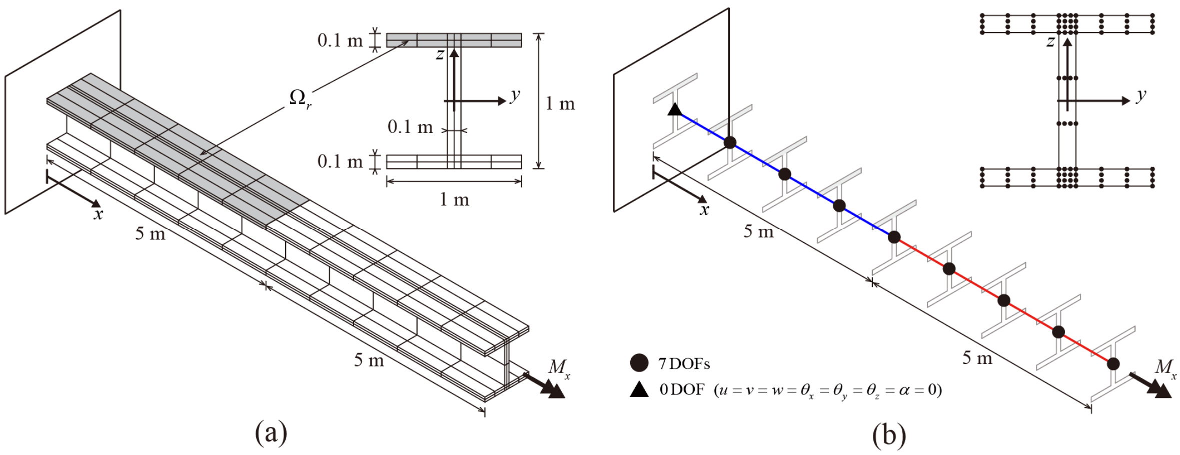

Figure 3-6. Partially reinforced wide flange beam. (a) Reference solid model. (b) Beam model and its cross-sectional mesh.

To obtain the reference solutions, the solid model is constructed using 280 hexahedral solid elements (5,223 DOFs), as illustrated in **Fig. 3-6(a)**. All DOFs are fixed at the clamped end surface ($x = 0\,\mathrm{m}$), and the torsional moment M_x is applied at the free end surface ($x = 10\,\mathrm{m}$). Three beam models are constructed using eight 2-node beam elements ($7\times9 = 63$ DOFs) for comparison: an ANSYS beam model using BEAM188, a free warping beam model, and the proposed warping beam model. The fully clamped boundary condition ($u = v = w = \theta_x = \theta_y = \theta_z = \alpha = 0$) is applied at $x = 0\,\mathrm{m}$, as shown in **Fig. 3-6(b)**. The cross-section of the

ANSYS BEAM188 is discretized with twenty-eight 9-node quadratic cross-sectional elements, and the proposed warping beam model is discretized with seven 16-node cubic cross-sectional elements.

Fig. 3-7 illustrates the distribution of the calculated warping displacements and positions of the twisting centers at $x = 2.5\,\mathrm{m}$, $x = 5.0\,\mathrm{m}$, and $x = 7.5\,\mathrm{m}$ when $M_x = 1\mathrm{Nm}$ is applied. The shape of free warping displacements and the corresponding positions of twisting centers at $x = 2.5\,\mathrm{m}$ and $x = 7.5\,\mathrm{m}$ are identical to those from the classical Saint-Venant torsion theory. However, the interface warping function at $x = 5.0\,\mathrm{m}$ can only be obtained through Eq. (3-32). The variation of the twisting center along the *x*-direction is automatically considered through the displacement field in Eq. (3-33).

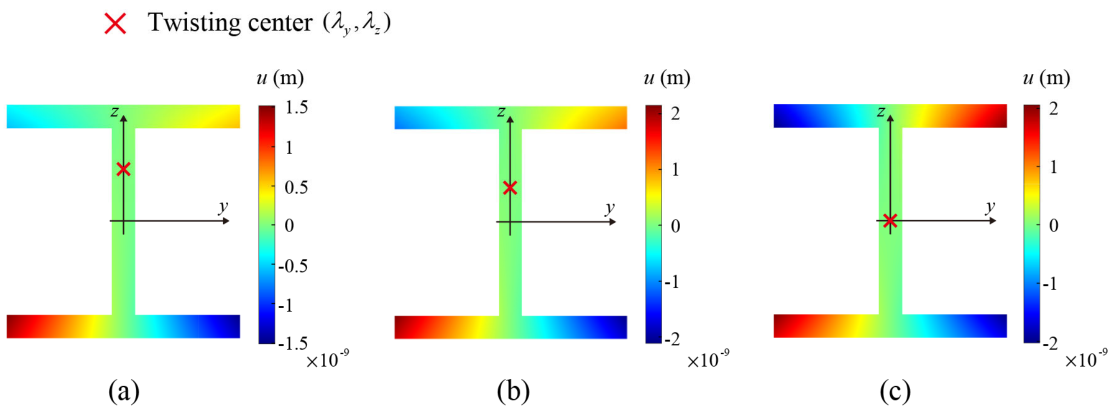

Figure 3-7. Distributions of the warping displacements u and twisting centers (λ_y, λ_z) for the partially reinforced wide flange beam. The location of twisting centers is indicated by a red cross. (a) Free warping displacement and twisting center $(\lambda_y, \lambda_z) = (0, 0.2234)$ at $x = 2.5\,\mathrm{m}$. (b) Interface warping displacement and twisting center $(\lambda_y, \lambda_z) = (0, 0.1487)$ at $x = 5.0\,\mathrm{m}$. (c) Free warping displacement and twisting center $(\lambda_y, \lambda_z) = (0, 0)$ at $x = 7.5\,\mathrm{m}$.

Fig. 3-8 compares three numerical results of the linear analysis along the beam length when $M_x = 1\mathrm{Nm}$ is applied: the distribution of twist angle θ_x and *y*-directional displacements v of points A and B, respectively. The proposed warping beam model shows good agreement with the reference model, while the free warping beam model fails to predict the behavior of the beam after the interface ($x = 5\,\mathrm{m}$). ANSYS BEAM188 gives a twist angle that exhibits good agreement with the reference solution, but displacements corresponding to points A and B do not match with the reference solutions.

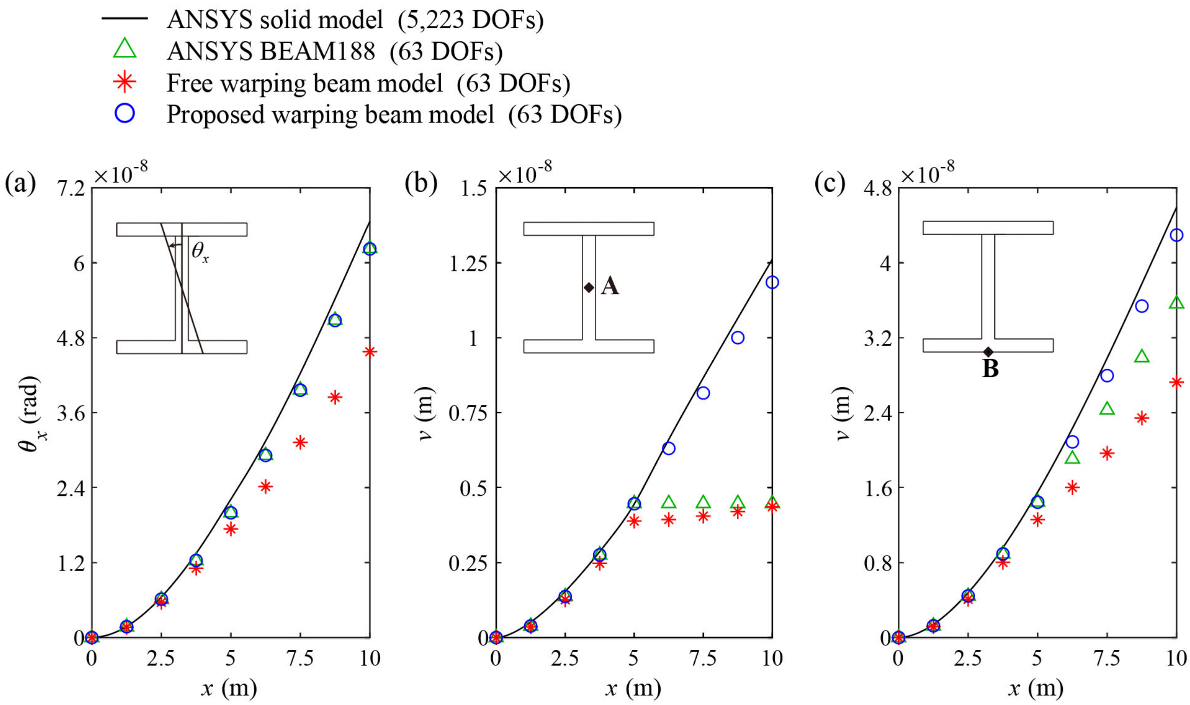

Figure 3-8. Linear analysis results for the partially reinforced wide flange beam. (a) Twist angle θ_x, (b) displacement v of point A, and (c) displacement v of point B along the beam.

For geometric nonlinear analysis, the torsional moment M_x increases up to $8\times10^6\,\text{Nm}$. **Fig. 3-9** displays the load-displacement curves, where the displacements of point A at the free tip is considered. This shows the proposed warping beam model can accurately predict the deformation due to the twisting-bending coupling unlike ANSYS BEAM188. **Fig. 3-10** illustrates the displacement distributions when the torsional moment of $M_x = 8\times10^6\,\text{Nm}$ is applied at the free tip. This shows that the proposed warping beam model can accurately predict not only the y-directional displacement v of point A, but also the z-directional displacement w of point A.

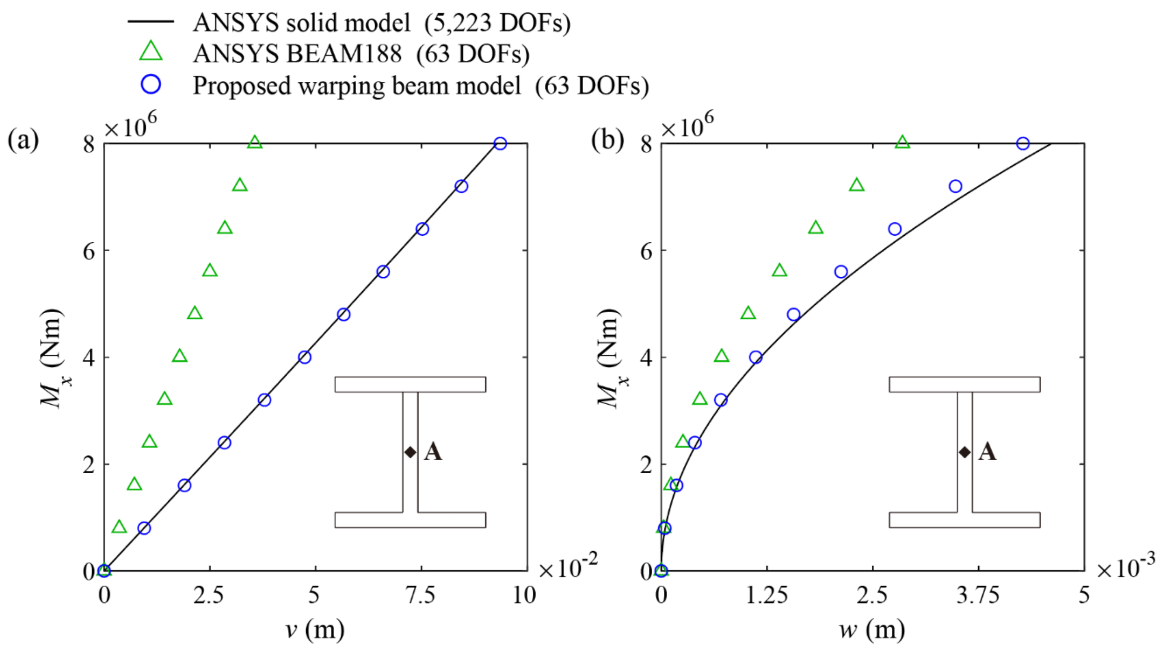

Figure 3-9. Load-displacement curves for the partially reinforced wide flange beam. (a) Displacement v, and (b) displacement w of point A at the free tip.

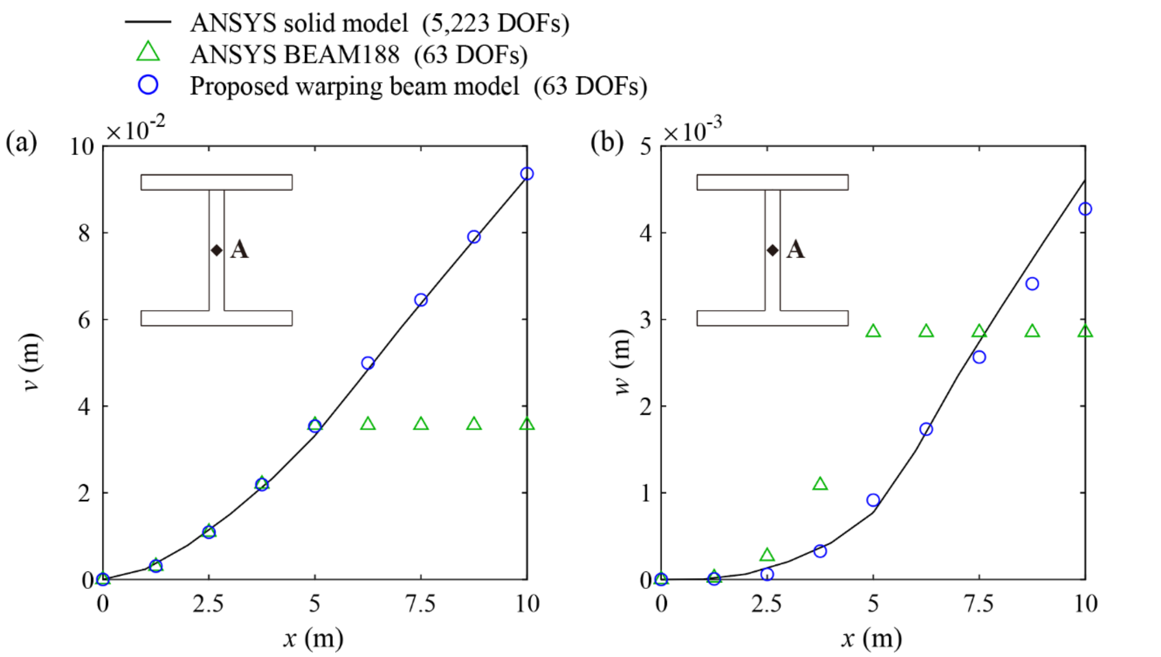

Figure 3-10. Nonlinear analysis results for the partially reinforced wide flange beam. (a) Twist angle θ_x, (b) displacement v of point A, and (c) displacement v of point B along the beam.

3.5.2 Partially constrained warping problem

In this section, we consider the wide flange beam proposed in Ref. [25]. The geometry of the beam is equal to that used in the previous example. In this problem, two boundary conditions are considered: a partially constrained boundary condition and a fully constrained boundary condition. In the boundary cross-section at $x = 0\,\mathrm{m}$, all displacements, including warping, are constrained only at the shaded area in **Fig. 3-11(a)**, and a torsional moment M_x is applied at the free end ($x = 10\,\mathrm{m}$). Young's modulus is $E = 2\times10^{11}$ Pa and Poisson's ratio is $\nu = 0$.

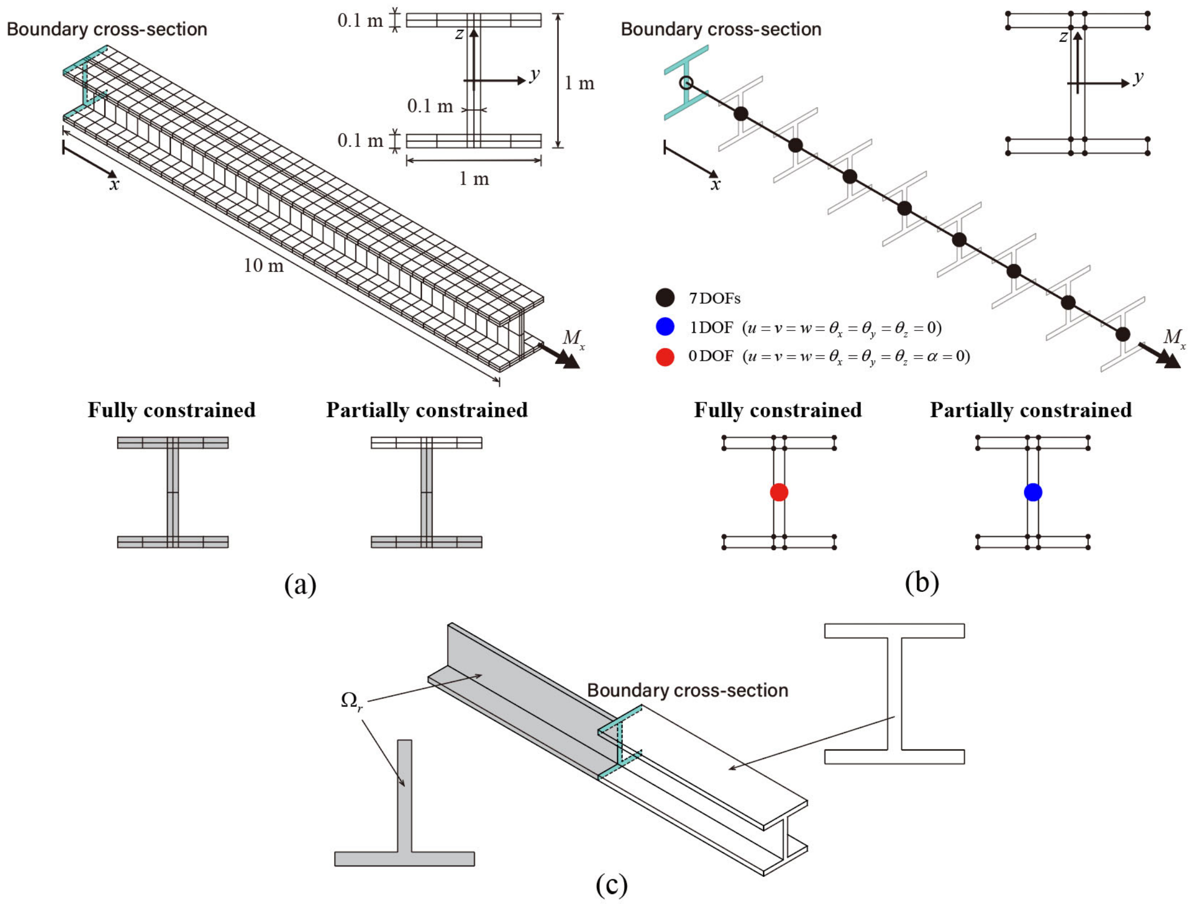

Figure 3-11. Partially constrained warping problem. (a) Reference solid model: shaded areas in the boundary cross-section are constrained. (b) Beam model and its cross-sectional mesh: warping DOF is imposed to the boundary cross-section for the partially constrained boundary condition. (c) Model used to calculate the interface warping function by attaching a rigid beam

The reference solid model uses 1,120 hexahedral solid elements (19,803 DOFs), as illustrated in **Fig. 3-11(a)**. All nodes corresponding to the shaded area ($x = 0\,\mathrm{m}$) are fixed. **Fig. 3-11(b)** shows a beam model consisting of eight 2-node beam elements; its cross-section consists of seven 4-node cross-sectional elements. All DOFs at $x = 0\,\mathrm{m}$ are fully clamped ($u = v = w = \theta_x = \theta_y = \theta_z = \alpha = 0$) for the fully constrained condition, while the partially constrained boundary condition has warping DOF ($u = v = w = \theta_x = \theta_y = \theta_z = 0$), as illustrated in **Fig. 3-11(b)**. Note that Yoon and Lee [25] used 8 DOFs per node ($8 \times 9 = 72$ DOFs) to solve this beam problem, while the proposed warping beam model uses 7 DOFs per node ($7 \times 9 = 63$ DOFs).

The interface warping function is employed to model the partially constrained boundary condition. **Fig. 3-11(c)** shows the model used to calculate the interface warping function by attaching a rigid beam (colored in gray, Ω_r) to the boundary cross-section. The rigid beam is modeled with a higher Young's modulus $E_r = 2 \times 10^{18}$ Pa and Poisson's ratio $\nu = 0$. Note that the model in **Fig. 3-11(c)** is only adopted to calculate the interface warping function using Eq. (3-32).

Fig. 3-12 demonstrates the distribution of the calculated warping displacements and positions of the twisting centers at $x = 0.0\,\mathrm{m}$ and $x = 5.0\,\mathrm{m}$ when $M_x = 1\,\mathrm{Nm}$ is applied. The warping displacement at $x = 5.0\,\mathrm{m}$ shows the free warping function, and its twisting center is located on $y = z = 0.0\,\mathrm{m}$ due to symmetry. The shape of the warping displacement observed at $x = 0.0\,\mathrm{m}$ is similar to that of the free warping function except for the constrained region (shaded area in **Fig. 3-11(a)**), but the location of the twisting center is significantly different.

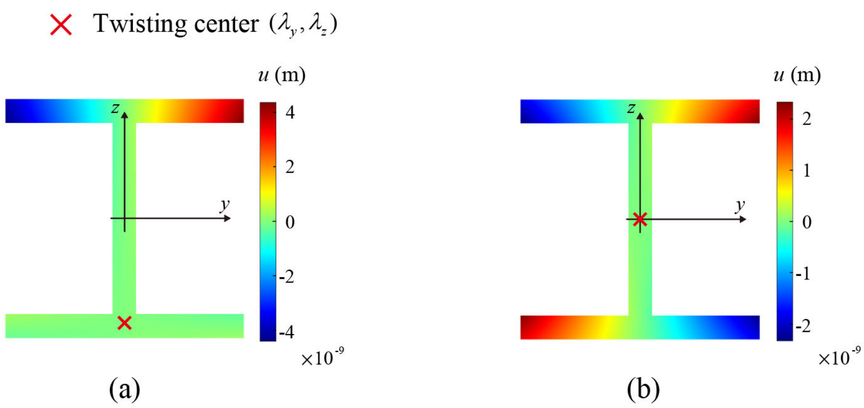

Figure 3-12. Distributions of the warping displacements u and twisting centers (λ_y, λ_z) for the partially constrained warping problem. The location of twisting centers is indicated by a red cross. (a) Interface warping displacement and twisting center $(\lambda_y, \lambda_z) = (0, -0.4369)$ at $x = 0.0\,\mathrm{m}$. (b) Free warping displacement and twisting center $(\lambda_y, \lambda_z) = (0, 0)$ at $x = 5.0\,\mathrm{m}$.

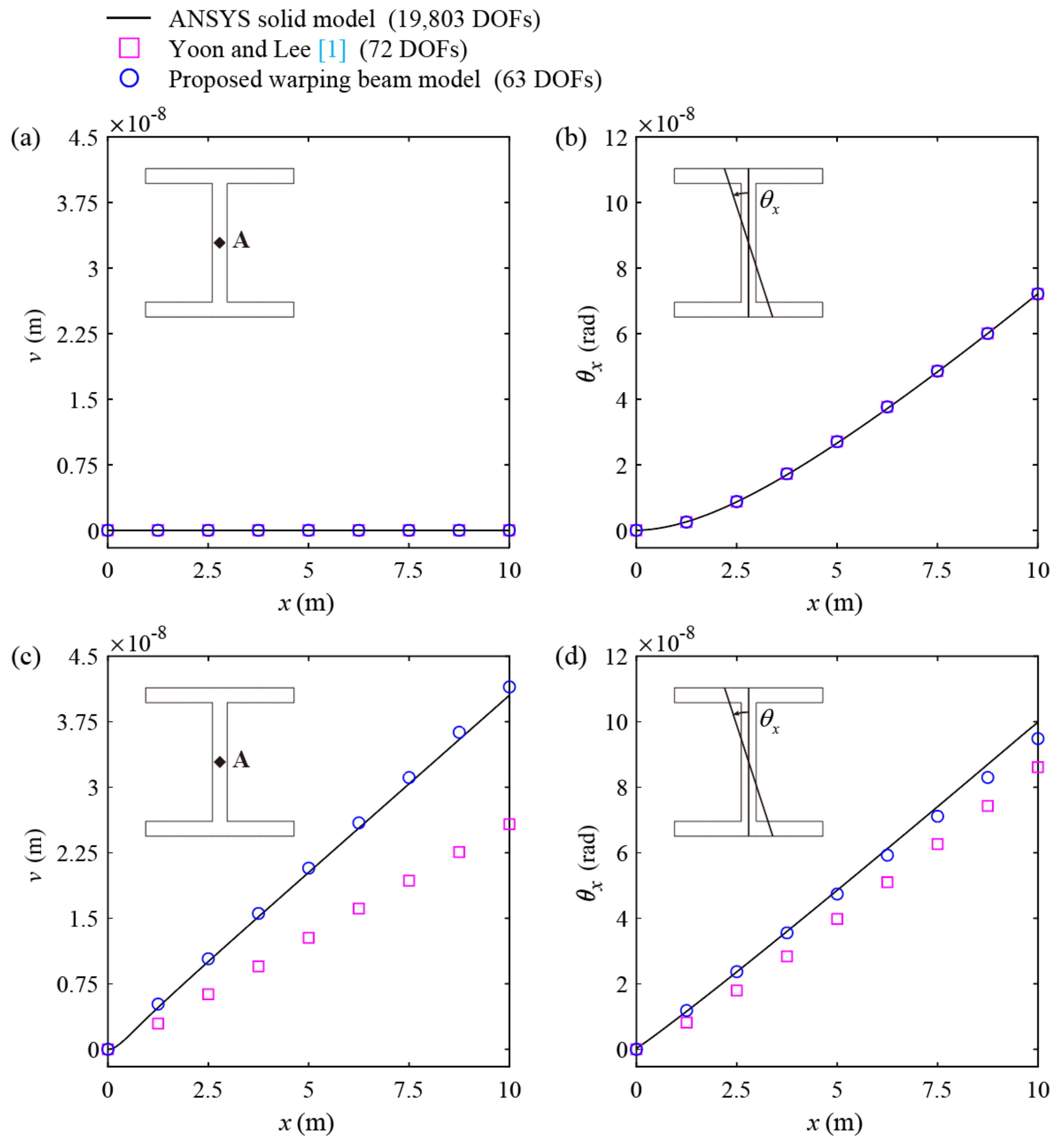

Figure 3-13. Linear analysis results for the partially constrained warping problem in fully and partially constrained boundary conditions: (a) Displacement v of point A, and (b) twist angle θ_x along the beam in the fully constrained boundary condition. (c) Displacement v of point A, and (d) twist angle θ_x along the beam in the partially constrained boundary condition.

Fig. 3-13 shows the numerical results of the linear analysis when $M_x = 1\,\text{Nm}$ is applied at the free tip. In the fully constrained boundary condition, both results from Ref. [25] and the proposed warping beam model match considerably well with the reference solution. However, in the partially constrained boundary condition, even though the proposed warping beam model used fewer DOFs per node, it shows better results compared with those in Ref. [25]. Note that the classical Saint-Venant torsion theory cannot be applied to solve the partially constrained warping problems.

3.5.3 Step varying rectangular cross-section beam

Fig. 3-14(a) shows the step varying rectangular cross-section beam [25] with two parts. Cross-sections of each beam part, ① and ②, have heights of $0.5\,\mathrm{m}$ and $1\,\mathrm{m}$, respectively, and an identical width of $0.5\,\mathrm{m}$. Young's modulus is $E = 2\times10^{11}\,\mathrm{Pa}$ and Poisson's ratio is $\nu = 0$. A fully clamped boundary condition is imposed at $x = 0\,\mathrm{m}$ while torsional moment M_x is applied at $x = 10\,\mathrm{m}$.

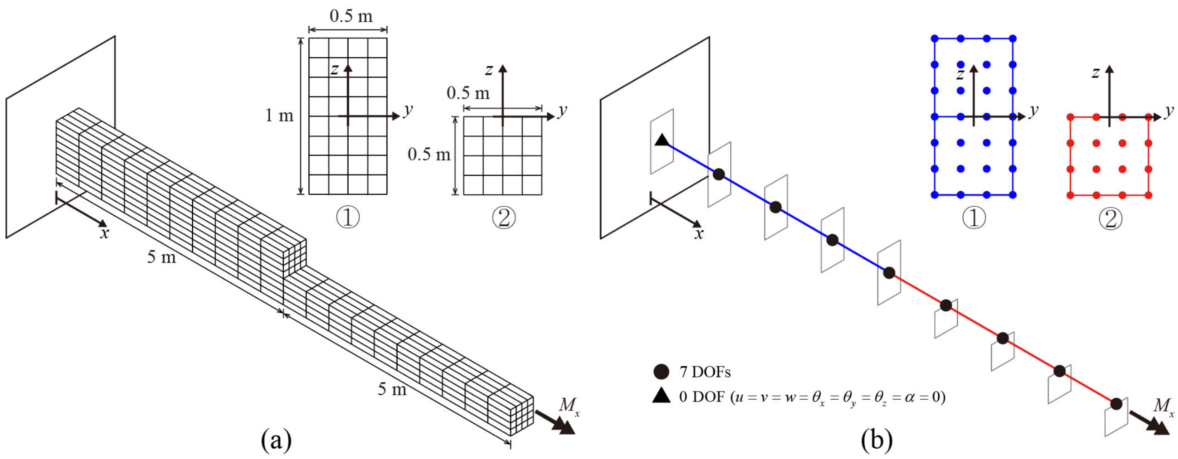

Figure 3-14. Step varying rectangular cross-section beam. (a) Reference solid model. (b) Beam model and its cross-sectional meshes.

As illustrated in **Fig. 3-14(a)**, the reference solid model is constructed using 480 hexahedral solid elements (8,055 DOFs). All DOFs are fixed at the clamped end surface ($x = 0\,\mathrm{m}$), and the torsional moment M_x is applied at the free end surface ($x = 10\,\mathrm{m}$). **Fig. 3-14(b)** shows that the beam models consist of eight 2-node beam elements, with cross-sections ① and ② (blue and red colored, respectively). 7 DOFs per node are used to construct the proposed warping beam and ANSYS BEAM188 models ($7\times9 = 63$ DOFs), but Yoon and Lee [25] used 7 and 8 DOFs per node to express the warping effect at the interface and continuous cross-sections, respectively (71 DOFs).

The proposed warping beam model used two and one 16-node cross-sectional elements to discretize cross-sections ① and ②, respectively, as in Ref. [25]. The cross-sections of the ANSYS BEAM188 model are discretized using finer meshes with eight and four 9-node quadratic cross-sectional elements, respectively. A fully constrained boundary condition ($u = v = w = \theta_x = \theta_y = \theta_z = \alpha = 0$) at $x = 0\,\mathrm{m}$ is applied and torsional moment M_x is applied at the free end.

Fig. 3-15 illustrates the calculated warping displacements and positions of twisting centers at $x = 2.5\,\mathrm{m}$, $x = 5.0\,\mathrm{m}$, and $x = 7.5\,\mathrm{m}$ of the proposed warping beam model, when $M_x = 1\mathrm{Nm}$ is applied. **Fig. 3-16** presents the linear analysis results along the beam length when $M_x = 1\mathrm{Nm}$ is applied. It can be seen that the proposed warping beam model is the most reliable for analyzing the beam with discontinuity. We also confirm that the proposed warping beam model used fewer DOFs to express the warping effect but showed better accuracy compared to the results in Ref. [25]. The free warping beam model failed to predict the behavior of the beam after the interface cross-section.

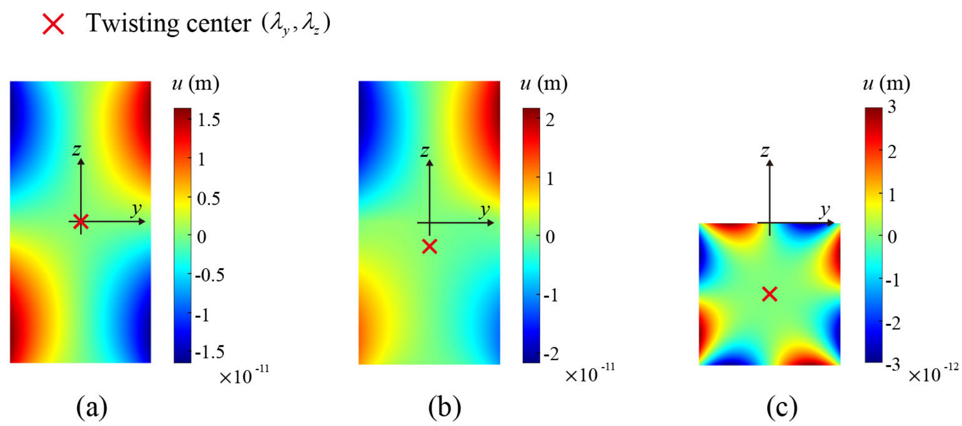

Figure 3-15. Distributions of the warping displacements u and twisting centers (λ_y, λ_z) for the step varying rectangular cross-section beam. The location of twisting centers is indicated by a red cross. (a) Free warping displacement and twisting center $(\lambda_y, \lambda_z) = (0, 0)$ at $x = 2.5\,\mathrm{m}$. (b) Interface warping displacement and twisting center $(\lambda_y, \lambda_z) = (0, -0.0833)$ at $x = 5.0\,\mathrm{m}$. (c) Free warping displacement and twisting center $(\lambda_y, \lambda_z) = (0, -0.25)$ at $x = 7.5\,\mathrm{m}$.

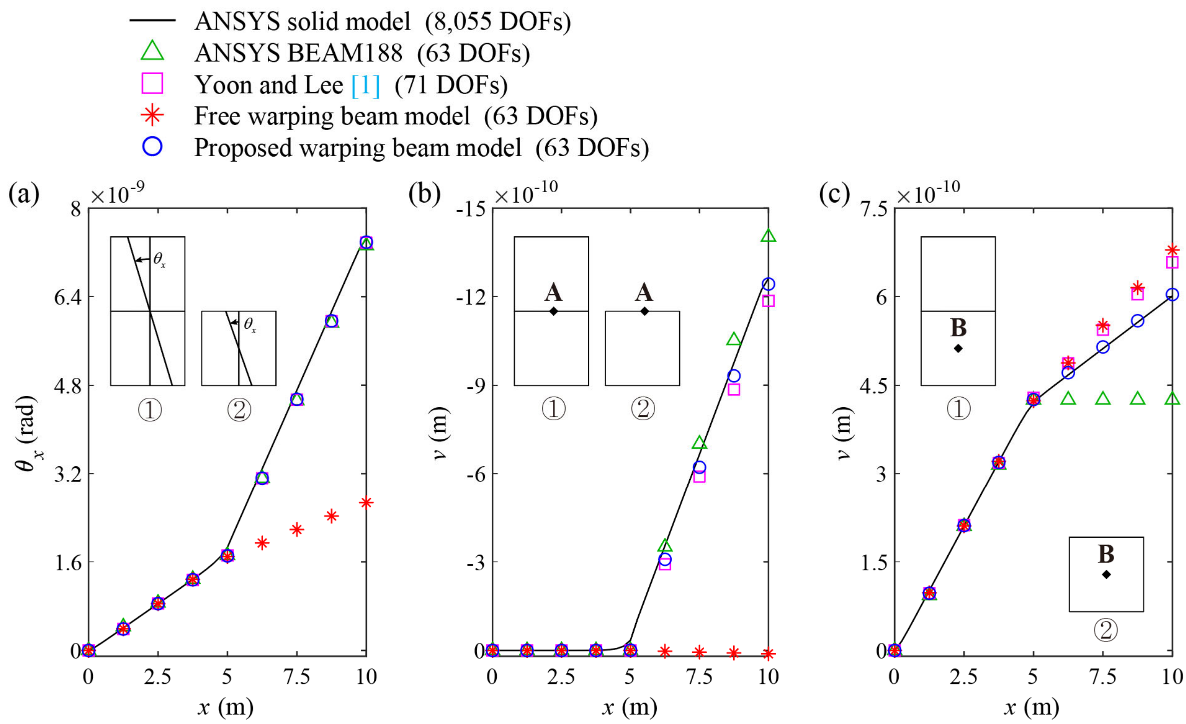

Figure 3-16. Linear analysis results for the step varying rectangular cross-section beam. (a) Twist angle θ_x, (b) displacement v of point A, and (c) displacement v of point B along the beam.

For geometric nonlinear analysis, we statically increase the torsional moment M_x up to $2\times10^8\,\text{Nm}$. **Fig. 3-17** displays the load-displacement curves, where the displacements of point A at the free tip are considered when $M_x = 2\times10^8\,\text{Nm}$ is applied. The results indicate that the proposed warping beam model predicts the geometric nonlinear behavior better than the ANSYS BEAM188. **Fig. 3-18** shows the displacements of point A along the beam length when $M_x = 2\times10^8\,\text{Nm}$ is applied. As seen, the proposed warping beam model successfully reflects the twisting-bending coupling effect compared with the ANSYS BEAM188 model.

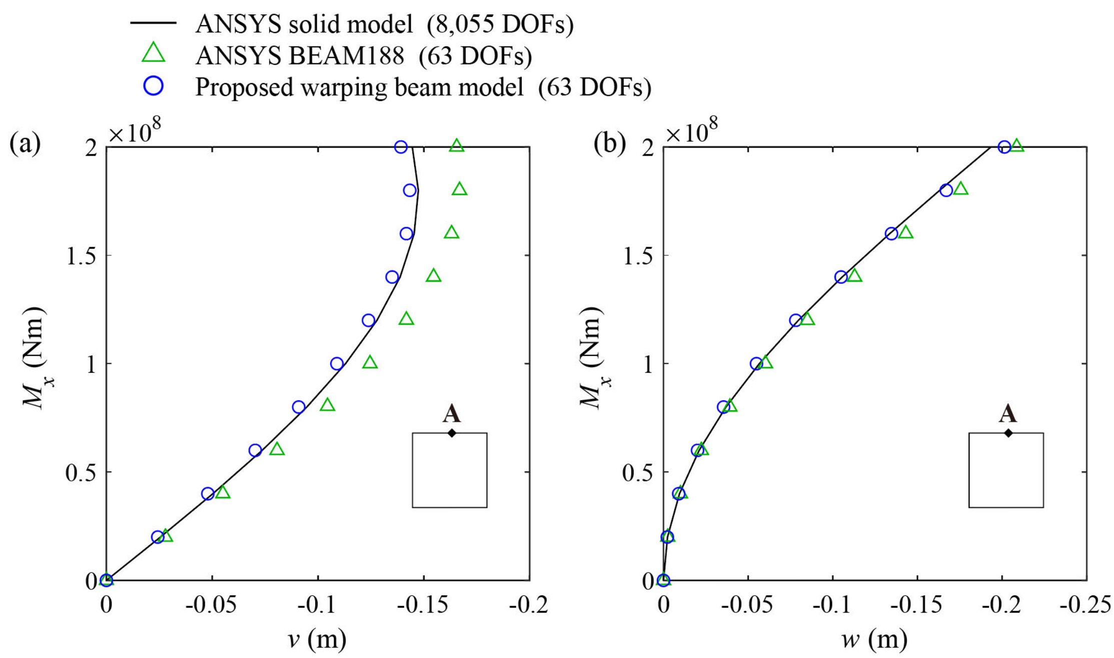

Figure 3-17. Load-displacement curves for the step varying rectangular cross-section beam. (a) Displacement v, and (b) displacement w of point A at the free tip.

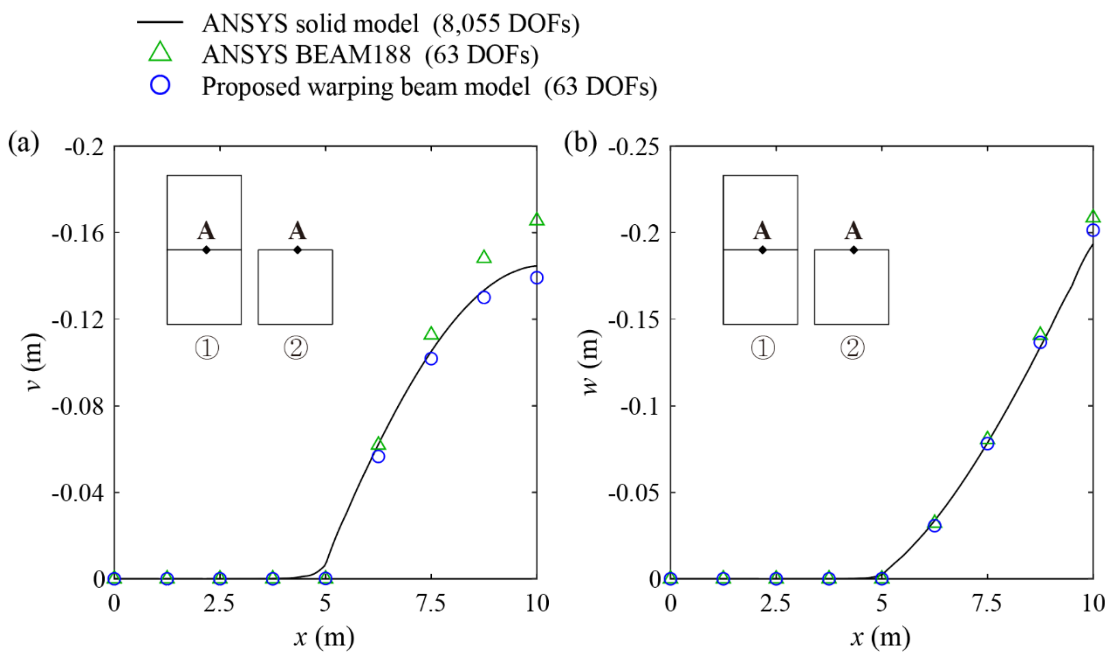

Figure 3-18. Nonlinear analysis results for the step varying rectangular cross-section beam. (a) Displacement v, and (c) displacement w of point A along the beam.

3.5.4 Circular beam with step varying rectangular cross-section

Finally, we consider the circular beam with a step varying rectangular cross-section, as shown in **Fig. 3-19**, to assess the twisting-bending behavior of the curved beam with longitudinal discontinuity. The beam has a radius of $10\mathrm{m}$ and its cross-section discontinuously varies from the rectangular cross-section ① to the square cross-section ② at $\phi = 180°$. The beam is fully clamped at $\phi = 0°$, and a force $F_z = 1.5\times10^6\,\mathrm{N}$ is applied at $\phi = 359°$. Young's modulus is $E = 2\times10^{11}\,\mathrm{Pa}$ and Poisson's ratio is $\nu = 0.3$. Geometric nonlinear analysis is performed, since the beam is expected to undergo large displacement and large rotation.

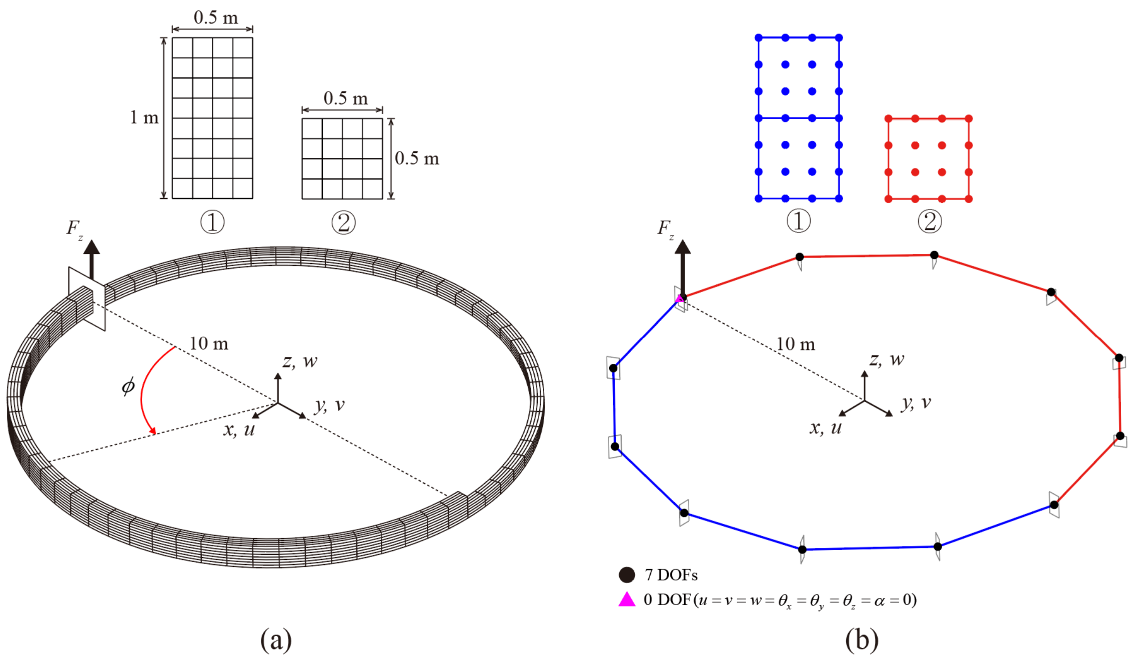

Figure 3-19. Circular beam with a step varying rectangular cross-section. (a) Reference solid model. (b) Beam model and its cross-sectional meshes.

The reference solid model is obtained using 1,472 hexahedral solid elements (23,943 DOFs), as shown in **Fig. 3-19(a)**. All DOFs are constrained at $\phi = 0°$, and the force $F_z = 1.5\times10^6\,\mathrm{N}$ is applied at the free end surface ($\phi = 359°$). **Fig. 3-19(b)** shows that the beam model consists of twelve 2-node beam elements ($7\times13 = 91$ DOFs), which are used to construct both proposed warping beam and ANSYS BEAM188 models. The cross-sections ① and ② are discretized using eight and four 9-node quadratic cross-sectional elements for the ANSYS BEAM188 model, respectively, and one and two 16-node cubic cross-sectional elements for the proposed warping beam model, respectively. The constrained boundary condition $u = v = w = \theta_x = \theta_y = \theta_z = \alpha = 0$ and force $F_z = 1.5\times10^6\,\mathrm{N}$ are applied at $\phi = 0°$ and $\phi = 359°$, respectively.

Fig. 3-20 shows the load-displacement curves considering the displacements of point A at the free end. The results from the proposed warping beam model correspond well with those from the reference solid model. **Fig. 3-21** presents the *y* and *z*-directional displacements (v and w) of point A according to the angle ϕ when $F_z = 1.5\times10^6\,\mathrm{N}$. These results confirm that the proposed interface warping function can be adopted to calculate complex beam problems considering twisting-bending coupling using only 7 DOFs per node. **Fig. 3-22** shows the successive deformed configurations obtained using the reference solid model and the proposed warping beam model at various load levels ($F_z = 0.3\times10^6\,\mathrm{N}$, $0.6\times10^6\,\mathrm{N}$, $0.9\times10^6\,\mathrm{N}$, $1.2\times10^6\,\mathrm{N}$, and $1.5\times10^6\,\mathrm{N}$). The geometric nonlinear response due to twisting-bending coupling is accurately predicted using the proposed warping beam model.

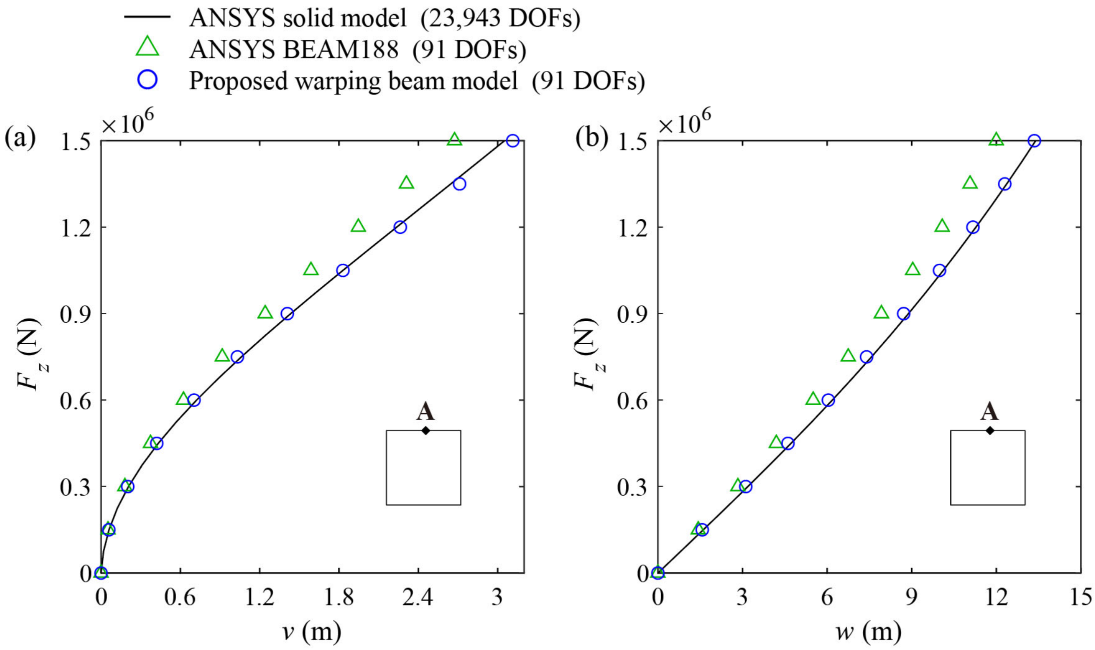

Figure 3-20. Load-displacement curves for the circular beam with a step varying rectangular cross-section. (a) Displacement *v*, and (b) displacement *w* of point A at the free tip.

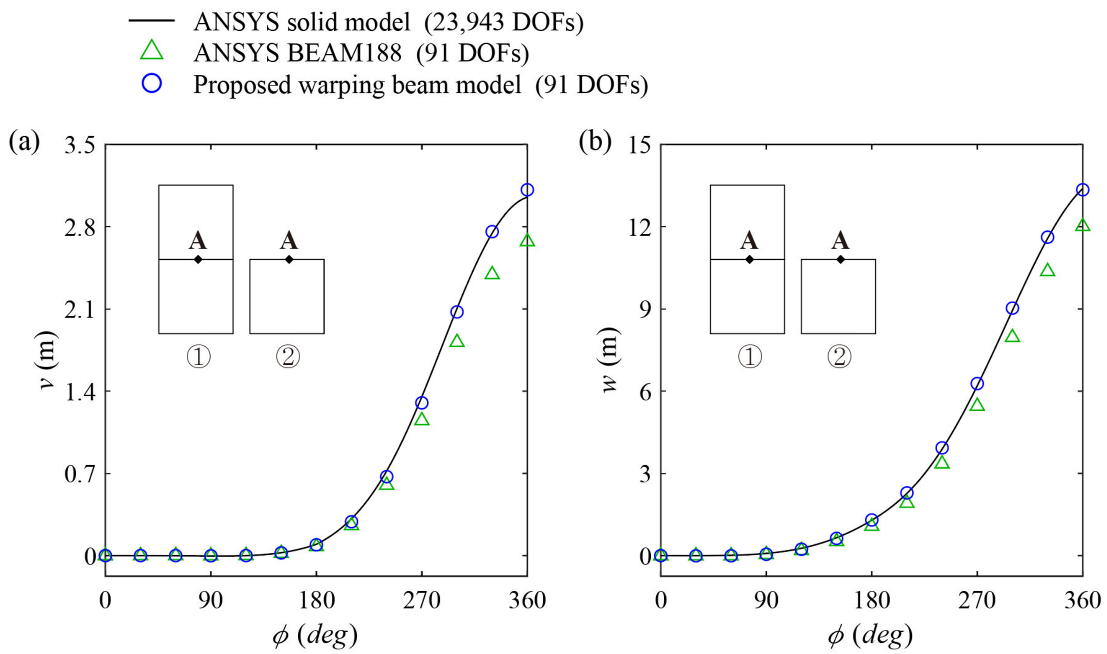

Figure 3-21. Nonlinear analysis results for the circular beam with a step varying rectangular cross-section. (a) Displacement v, and (c) displacement w of point A along the beam.

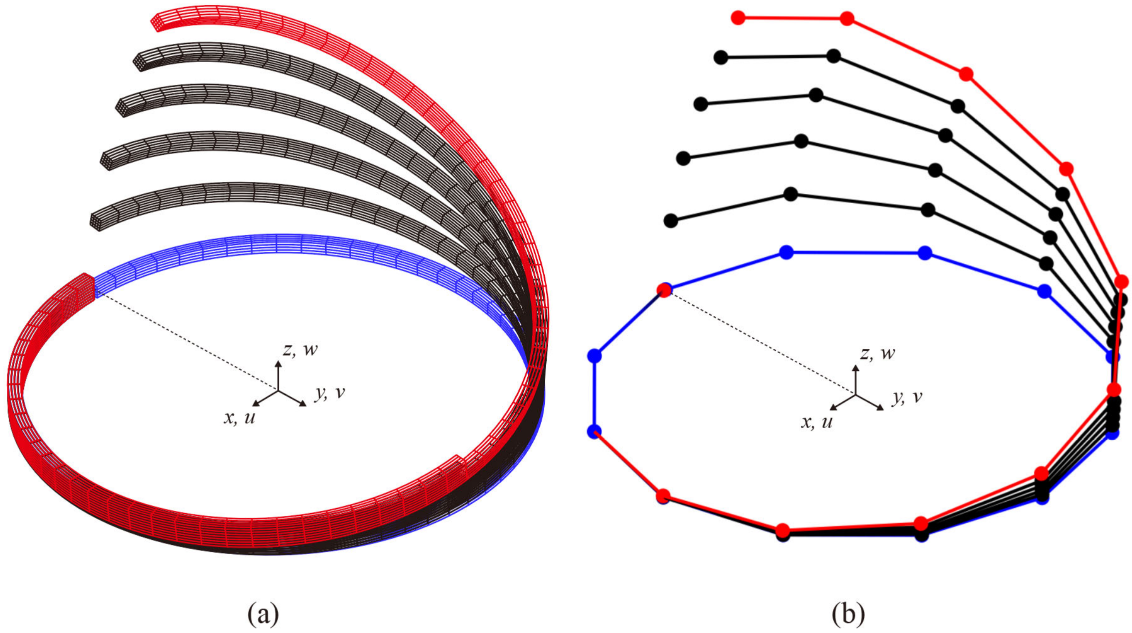

Figure 3-22. Deformed configurations of the circular beam with a step varying rectangular cross-section: (a) reference solid model, and (c) proposed warping beam model.

3.6 Concluding Remarks

In this chapter, we proposed a numerical method that can effectively calculate interface warping functions for beams with geometrical and material discontinuities in the longitudinal direction. The governing equations were obtained by extending the classical Saint-Venant torsion theory along the longitudinal direction. Finite element discretization was developed to numerically calculate the proposed interface warping functions and the corresponding twisting centers. The interface warping functions are incorporated with the continuum-mechanics based beam element. Consequently, a general 3D beam finite element capable of modeling longitudinal discontinuities was developed for linear and nonlinear analysis while using only 7 DOFs per node.

The proposed beam finite element can consider partially/fully constrained warping conditions, curved geometries, composite materials, longitudinal discontinuities in material and geometry, and arbitrary cross-sections. Through numerical examples, powerful modeling and predictive capabilities of the proposed warping beam model were demonstrated in both linear and geometric nonlinear analysis. An important advantage of the interface warping functions presented in this study is that the displacement compatibility at an interface cross-section can be satisfied using only 7 DOFs per node. The interface warping functions can be easily adopted to other types of beam finite elements, allowing consideration of material and geometric longitudinal discontinuities.

Chapter 4. Optimization of Beam using Interface Warping Mode

4.1 Optimization Problem

Thin-walled beams of the closed cross-section are widely used in engineering since they have a high stiffness ratio compared to their mass. Although both closed cross-section beams and open cross-section beams have high stiffness in bending and tension compared to their mass, open cross-section beams generally have lower torsional stiffness due to cross-section distortion. Therefore, closed-section beams are widely used in engineering practice to reduce mass.

Designing a cross-section of beam element to maximize its stiffness with respect to a given force condition was a popular beam optimization problem. Early studies attempted to change design parameters related to cross-sectional geometry. However, those studies could not express the change of topology, which is vital in the structural properties of the beam since a closed cross-section beam can endure more cross-sectional distortion mode and stiffeners influence its buckling mode.

One of the well-known optimization problems is to maximize the stiffness of structure within a given material constraint. In structural optimization problems, external force conditions and boundary conditions are given within its design space. The problem can be re-stated as: find the best shape of structure within design space to endure given external forces with the given boundary conditions.

Beam structures are long, and their global behaviors are categorized into: compression/extension, bending, shearing, and twisting. Shearing always provokes bending, and in most cases stress-induced by bending is much bigger than shear-induced stress. Optimal cross-sectional shape resulting in maximum bending stiffness is straightforward since bending is indeed simple deformation. A lot of studies related to beam cross-sectional optimization focused on maximizing torsional stiffness.

Three strategies can be applied to maximize torsional stiffness. First one is to maximize the moment of area. To do this, the material must be placed as far as possible from the twisting center within the design space. As a result, thin-walled beams with their shape with respect to design space are obtained. The second strategy is to make a cross-section into a closed section. It is a rational choice since open section beams are vulnerable to distortion, resulting in lower torsional rigidity. The last strategy is to eliminate the warping of beam, since the warping of beam always reduces the torsional rigidity. The detailed proof is stated in appendix A.

Designing a cross-section of beam element in order to maximize its stiffness with respect to a given force condition was one of the beam optimization problems. Early studies attempted to change design parameters related to cross-sectional geometry. However, those studies could not express the change of topology, which is vital in the structural properties of the beam since a closed cross-section beam can endure more cross-sectional distortion mode and stiffeners influence its buckling mode.

A simple and powerful topology optimization method was introduced [31], which overcome the ill-conditioned problem of the previous homogenization method. In this method, so-called Solid Isotropic Material with Penalization (SIMP), the densities of each element are used as design variables. The stiffness of each element is combined with each variable with its penalization parameter.

By assigning design variables to each cross-sectional sub-beam element, topology optimization of beam cross-section became possible. However, as previously mentioned in the last chapters, since warping plays an essential role in torsional stiffness, cross-sectional topology optimization must consider warping mode. Kim [32] conducted topology optimization of cross-section using bending rigidity and torsional rigidity, which its warping effect was included. However, its objective function was determined by a mixture of torsional rigidity induced by materials and torsional rigidity by the warping effect. The optimization results showed significant differences depending on its mixing ratio. A similar study, mixing rigidity induced by warping and distortion, was conducted [33] but the correct ratio between warping and distortion could not be found.

Liu used Giavotto's beam theory [34] in the cross-sectional topology optimization problem [35,36]. In the theory, local deformation modes and their stiffness with respect to tension, bending, shear, and torsion, are calculated. As a result, it was possible to calculate the topological optimization of the beam cross-section considering not only warping but also an in-plane distortion. Applications to extend on laminated composite beams [37] and on shell-like structures [38] were conducted. However, the beam theory can only handle straight prismatic beams, and the computation cost to calculate all local deformation modes was too large.

The continuum mechanics based beam element has powerful modeling capability using its sub-beam mesh. As previously discussed and proved in the last chapter, enriched with interface warping mode, it can efficiently predict complex coupled behaviors including bending-twisting coupling.

In this chapter, we propose a numerical method that can efficiently calculate the topology optimization of a cross-section of the beam. Sub-beam elements are used as a design cell, and a well-known SIMP method [39] is applied by assigning material density in each sub-beam element. The objective function and its sensitivity will be derived in the next section.

4.2 Objective Function and Its Sensitivity

In an optimization problem, the objective function is defined as the design target, and its derivatives with respect to design variables are defined as sensitivity. In this chapter, compliance, which is the most widely known objective function for structural optimization problems, will be considered as an objective function.

According to SIMP method [39], each design cell has a design variable ρ_e^b, which decides the stiffness tensor

$$\widetilde{\mathbf{C}}_e = \left(\rho_e^b\right)^p \widetilde{\mathbf{C}}_0 , \tag{4-1}$$

where, p is the penalty factor and $\widetilde{\mathbf{C}}_0$ is the base stiffness tensor.

The compliance of beam is

$$C = \mathbf{U}^T \mathbf{K} \mathbf{U} , \tag{4-2}$$

where, $\mathbf{U}$ is the nodal displacement vector, and $\mathbf{K}$ is the stiffness matrix, as we previously mentioned in the last chapter.

Sensitivity is defined as the derivative of the objective function with respect to the design variable. By using chain-rule, sensitivity is

$$\frac{dC}{d\rho_e^b} = -\mathbf{U}^T \frac{d\mathbf{K}}{d\rho_e^b} \mathbf{U} = -\mathbf{U}^T \left(\frac{\partial \mathbf{K}}{\partial \rho_e^b} + \frac{d\mathbf{f}}{d\rho_e^b} \frac{\partial \mathbf{K}}{\partial \mathbf{f}} \right) \mathbf{U} , \tag{4-3}$$

where, $\mathbf{f}$ is the vector containing warping mode.

Eq. (4-1) shows the first part of Eq. (4-3), which is

$$\frac{\partial \mathbf{K}}{\partial \rho_e^b} = \iiint \widetilde{\mathbf{B}}^T \frac{\partial \widetilde{\mathbf{C}}}{\partial \rho_e^b} \widetilde{\mathbf{B}} \|\mathbf{J}\| \, dr\, ds\, dt = \frac{\partial \left(\rho_e^b\right)^p}{\partial \rho_e^b} \iiint \widetilde{\mathbf{B}}^T \widetilde{\mathbf{C}}_0 \widetilde{\mathbf{B}} \|\mathbf{J}\| \, dr\, ds\, dt = p\left(\rho_e^b\right)^{p-1} \mathbf{K}_0 , \tag{4-4}$$

where, $\mathbf{K}_0$ is the base stiffness matrix, which is obtained by assuming the sub-beam has base Young's modulus E_0.

The second part of Eq. (4-3) can be calculated using Eq. (3-32). For simplicity, Eq. (3-32) can be rewritten as

$$\mathbf{W}\mathbf{F} = \mathbf{M} , \tag{4-5}$$

with

$$\mathbf{W} = \begin{bmatrix} \mathbf{K}_w & -\mathbf{N}_z & \mathbf{N}_y & \mathbf{B}_c \\ \mathbf{Q}_x & \mathbf{0} & \mathbf{0} & \mathbf{0} \\ \mathbf{Q}_y & \mathbf{0} & \mathbf{0} & \mathbf{0} \\ \mathbf{Q}_z & \mathbf{0} & \mathbf{0} & \mathbf{0} \\ \mathbf{R}_w & -\mathbf{S}_y & -\mathbf{S}_z & \mathbf{J}_x \end{bmatrix} , \tag{4-6a}$$

$$\mathbf{F} = \begin{bmatrix} \mathbf{U} \\ \tilde{\mathbf{\Lambda}}_y \\ \tilde{\mathbf{\Lambda}}_z \\ \mathbf{A} \end{bmatrix} , \tag{4-6b}$$

$$\mathbf{M} = M_x \begin{bmatrix} \mathbf{0} \\ \mathbf{0} \\ \mathbf{0} \\ \mathbf{0} \\ \mathbf{1} \end{bmatrix}. \tag{4-6c}$$

$\dfrac{d\,\mathbf{f}}{d\rho_e^b}$ can be obtained from $\dfrac{d\,\mathbf{F}}{d\rho_e^b}$ and it can be calculated from derivation of Eq. (4-5),

$$\frac{d\,\mathbf{F}}{d\rho_e^b} = -\mathbf{W}^{-1}\frac{d\mathbf{W}}{d\rho_e^b}\mathbf{F}. \tag{4-7}$$

Differentiating a matrix **K** with a vector **f** results a 3-dimensional tensor, such as

$$\frac{d\mathbf{K}}{d\mathbf{f}} = \left[\frac{d\mathbf{K}}{df_1}\ \frac{d\mathbf{K}}{df_2}\ \cdots\ \frac{d\mathbf{K}}{df_j}\ \cdots\ \frac{d\mathbf{K}}{df_n}\right], \tag{4-8}$$

with

$$\frac{d\mathbf{K}}{df_j} = \iiint \frac{d\widetilde{\mathbf{B}}^T}{df_j}\widetilde{\mathbf{C}}\widetilde{\mathbf{B}}\left\|\mathbf{J}\right\| dr\,ds\,dt + \iiint \widetilde{\mathbf{B}}^T\widetilde{\mathbf{C}}\frac{d\widetilde{\mathbf{B}}}{df_j}\left\|\mathbf{J}\right\| dr\,ds\,dt. \tag{4-9}$$

Strain-displacement interpolation matrix in local coordinate is calculated using coordinate transformation

$$\widetilde{\mathbf{B}}_{nm} = \overline{\mathbf{B}}_{kl}\left(\mathbf{t}_n\cdot\mathbf{g}^k\right)\left(\mathbf{t}_m\cdot\mathbf{g}^l\right), \tag{4-10}$$

with

$$\overline{\mathbf{B}}_{kl} = \frac{1}{2}\left(\frac{d\mathbf{L}}{dr_k}\mathbf{g}_l + \frac{d\mathbf{L}}{dr_l}\mathbf{g}_k\right), \tag{4-11}$$

where, $\overline{\mathbf{B}}_{kl}$ is the strain-displacement interpolation matrix in covariant basis, $\mathbf{t}_n$ is the local basis, $\mathbf{g}^k$ is the contravariant basis, $\mathbf{g}_k$ is the covariant basis, and **L** is the matrix which interpolates nodal displacements to displacement field.

Combining Eq. (4-10) and Eq. (4-11), components of Eq. (4-8) are obtained as

$$\frac{d\widetilde{\mathbf{B}}_{nm}}{df_j} = \frac{1}{2}\left[\frac{d}{df_j}\left(\frac{d\mathbf{L}}{dr_k}\right)\mathbf{g}_l + \frac{d}{df_j}\left(\frac{d\mathbf{L}}{dr_l}\right)\mathbf{g}_k\right]\left(\mathbf{t}_n\cdot\mathbf{g}^k\right)\left(\mathbf{t}_m\cdot\mathbf{g}^l\right). \tag{4-12}$$

Eq. (2-35) shows the linearized displacement field of the continuum mechanics based beam element for nonlinear analysis. In linear analysis, the linearized displacement field can be simplified as

$$\mathbf{u} = h_i\mathbf{u}_i - h_i\left(\frac{\overline{y}_i}{2}\hat{\mathbf{V}}_s^i + \frac{\overline{z}_i}{2}\hat{\mathbf{V}}_t^i\right)\boldsymbol{\theta}_i + h_i\overline{f}_i\mathbf{V}_r^i\Delta\alpha_i. \tag{4-13}$$

Therefore, the **L** matrix in Eq. (4-11) and Eq. (4-12) is

$$\mathbf{L}=h_i\begin{bmatrix} 1 & 0 & 0 & 0 & \left(\frac{\bar{y}_i}{2}V_{sz}^i+\frac{\bar{z}_i}{2}V_{tz}^i\right) & -\left(\frac{\bar{y}_i}{2}V_{sy}^i+\frac{\bar{z}_i}{2}V_{ty}^i\right) & \bar{f}_iV_{rx}^i \\ 0 & 1 & 0 & -\left(\frac{\bar{y}_i}{2}V_{sz}^i+\frac{\bar{z}_i}{2}V_{tz}^i\right) & 0 & \left(\frac{\bar{y}_i}{2}V_{sx}^i+\frac{\bar{z}_i}{2}V_{tx}^i\right) & \bar{f}_iV_{ry}^i \\ 0 & 0 & 1 & \left(\frac{\bar{y}_i}{2}V_{sy}^i+\frac{\bar{z}_i}{2}V_{ty}^i\right) & -\left(\frac{\bar{y}_i}{2}V_{sx}^i+\frac{\bar{z}_i}{2}V_{tx}^i\right) & 0 & \bar{f}_iV_{rz}^i \end{bmatrix}, \tag{4-14}$$

where, $\bar{\mathbf{f}}(s,t)=\mathbf{H}(s,t)\mathbf{f}$ is the interpolated warping function, $\mathbf{f}=[f_1, f_2, \cdots, f_n]$ is the nodal warping function, and $[V_{rx}^i, V_{ry}^i, V_{rz}^i]$, $[V_{sx}^i, V_{sy}^i, V_{sz}^i]$, and $[V_{tx}^i, V_{ty}^i, V_{tz}^i]$ are the components of director vectors $\mathbf{V}_r^i$, $\mathbf{V}_s^i$, and $\mathbf{V}_t^i$, respectively.

The compliance can be expressed in a summation form of elemental compliances

$$C=\mathbf{U}^T\mathbf{K}\mathbf{U}=\sum_{e=1}^{d}\left[\mathbf{U}^{(e)T}\mathbf{K}^{(e)}\mathbf{U}^{(e)}\right], \tag{4-15}$$

where e is the element number.

As previously defined, ρ_e^b is the density of sub-beam b of beam element e, and $\mathbf{f}_{e-1}^e$ is the warping function vector, assigned on a node between element e-1 and e. Since ρ_e^b affects both $\mathbf{f}_{e-1}^e$ and $\mathbf{f}_e^{e+1}$, change of ρ_e^b also affects the stiffness of neighboring beam elements e-1 and e+1.

As a result, the sensitivity can be expressed in a summation form of three elements:

$$\begin{aligned}\frac{dC}{d\rho_e^b}&=-\mathbf{U}^{(e-1)T}\frac{d\mathbf{K}^{(e-1)}}{d\rho_e^b}\mathbf{U}^{(e-1)}-\mathbf{U}^{(e)T}\frac{d\mathbf{K}^{(e)}}{d\rho_e^b}\mathbf{U}^{(e)}-\mathbf{U}^{(e+1)T}\frac{d\mathbf{K}^{(e+1)}}{d\rho_e^b}\mathbf{U}^{(e+1)}\\ &=-\mathbf{U}^{(e-1)T}\frac{\partial\mathbf{K}^{(e-1)}}{\partial\mathbf{f}_{e-1}^e}\frac{d\mathbf{f}_{e-1}^e}{d\rho_e^b}\mathbf{U}^{(e-1)}\\ &\quad-\mathbf{U}^{(e)T}\left(\frac{\partial\mathbf{K}^{(e)}}{\partial\rho_e^b}+\frac{\partial\mathbf{K}^{(e)}}{\partial\mathbf{f}_{e-1}^e}\frac{d\mathbf{f}_{e-1}^e}{d\rho_e^b}+\frac{\partial\mathbf{K}^{(e)}}{\partial\mathbf{f}_e^{e+1}}\frac{d\mathbf{f}_e^{e+1}}{d\rho_e^b}\right)\mathbf{U}^{(e)}\\ &\quad-\mathbf{U}^{(e+1)T}\frac{\partial\mathbf{K}^{(e+1)}}{\partial\mathbf{f}_e^{e+1}}\frac{d\mathbf{f}_e^{e+1}}{d\rho_e^b}\mathbf{U}^{(e+1)}.\end{aligned} \tag{4-16}$$

4.3 Cost Reduction Technique

This section introduces several cost reduction techniques. The techniques rely on mathematical formulations and implementing methods, not approximation; therefore, computation results will be preserved.

The first cost reduction technique is eliminating the chain-rule summation. First, we introduce a new variable $\frac{d\mathbf{f}}{d\rho_e^b} = \mathbf{f}' = [f_1', f_2', \cdots, f_n']$. Then,

$$
\begin{aligned}
\frac{d\mathbf{f}}{d\rho_e^b}\frac{\partial \mathbf{K}}{\partial \mathbf{f}} &= \mathbf{f}'\frac{\partial \mathbf{K}}{\partial \mathbf{f}} = \sum_j f_j' \frac{\partial \mathbf{K}}{\partial f_j} \\
&= \sum_j \left[\iiint \left(f_j' \frac{\partial \widetilde{\mathbf{B}}^T}{\partial f_j} \right) \widetilde{\mathbf{C}}\widetilde{\mathbf{B}} \|\mathbf{J}\| \, dr\, ds\, dt + \iiint \widetilde{\mathbf{B}}^T \widetilde{\mathbf{C}} \left(f_j' \frac{\partial \widetilde{\mathbf{B}}}{\partial f_j} \right) \|\mathbf{J}\| \, dr\, ds\, dt \right] \\
&= \iiint \sum_j \left[\frac{\partial \left(f_j' \widetilde{\mathbf{B}} \right)^T}{\partial f_j} \right] \widetilde{\mathbf{C}}\widetilde{\mathbf{B}} \|\mathbf{J}\| \, dr\, ds\, dt + \iiint \widetilde{\mathbf{B}}^T \widetilde{\mathbf{C}} \sum_j \left[\frac{\partial \left(f_j' \widetilde{\mathbf{B}} \right)}{\partial f_j} \right] \|\mathbf{J}\| \, dr\, ds\, dt \, .
\end{aligned} \tag{4-17}
$$

Since, Eq. (4-12) shows

$$
\frac{\partial \left(f_j' \widetilde{\mathbf{B}}_{nm} \right)}{\partial f_j} = \frac{1}{2} \left[\left(f_j' \frac{\partial}{\partial f_j} \frac{d\mathbf{L}}{dr_k} \right) \mathbf{g}_l + \left(f_j' \frac{\partial}{\partial f_j} \frac{d\mathbf{L}}{dr_l} \right) \mathbf{g}_k \right] \left(\mathbf{t}_n \cdot \mathbf{g}^k \right) \left(\mathbf{t}_m \cdot \mathbf{g}^l \right), \tag{4-18}
$$

by introducing

$$
\mathbf{L}' = h_i \begin{bmatrix} 0 & 0 & 0 & 0 & 0 & 0 & \overline{f}' V_{rx}^i \\ 0 & 0 & 0 & 0 & 0 & 0 & \overline{f}' V_{ry}^i \\ 0 & 0 & 0 & 0 & 0 & 0 & \overline{f}' V_{rz}^i \end{bmatrix}, \tag{4-19}
$$

where, $\overline{f}' = H_j f_j'$ is the interpolated value of nodal values f_j',

Eq. (4-18) can be simplified as follow

$$
\frac{\partial \left(f_j' \widetilde{\mathbf{B}}_{nm} \right)}{\partial f_j} = \frac{1}{2} \left[\frac{d\mathbf{L}'}{dr_k} \mathbf{g}_l + \frac{d\mathbf{L}'}{dr_l} \mathbf{g}_k \right] \left(\mathbf{t}_n \cdot \mathbf{g}^k \right) \left(\mathbf{t}_m \cdot \mathbf{g}^l \right). \tag{4-20}
$$

In a similar manner, a new interpolation matrix $\widetilde{\mathbf{B}}'$ can be defined using $\mathbf{L}'$ as follow:

$$
\widetilde{\mathbf{B}}' = \sum_j \frac{\partial \left(f_j' \widetilde{\mathbf{B}}_{nm} \right)}{\partial f_j} = \frac{1}{2} \left[\frac{d\mathbf{L}'}{dr_k} \mathbf{g}_l + \frac{d\mathbf{L}'}{dr_l} \mathbf{g}_k \right] \left(\mathbf{t}_n \cdot \mathbf{g}^k \right) \left(\mathbf{t}_m \cdot \mathbf{g}^l \right). \tag{4-21}
$$

With the newly introduced variables, the elemental sensitivity can be re-written as

$$
\begin{aligned}
\frac{d\mathbf{K}}{d\rho_e^b} &= \frac{\partial \mathbf{K}}{\partial \rho_e^b} + \frac{d\mathbf{f}}{d\rho_e^b}\frac{\partial \mathbf{K}}{\partial \mathbf{f}} \\
&= \iiint \widetilde{\mathbf{B}}^T \frac{\partial \widetilde{\mathbf{C}}}{\partial \rho_e^b} \widetilde{\mathbf{B}} \|\mathbf{J}\| \, dr\, ds\, dt + \iiint \widetilde{\mathbf{B}}'^T \widetilde{\mathbf{C}}\widetilde{\mathbf{B}} \|\mathbf{J}\| \, dr\, ds\, dt + \iiint \widetilde{\mathbf{B}}^T \widetilde{\mathbf{C}}\widetilde{\mathbf{B}}' \|\mathbf{J}\| \, dr\, ds\, dt \, ,
\end{aligned} \tag{4-22}
$$

which is a more computationally efficient form by avoiding the summation from the chain rule in Eq. (4-17). Note that this procedure does not include approximations.

The second cost reduction technique is about calculating $\frac{d\mathbf{F}}{d\rho_e^b}$ in Eq. (4-7). Eq. (4-6a) shows that $\frac{d\mathbf{W}}{d\rho_e^b}$ is sparse matrix, which indicates that the bottleneck of Eq. (4-7) is the inverse calculation of **W**, not calculating $\frac{d\mathbf{W}}{d\rho_e^b}\mathbf{F}$. Therefore, computational cost can be reduced by calculating the inverse of **W** only once with respect to variables ρ_e^b,

$$\left[\frac{d\mathbf{F}}{d\rho_e^1}, \cdots, \frac{d\mathbf{F}}{d\rho_e^b}\right] = -\mathbf{W}^{-1}\left[\frac{d\mathbf{W}}{d\rho_e^1}\mathbf{F}, \cdots, \frac{d\mathbf{W}}{d\rho_e^b}\mathbf{F}\right]. \tag{4-23}$$

The last cost reduction technique is about calculating $\mathbf{W}^{-1}$ in Eq. (4-5) using Cholesky decomposition. Since, **W** from Eq. (4-6a) is not square matrix, QR-decomposition is required to solve inverse problem of **W**. Due to orthogonality condition Eq. (3-13b), $\mathbf{K_w}$ in Eq. (4-6a) have 3 null vectors, which can be easily eliminated by assigning 0 values to an arbitrary nodal warping value on each cross-section. Eq. (4-6a)-(4-6c) can be re-written as

$$\mathbf{W}' = \begin{bmatrix} \mathbf{K}_w^{redu} & -\mathbf{N}_z^{redu} & \mathbf{N}_y^{redu} & \mathbf{B}_c^{redu} \\ \mathbf{Q}_y^{redu} & \mathbf{0} & \mathbf{0} & \mathbf{0} \\ \mathbf{Q}_z^{redu} & \mathbf{0} & \mathbf{0} & \mathbf{0} \\ \mathbf{R}_w^{redu} & -\mathbf{S}_y & -\mathbf{S}_z & \mathbf{J}_x \end{bmatrix}, \tag{4-24a}$$

$$\mathbf{F}' = \begin{bmatrix} \mathbf{U}^{redu} \\ \tilde{\mathbf{\Lambda}}_y \\ \tilde{\mathbf{\Lambda}}_z \\ \mathbf{A} \end{bmatrix}, \tag{4-24b}$$

$$\mathbf{M}' = M_x \begin{bmatrix} \mathbf{0} \\ \mathbf{0} \\ \mathbf{0} \\ \mathbf{0} \\ \mathbf{1} \end{bmatrix}. \tag{4-24c}$$

where, the size of matrices and vectors with superscript 'redu' has decreased due to boundary condition, $\mathbf{Q}_x$. Eq. (4-24a)-(4-24c) can be simplified as,

$$\mathbf{W}' = \begin{bmatrix} \mathbf{K} & \mathbf{N} \\ \mathbf{Q} & \mathbf{0} \\ \mathbf{R} & \mathbf{S} \end{bmatrix}, \tag{4-25a}$$

$$\mathbf{F}' = \begin{bmatrix} \mathbf{P} \\ \mathbf{\Lambda} \end{bmatrix}, \tag{4-25b}$$

$$\mathbf{M}' = \begin{bmatrix} \mathbf{0} \\ \mathbf{0} \\ \mathbf{T} \end{bmatrix}. \tag{4-25c}$$

Note that **K** is sparse semi-positive definite symmetric invertible matrix. With some linear algebra, Eq. (4-25a)-(4-25c) are simplified as

$$\Lambda = \begin{bmatrix} \mathbf{Q}\mathbf{K}^{-1}\mathbf{N} \\ \mathbf{S} - \mathbf{R}\mathbf{K}^{-1}\mathbf{N} \end{bmatrix}^{-1} \begin{bmatrix} \mathbf{0} \\ \mathbf{T} \end{bmatrix}, \tag{4-26a}$$

$$\mathbf{P} = -\mathbf{K}^{-1}\mathbf{N}\Lambda , \tag{4-26b}$$

where, the matrix of Eq. (4-25a) has size of 9×9, therefore calculating $\mathbf{K}^{-1}\mathbf{N}$ is the bottleneck of calculating interface warping function. It is notable that due to symmetricity and semi-positive definite property of **K**, the Cholesky-decomposition can be used to calculate inverse problem of **K**, which is far more computational efficient compared to QR-decomposition. The warping function **F** can be obtained by applying Eq. (3-13b) to **P**.

4.4 Numerical Results

In this section, we proposed three numerical examples of beam cross-sectional topology optimization problems. Two examples are obtaining the optimal shape of straight prismatic beams with different design spaces - square and L-section. The last example is an optimization problem about the curved beam. The final converged cross-sections and the objective function with respect to time history are displayed together. As previously discussed, compliance is the objective function and its constraints are given as an upper bound of material. OC and MMA are used as an optimizer, depending on problems.

Two reference models are used for comparison, as shown in Table 4-1. One is the solid element model written in MATLAB, which is revised from Ref. [40]. The code from Ref. [40] is fully ‘vectorized’, therefore it is known to have the fastest speed among the codes for calculating topology optimization using solid element without further assumptions or techniques. Only the mesh part was modified in Ref. [40] to model the curved beams. The other reference model is obtained using commercial software ANSYS. ANSYS topology optimization module is known to be written in Fortran and C/C++, and multicore processors are available. However, the proposed beam is written in MATLAB with partially ‘vectorized’ expressions. For comparison, the same methodology, SIMP with penalization parameter p=3 and convergence tolerance 0.001 are used for all models. OC and MMA are used to solve the proposed beam and reference solid model. However commercial software ANSYS only offers OC.

Table 4-1. Comparison of proposed beam model, reference solid model, and ANSYS.

	Proposed beam	Reference solid	ANSYS
	In-house code (MATLAB)	Revised code [41] (MATLAB)	Commercial software (Fortran, C/C++)
Parallel	Partially vectorized	Fully vectorized	Parallel code
Methodology	SIMP	SIMP	SIMP
Optimizer	OC/MMA	OC/MMA	OC
Tolerance	0.001	0.001	0.001

The inverse matrix problem is known to be the computational bottleneck of topology optimization, and Table 4-2 shows the matrix size of each model. The number of DOFs for both reference solid model and ANSYS are $3abc$, and it became the size of matrix to solve. The calculation of interface warping functions, and its derivatives with respect to design variables, as shown in Eq. (4-23), is the bottleneck for the topology optimization using the proposed beam model. The matrix size to solve interface warping for the proposed beam model is $3ab$, which is the number of nodal warping DOFs in 3 cross-sections. Since, there are c number of cross-sections, the inverse problem of size $3ab$ should be performed c times, which is still cost efficient compared to the inverse problem of matrix size $3abc$. The size of matrix to solve beam element is $7c$, since there are 7DOF per each beam node.

Using cost reduction techniques mentioned in section 4.3, Cholesky decomposition can not only be applied to the reference solid model and ANSYS, but also to the proposed beam model. For simplicity, it is assumed that no re-ordering process are applied to sparse banded symmetric matrices. The time complexity of Cholesky decomposition of matrix size n and half-bandwidth b is $O(bn^2)$ and its backward and forward substitution takes $O(2bn)$ for a single vector, as a result total time complexity big-O of inverse matrix problem for a single vector is $O(bn^2+2bn)$. The FLOPs (FLoating time OPeartionS) and time complexity of the reference solid model and ANSYS are roughly calculated in Table 4-2. However, Eq. (4-23) shows that while calculating the sensitivity of the proposed beam model, backward and forward substitution should be performed not only once, but for the number of nodes in adjacent cross-sections. As a result, the bottleneck of the proposed beam model is the Eq. (4-23), due to forward and backward substitution which takes $O(2bn^2)$. However, for beam-like structures, since the number of mesh c required for longitudinal direction is far bigger than the cross-sectional mesh a and b, the total time complexity of the proposed beam model is less than the reference solid model.

Table 4-2. Time complexity comparison of proposed beam model, reference solid model, and ANSYS.

	Proposed beam	Reference solid	ANSYS
Mesh	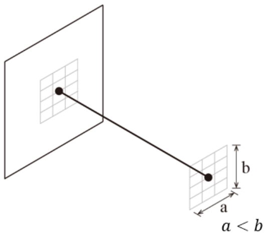	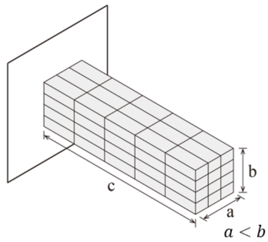	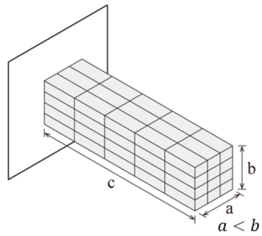
Matrix size to solve	$[3ab]$	$[3abc]$	$[3abc]$
Sparsity	Sparse banded	Sparse banded	Sparse banded
Inverse sol.	Cholesky decomposition	Cholesky decomposition	Cholesky decomposition
FLOPs	$3a^3b+18a^3b^2$	$27a^3bc+18a^2bc$	$27a^3bc+18a^2bc$
Big-O	$O(a^3b^2)$	$O(a^3bc)$	$O(a^3bc)$

4.4.1 Square-Section Beam Problem

A simple design optimization problem is considered in order to verify the validity of the proposed optimization method. **Fig. 4-1(a)** shows the straight square-section prismatic beam with Young's modulus $E = 1\,\text{Pa}$ and Poisson's ratio $\nu = 0.3$. The cross-section of continuum mechanics based beam is discretized using uniform mesh of 40×40 4-node elements, as shown in **Fig. 4-1(b)**. The beam is fully clamped at one side of the end, $x = 0\,\text{m}$, and a torsional moment M_x is applied at the other end of the beam, $x = 10\,\text{m}$. Due to the simplicity of boundary conditions, the model is built using one 2-node beam element. OC is used as an optimizer with Maxjump=0.2.

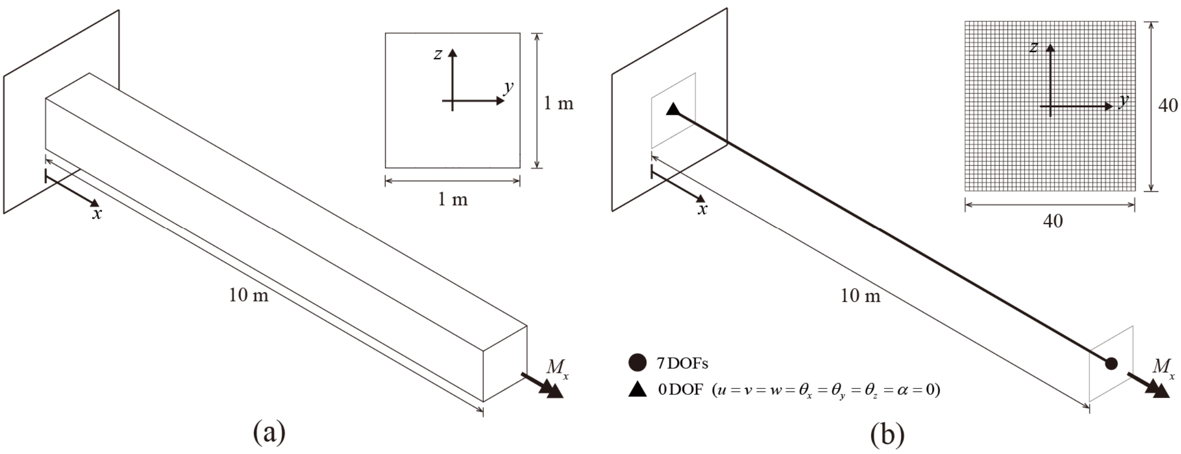

Figure 4-1. Square-section beam problem. (a) Physical model. (b) Beam model and its cross-sectional mesh.

Fig. 4-2 shows the distribution of design variables ρ_e, which are the relative material density used in SIMP method. The results using material constraints of 30%, 50%, and 60% are displayed. The results show the mixed shape between circular hollow beam and square boxed hollow beam. Since the square box is the optimum shape with maximum torsional rigidity and the circular beam is the optimum shape to eliminate the warping mode, it can be explained that the optimum shape is in between those two shapes. The proposed beam model result showed close shape to solid reference model result, compared to the result by Kim and Kim [32]. The results of ANSYS shows smoothed contours due to its automatic post-processing.

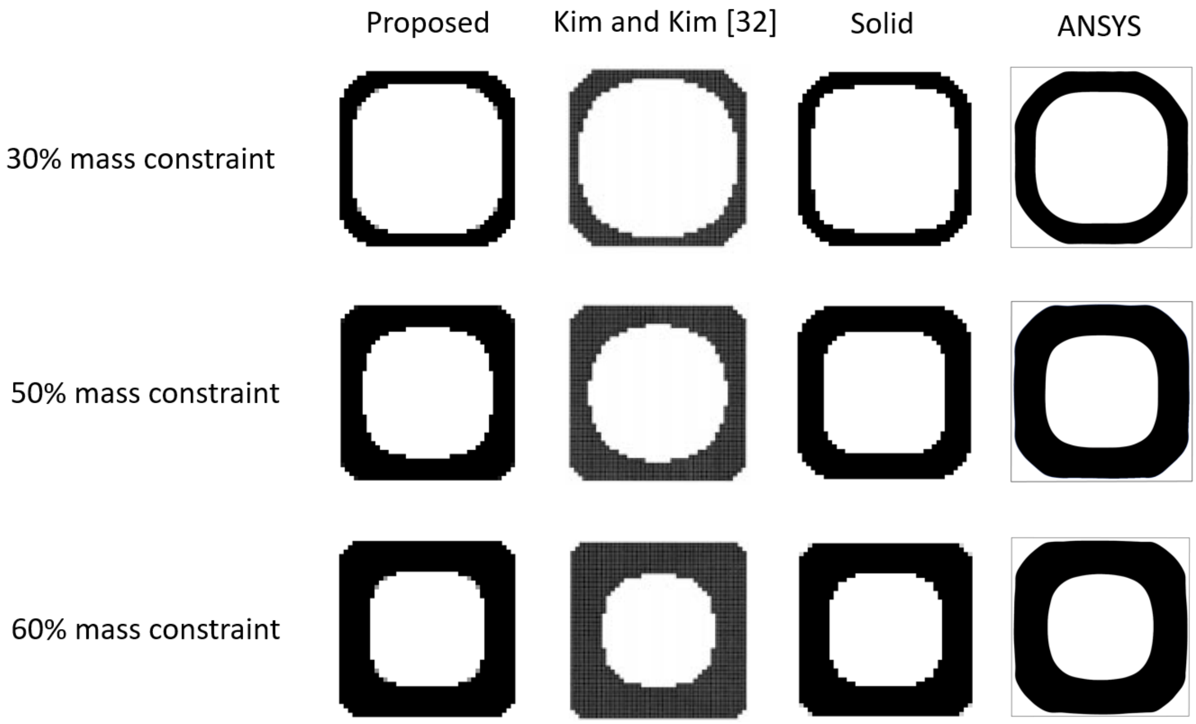

Figure 4-2. Optimized cross-sections of square-section beam problem with different mass constraints.

The objective functions with respect to iteration steps are displayed in **Fig. 4-3** and all the convergence history showed good convergence curve with less than 25 iteration steps. Note that, the more mass constraint we use, less compliance we get.

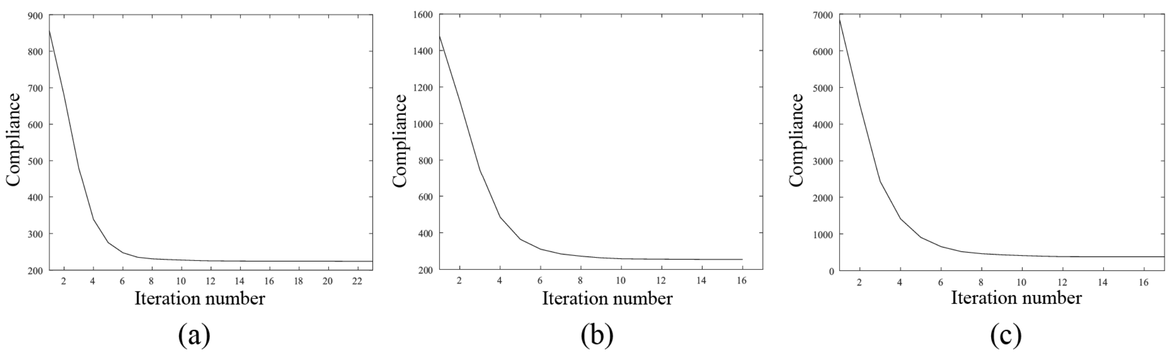

Figure 4-3. Convergence history of square-section beam problem: (a) 60% mass constraint, (b) 50% mass constraint, and (c) 30% mass constraint.

Table 4-3. shows the optimization results. Both the proposed beam model and the reference solid model showed similar compliance values, while the compliance value was unable to be obtained from ANSYS. The computational time of topology optimization are displayed and compared. Both the average time per iteration and the number of iterations are shown as well as overhead time.

Table 4-3. Optimization results of square-section beam problem.

	Proposed beam	Reference solid	ANSYS
Compliance	254.5439	255.9978	-
# of design variables	40×40×1	40×40×15	40×40×25
DOF of inverse problem	5,052	45,387	126,075
Overhead [s]	3.5	593	59
Avg. time per iteration [s/iter]	5.5	76.3	40.6
# of iteration	12	31	18
Total time [s]	69.5	2958.2	789.9

4.4.2 L-Section Beam Problem

Straight prismatic beam with L-section as shown in **Fig. 4-4(a)** is considered. For simplicity, one 2-node continuum mechanics based beam element is used to build beam mode, and its cross-section is discretized using 1728 4-node elements, as illustrated in **Fig. 4-4(b)**. The beam has exact same boundary conditions, which are fully clamped condition at one side of the end, $x = 0\,\text{m}$, and a torsional moment M_x applied at the other end of the beam, $x = 10\,\text{m}$. Beam has Young's modulus $E = 1\,\text{Pa}$ and Poisson's ratio $\nu = 0.3$.

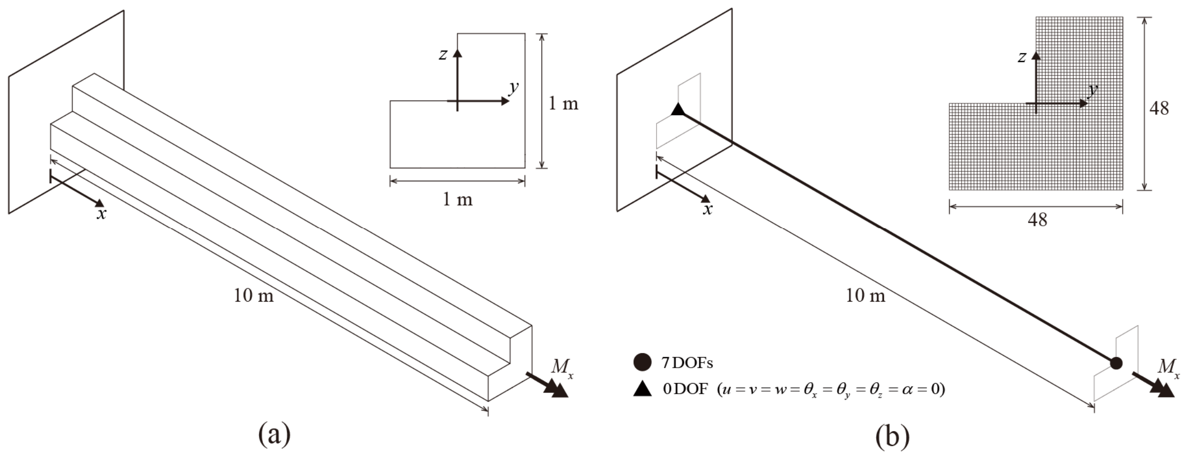

Figure 4-4. L-section beam problem. (a) Physical model. (b) Beam model and its cross-sectional mesh.

Two optimizers are used in this example, OC and MMA, with parameter Maxjump=0.2. The final converged shape with respect to relative material density ρ_e, when MMA is used, are plotted in **Fig. 4-5**. The results showed closed section beams, which are known to have good torsional rigidity. The mixed form of circular beam and box shaped cross-sections can be found in the results. Since the continuum mechanics based beam with warping mode enrichment calculates the shear stress in the cross-section, the result shows optimized shape avoiding shear stress concentration.

Fig. 4-6 shows the convergence history of objective functions with respect to iteration steps, when MMA is used as an optimizer, which shows stable convergence behavior within 30 iteration steps. The converged values also showed less compliance when more mass constraint is used.

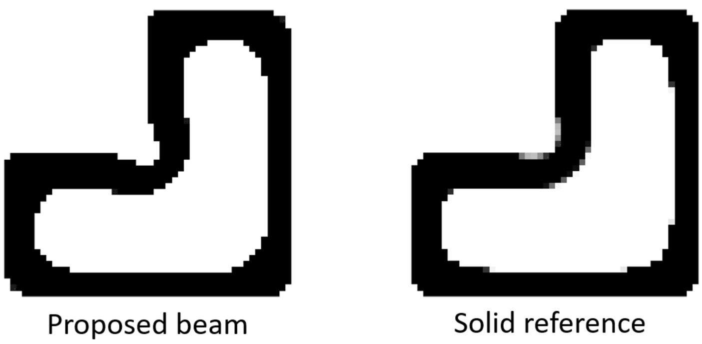

Figure 4-5. Optimized cross-sections of L-section beam problem using MMA.

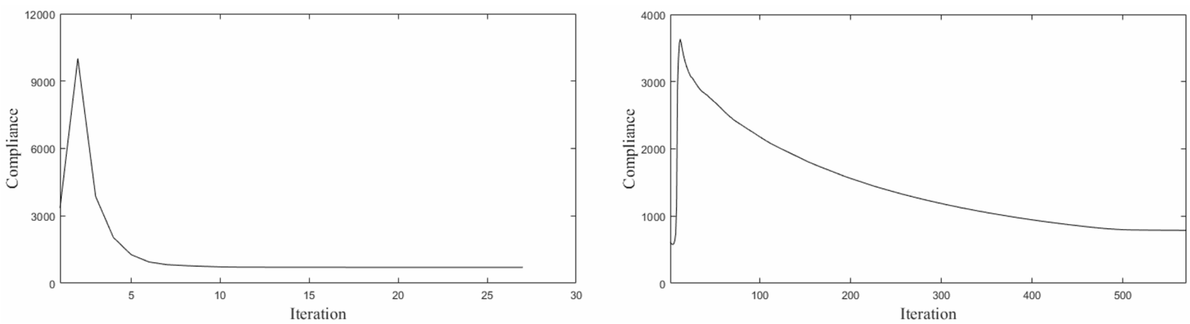

Figure 4-6. Convergence history of L-section beam problem using MMA: (a) proposed beam model, and (b) solid reference model.

Fig. 4-7 shows the final converged shape when OC is used as an optimizer. Since ANSYS provides OC as an optimizer, its result is used for comparison. The final converged shapes show more sharp edges, compared to the results obtained using MMA, see **Fig. 4-5**. The convergence history shown in **Fig. 4-8** also showed good convergence behavior with less iteration numbers.

Since the final compliance obtained using OC is less than the compliance obtained using MMA, it can be concluded that the result of MMA is the local minimum. Therefore, we compare the results using OC, as shown in Table. 4-4. The proposed beam model showed similar compliance value compared with the result obtained using solid reference model, and showed less computation time.

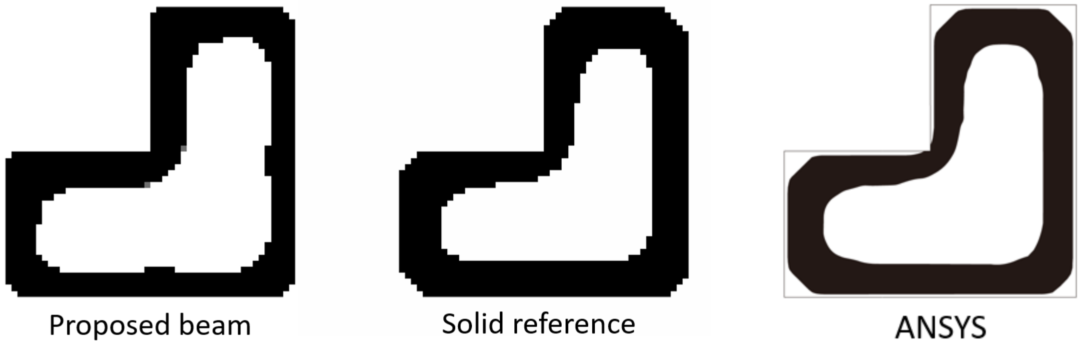

Figure 4-7. Optimized cross-sections of L-section beam problem using OC.

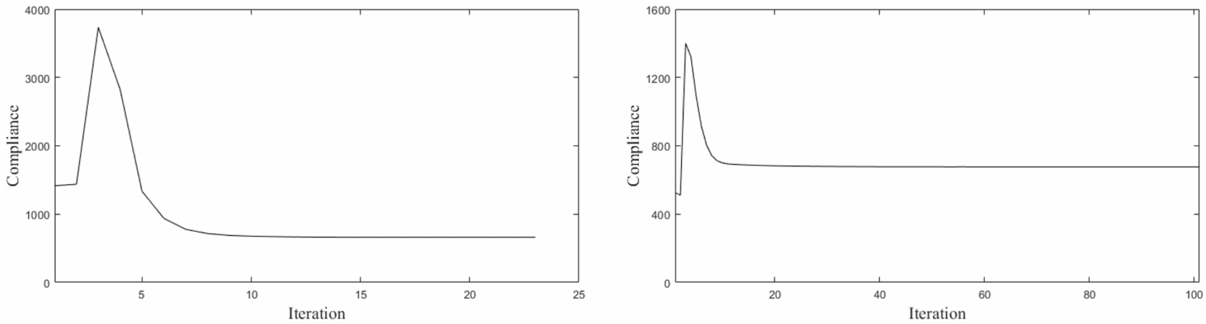

Figure 4-8. Convergence history of L-section beam problem using OC: (a) proposed beam model, and (b) solid reference model.

Table 4-4. Optimization results of L-section beam problem.

	Proposed beam	Reference solid	ANSYS
Compliance	660.4315	676.6892	-
# of design variables	48×48×1	48×48×9	48×48×26
DOF of inverse problem	5,484	38,325	147,825
Overhead [s]	5.9	1469	51.6
Avg. time per iteration [s/iter]	34.7	234.9	106.7
# of iteration	23	101	17
Total time [s]	804.0	25,193.9	1,865.5

4.4.3 90-degree Curved Beam Problem

As a last example, a 90-degree curved beam is considered, as illustrated in **Fig. 4-9(a)**. The beam has square cross-section with Young's modulus $E = 1\text{Pa}$ and Poisson's ratio $\nu = 0.3$. The cross-section of continuum mechanics based beam is discretized using uniform mesh of 30×30 4-node elements, as shown in **Fig. 4-9(b)**. Element numbers, starting from its boundary condition, are marked in Greek numbers. The beam is fully clamped at $\phi = 0°$, and a torsional moment M_y is applied at $\phi = 90°$. In order to observe the cross-sections of each beam elements, eight 2-node beam element are used to build beam model. Total volume is constrained as 50%. OC is used as an optimizer with parameter Maxjump=0.2.

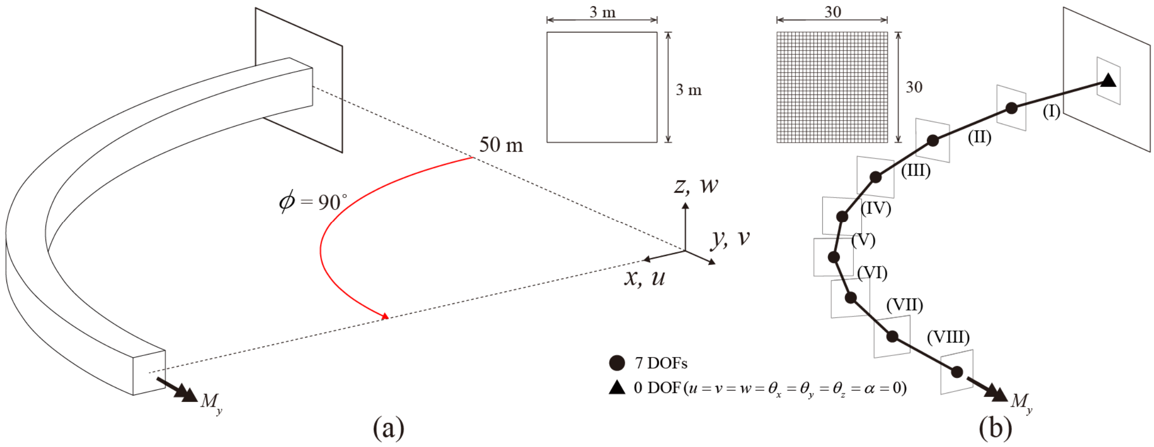

Figure 4-9. 90-degree curved beam problem. (a) Physical model. (b) Beam model and its cross-sectional mesh. Element numbers are assigned in Greek numbers.

The final converged shapes of each cross-sections are plotted in **Fig. 4-10**, and their cross-section numbers are marked in Greek letters. Since the beam is curved, each beam element should endure different external force. Therefore, as shown in **Fig. 4-10**, the optimized cross-section shapes are different each other. Cross-sections close to the external force M_y tends to show a circular box-shaped cross-section, which we have observed in section 4.4.1. However, the cross-sections close to the boundary loss its circular shapes, and mimics the H-shaped cross-section, which is widely known to have maximum bending rigidity. The convergence history plotted in **Fig. 4-11** shows good convergence behavior. It is noteworthy, that the volume in each element sections are almost equal to each other, although the mass constraints are applied as sum of all element's volume.

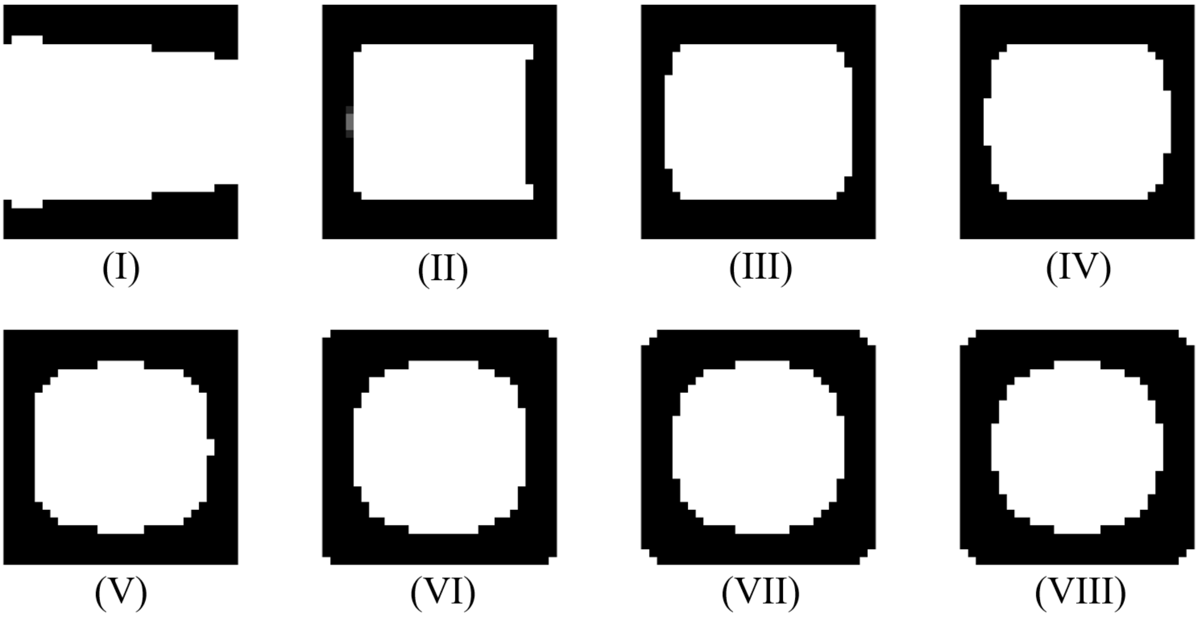

Figure 4-10. Optimized cross-sections of 90-degree curved beam problem with 30×30 mesh.

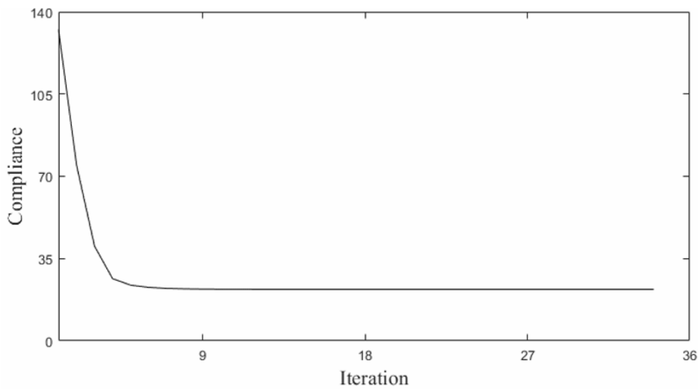

Figure 4-11. Convergence history of 90-degree curved beam problem with 30×30 mesh.

Same topology optimization is performed with more fine mesh, 60×60. **Fig. 4-12** shows the converged cross-sectional shapes. Its convergence history is displayed in **Fig. 4-13**.

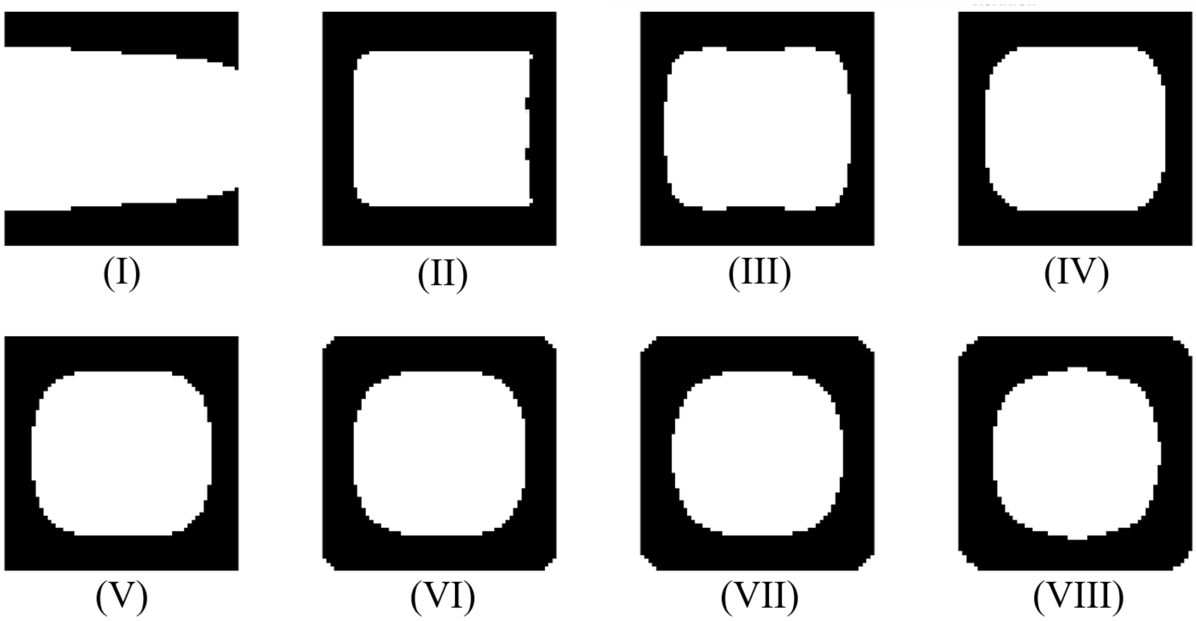

Figure 4-12. Optimized cross-sections of 90-degree curved beam problem with 60×60 mesh.

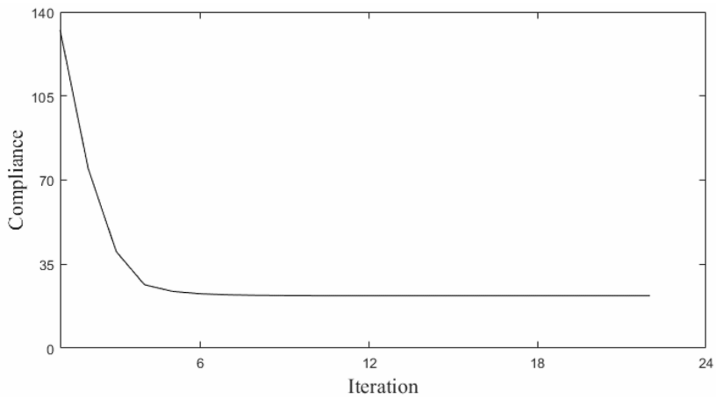

Figure 4-13. Convergence history of 90-degree curved beam problem with 60×60 mesh.

The results are displayed and compared in **Fig. 4-14** which shows good agreement with each other. It can be concluded that the proposed beam model can reflect and predict its optimized cross-section when the beam is not straight. The powerful modeling capability from the continuum mechanics based beam element is inherited to the model, therefore the proposed model could reflect the bending-twisting coupling behavior. Table 4-5 compares the converged compliance values and the computation time costs, which shows benefit of using the proposed beam model.

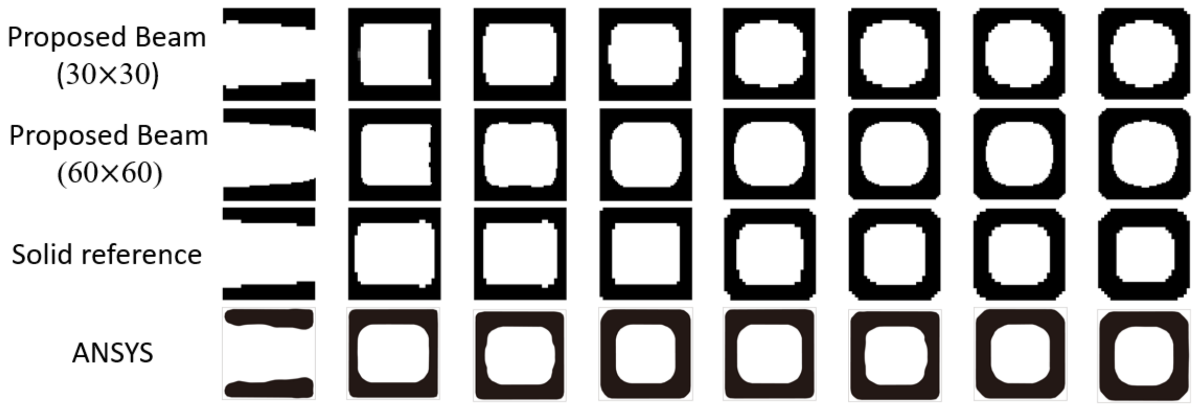

Figure 4-14. Cross-sectional geometries of 90-degree curved beam problem using (a) proposed beam model of mesh size 30×30, (b) proposed beam model of mesh size 60×60, (c) solid reference model, and (d) ANSYS

.

Table 4-5. Optimization results of 90-degree curved beam problem.

	Proposed beam	Reference solid	ANSYS
Compliance	21.8909	18.1737	-
# of design variables	30×30×8	30×30×24	30×30×112
DOF of inverse problem	2,895	72,075	325,779
Overhead [s]	14	1556	116
Avg. time per iteration [s/iter]	27.3	92.7	100.1
# of iteration	34	940	14
Total time [s]	942.2	88,756	1,518

4.5 Concluding Remarks

A new method of finding the optimal beam cross-section for a given boundary and force condition with fully coupled motion, including bending, is proposed. The sensitivity is derived directly from the continuum mechanics based beam formulation enriched with warping mode without further assumption. Numerical techniques without approximation are suggested in order to reduce computational cost. A well-known SIMP method is implemented, which is relatively simple and straight-forward, and the numerical examples showed good convergence history of objective function. The final converged shape of cross-sections are mixture of circular cross-sections, which are known to have zero warping, and box-shaped cross-sections, which are known to have maximum torsional rigidity. Its scalability is shown through L-shaped design space topology optimization. Through 90-degree curved beam example, it also showed that the proposed method can be used to calculate the optimum design, which endures complex force induced by its complex geometry.

Chapter 5. Conclusions

5.1 Conclusions

In this dissertation, applications of continuum mechanics based beam with warping enrichment is newly proposed, which are the interface warping enrichment and cross-sectional topology optimization.

In chapter 2, continuum mechanics based beam is introduced with the nonlinear formulation. The method of enriching warping mode into continuum mechanics based beam is introduced which does not violate the compatibility condition of the displacement field.

In chapter 3, the method of calculating interface warping and its efficient direct calculation method are proposed. The interface warping is implemented in the continuum mechanics based beam with an additional degree-of-freedom. Numerical examples showed that the newly proposed interface warping can successfully predict the behavior of beams with longitudinal discontinuities. The geometric non-linear analysis also showed good agreement with the results predicted by solid elements.

In chapter 4, cross-sectional topology optimization of the beam is proposed. Sub-beams are designated as design cells, and design parameters are assigned for each sub-beams using the SIMP method. By using continuum mechanics based beam with interface warping enrichment, cross-sectional topology optimization with respect to various force conditions is achieved.

Appendix

Appendix A. Effect of Warping on Torsional Rigidity

Here, we briefly show that the warping of beam always reduces the torsional rigidity. Torsional rigidity of beam J is defined as the division of torsional moment M over twist rate α. From Eq. (3-12),

$$J = \frac{dM}{d\alpha} = \int_A G\left(y\frac{\partial f}{\partial z} - z\frac{\partial f}{\partial y} \right) dA - \lambda_y \int_A GydA - \lambda_z \int_A GzdA + \int_A G\left(y^2 + z^2\right) dA . \tag{A-1}$$

Eqs. (3-10a)-(3-10b) shows,

$$F_y = \int_A \sigma_{yx} dA = \int_A G\left(\frac{\partial u}{\partial y} + \frac{\partial v}{\partial x} \right) dA = \alpha \int G\frac{\partial f}{\partial y} dA = 0 , \tag{A-2a}$$

$$F_z = \int_A \sigma_{zx} dA = \int_A G\left(\frac{\partial u}{\partial z} + \frac{\partial w}{\partial x} \right) dA = \alpha \int G\frac{\partial f}{\partial z} dA = 0 , \tag{A-2b}$$

and definition of twist center of prismatic beam gives,

$$\int_A GydA = \lambda_y \int_A GdA , \tag{A-2c}$$

$$\int_A GzdA = \lambda_z \int_A GdA . \tag{A-2d}$$

Substituting Eqs. (A-2a)-(A-2d) into Eq. (A-1), the torsional rigidity is rearranged as follow

$$J = \int_A G\left(\bar{y}^2 + \bar{z}^2\right) dA - \int_A G\left(\bar{z}\frac{\partial f}{\partial y} - \bar{y}\frac{\partial f}{\partial z} \right) dA , \tag{A-3}$$

where $\bar{y} = y - \lambda_y(x)$ and $\bar{z} = z - \lambda_z(x)$, as previously defined in Eq. (3-1). Using divergence theorem, the integral in Eq. (A-3) can be substituted into contour integration of cross-section A,

$$\int_A G\left[\frac{\partial(\bar{z}f)}{\partial y} + \frac{\partial(-\bar{y}f)}{\partial z} \right] dA = \oint_{\partial A} G\left[(\bar{y}f) n_z + (-\bar{z}f) n_y \right] dl . \tag{A-4a}$$

Substituting Eq. (2-10b),

$$\oint_{\partial A} f\left[G\bar{y}n_z - G\bar{z}n_y \right] dl = \oint_{\partial A} f\left[\frac{\partial(Gf)}{\partial y} n_y + \frac{\partial(Gf)}{\partial z} n_z \right] dl , \tag{A-4b}$$

and by divergence theorem,

$$\oint_{\partial A} \left[f\frac{\partial(Gf)}{\partial y} n_y + f\frac{\partial(Gf)}{\partial z} n_z \right] dl = \int_A \left[\frac{\partial}{\partial y}\left(f\frac{\partial(Gf)}{\partial y} \right) + \frac{\partial}{\partial z}\left(f\frac{\partial(Gf)}{\partial z} \right) \right] dA . \tag{A-4c}$$

Eq. (A-4c) can be simplified using Eq. (2-10a),

$$\int_A G\left[\frac{\partial}{\partial y}\left(f\frac{\partial(Gf)}{\partial y} \right) + \frac{\partial}{\partial z}\left(f\frac{\partial(Gf)}{\partial z} \right) \right] dA = \int_A \left[\frac{\partial f}{\partial y}\frac{\partial(Gf)}{\partial y} + \frac{\partial f}{\partial z}\frac{\partial(Gf)}{\partial z} \right] dA . \tag{A-4d}$$

If we assume material properties are constant within the sub-beam element domain, through Eq. (A-4a)-(A-4d), Eq. (A-3) can be rewritten as,

$$J = \int_A G\left(\overline{y}^2 + \overline{z}^2\right) dA - \int_A G\left[\left(\frac{\partial f}{\partial y}\right)^2 + \left(\frac{\partial f}{\partial z}\right)^2\right] dA \,. \tag{A-5}$$

Note that the integrand of the second term in Eq. (A-5) is always positive, therefore the warping of beams always reduces the torsional rigidity:

$$J < \int_A G\left(\overline{y}^2 + \overline{z}^2\right) dA = \sum_k G_k \overline{I}_k \,, \tag{A-6}$$

where $\overline{I}_k$ is the second moment of area normal to the cross-section of cross-sectional domain *k* with respect to twisting center (λ_y, λ_z) and G_k is the bulk modulus of cross-sectional domain *k*.

Bibliography

[1] Goss VG. Snap buckling, writhing and loop formation in twisted rods. University of London, 2003.

[2] Park YB, Yang DY. Analysis of torsional deformation by rigid-plastic finite element method using recurrent boundary conditions. J Mater Process Technol 2007;182:303–11.

[3] de Saint-Venant A. J. C. B. Mémoire sur la torsion des prismes. 1855.

[4] Vlasov VZ. Thin-walled Elastic Beams. Jerusalem: Israel Program for Scientific Translations; 1961.

[5] Dvorkin EN, Celentano D, Cuitiño A, Gioia G. A Vlasov beam element. Comput Struct 1989;33:187–96.

[6] Reddy JN, Wang CM, Lee KH. Relationships between bending solutions of classical and shear deformation beam theories. Int J Solids Struct 1997;34:3373–84.

[7] Reddy JN, Wang CM, Lim GT, Ng KH. Bending solutions of Levinson beams and plates in terms of the classical theories. Int J Solids Struct 2001;38:4701–20.

[8] Eisenberger M. An exact high order beam element. Comput Struct 2003;81:147–52.

[9] Dufort L, Drapier S, Grédiac M. Closed-form solution for the cross-section warping in short beams under three-point bending. Compos Struct 2001;52:233–46.

[10] Benscoter S. U., A theory of torsion bending for multicell beams. J. appl. Mech. 21, 25-34, 1954.

[11] Shakourzadeh H, Guo YQ, Batoz JL. A torsion bending element for thin-walled beams with open and closed cross sections. Comput Struct 1995;55:1045–54.

[12] El Fatmi R. Non-uniform warping including the effects of torsion and shear forces. Part I: A general beam theory. Int J Solids Struct 2007;44:5912–29.

[13] El Fatmi R. Non-uniform warping including the effects of torsion and shear forces. Part II: Analytical and numerical applications. Int J Solids Struct 2007;44:5930–52.

[14] El Fatmi R, Ghazouani N. Higher order composite beam theory built on Saint-Venant's solution. Part-I: Theoretical developments. Compos Struct 2011;93:557–66.

[15] Yoon K, Lee PS, Kim DN. Geometrically nonlinear finite element analysis of functionally graded 3D beams considering warping effects. Compos Struct 2015;132:1231–47.

[16] Sapountzakis EJ, Mokos VG. Warping shear stresses in nonuniform torsion of composite bars by BEM. Comput Methods Appl Mech Eng 2003;192:4337–53.

[17] Sapountzakis EJ, Mokos VG. Nonuniform torsion of composite bars of variable thickness by BEM. Int J Solids Struct 2004;41:1753–71.

[18] Iesan D. Classical and generalized models of elastic rods. New York: Chapman and Hall/CRC; 2008.

[19] Genoese A, Genoese A, Bilotta A, Garcea G. A mixed beam model with non-uniform warpings derived from the Saint Venànt rod. Comput Struct 2013;121:87–98.

[20] Genoese A, Genoese A, Bilotta A, Garcea G. A geometrically exact beam model with non-uniform warping coherently derived from the Saint Venant rod. Eng Struct 2014;68:33–46.

[21] Yoon K, Lee Y, Lee PS. A continuum mechanics based 3-D beam finite element with warping

displacements and its modeling capabilities. Struct Eng Mech 2012;43:411–37.

[22] Yoon K, Lee PS. Nonlinear performance of continuum mechanics based beam elements focusing on large twisting behaviors. Comput Methods Appl Mech Eng 2014;281:106–30.

[23] Yoon K, Lee PS, Kim DN. An efficient warping model for elastoplastic torsional analysis of composite beams. Compos Struct 2017;178:37–49.

[24] Yoon K, Kim DN, Lee PS. Nonlinear torsional analysis of 3D composite beams using the extended St. Venant solution. Struct Eng Mech 2017;62:33–42.

[25] Yoon K, Lee PS. Modeling the warping displacements for discontinuously varying arbitrary cross-section beams. Comput Struct 2014;131:56–69.

[26] Park SW, Fujii D, Fujitani Y. A finite element analysis of discontinuous thin-walled beams considering nonuniform shear warping deformation. Comput Struct 1997;65:17–27.

[27] Gunnlaugsson GA, Pedersen PT. A finite element formulation for beams with thin walled cross-sections. Comput Struct 1982;15:691–9.

[28] Bathe KJ. Finite Element Procedures. New York: Prentice Hall; 1996.

[29] Hughes TJR. The Finite Element Method: Linear Static and Dynamic Finite Element Analysis. Dover Publications; 2000.

[30] ANSYS. ANSYS Mechanical APDL Theory Reference. ANSYS Inc.; Release 19.

[31] Bendsøe MP, Sigmund O. Material interpolation schemes in topology optimization. Arch Appl Mech 1999;69:635–54.

[32] Kim YY, Kim TS. Topology optimization of beam cross sections. Int J Solids Struct 2000;37:477–93.

[33] Kim TS, Kim YY. Multiobjective topology optimization of a beam under torsion and distortion. AIAA J 2002;40:376–81.

[34] Giavotto V, Borri M, Mantegazza P, Ghiringhelli G, Carmaschi V, Maffioli GC, et al. Anisotropic beam theory and applications. Comput Struct 1983;16:403–13.

[35] Liu S, An X, Jia H. Topology optimization of beam cross-section considering warping deformation. Struct Multidiscip Optim 2008;35:403–11.

[36] Liu J, Li Q, Liu S, Tong L. Concurrent optimization design of axial shape and cross-sectional topology for beam structures. Struct Multidiscip Optim 2019;59:2287–302.

[37] Blasques JP, Stolpe M. Multi-material topology optimization of laminated composite beam cross sections. Compos Struct 2012;94:3278–89.

[38] Li Q, Qu Y, Luo Y, Liu S. Concurrent topology optimization design of stiffener layout and cross-section for thin-walled structures. Acta Mech Sin Xuebao 2021;37:472–81.

[39] Bendsoe, Martin Philip, Sigmund O. Topology Optimization: Theory, Methods, and Applications. vol. 540. 2012.

[40] Liu K, Tovar A. An efficient 3D topology optimization code written in Matlab. Struct Multidiscip Optim 2014; 50:1175-1196.